# Université de Montréal

# FROM ELECTRON RECONSTRUCTION AND IDENTIFICATION TO THE SEARCH FOR SUPERSYMMETRY AT THE ATLAS EXPERIMENT

par

## Tuan Nguyen

Département de physique
Faculté des arts et des sciences

Thèse présentée en vue de l'obtention du grade de
Philosophiæ Doctor (Ph.D.)
en Physique

May 20, 2020

# Université de Montréal

Faculté des arts et des sciences

Cette thèse intitulée

## FROM ELECTRON RECONSTRUCTION AND IDENTIFICATION TO THE SEARCH FOR SUPERSYMMETRY AT THE ATLAS EXPERIMENT

présentée par

## Tuan Nguyen

a été évaluée par un jury composé des personnes suivantes :

*Manu Paranjape*

(président-rapporteur)

*Jean-François Arguin*

(directeur de recherche)

*Georges Azuelos*

(membre du jury)

*Hugo Beauchemin*

(examinateur externe)

*Véronique Hussin*

(représentant du doyen de la FESP)

# Résumé

La supersymétrie est une des théories privilégiées pour expliquer la physique au-delà du Modèle Standard. Le LHC, qui fonctionne à des énergies de centre de masse les plus élevées jusqu'à ce jour, procure une opportunité inégalée de vérifier si cette théorie existe.

Le traitement des électrons de signal occupe une place importante dans la recherche de supersymétrie qui inclut des leptons (électrons et muons) dans les états finaux du détecteur ATLAS. En raison des nombreuses sources de di-leptons de charge opposée dans le Modèle Standard et de leur contribution significative dans la recherche de bruit de fond, l'identification de la charge des électrons revêt une très grande importance pour les processus qui impliquent des états finaux consistant en des paires de leptons de même signe. Une estimation du taux d'erreur d'identification de la charge des électrons est présentée au moyen d'une fonction de vraisemblance, une méthode qui a déjà depuis été utilisée avec succès par la communauté d'ATLAS afin d'estimer le bruit de fond dû à une erreur d'identification de charge des électrons.

En revanche, les processus qui impliquent la production de paires de gluinos lourds sont fortement motivés par le problème de naturalité ainsi que par le fait que leurs sections efficaces de production sont élevées. Une recherche de paires de gluinos utilisant des données récoltées durant la période 2015-2016 à $\sqrt{s} = 13$ TeV et correspondant à une luminosité de $36.1$ fb$^{-1}$ est présentée. Les particules à l'état final one une grande impulsion transverse et plusieurs jets sont présents, dont au moins trois doivent être des jets-$b$. Le canal leptonique, qui nécessite en plus au moins un lepton (un électron ou un muon), est discuté en détail, y compris le schéma de suppression de chevauchement entre jet et muon en fonction du $p_T$ du muon ainsi que l'optimisation des régions de signal. Aucune découverte n'est revendiquée. Des limites indépendantes du modèle sont extraites sur la section efficace visible pour les nouveaux processus physiques, et des limites dépendantes du modèle sont extraites en fonction des masses du gluino et du neutralino. Les masses de gluinos inférieures à 1.97 TeV pour les masses de neutralinos inférieures à environ 300 GeV sont exclues avec un niveau de confiance de 95%, montrant une amélioration marquée par rapport à la même analyse en utilisant uniquement l'ensemble de données de 2015.

Les désintégrations de quarks top boostés, dans laquelle les particules filles des quarks top se trouvent près les uns des autres, vont se produire plus fréquemment dans Run 2 car l'énergie du centre-de-masse du LHC a subi une mise à niveau à 13 TeV à partir du début de 2015. Dans les recherches qui impliquent des particules supersymétriques se désintégrant en quarks top, ces désintégrations conduisent à une augmentation considérable de l'acceptation du signal lorsque des électrons se chevauchant avec des jets sont acceptés. Une discussion de la méthode et de la mesure initiale des efficacités d'identification pour les électrons se chevauchant avec des jets est présentée, représentant la première tentative de telles mesures pour les électrons produits à l'intérieur des quarks top boostés.

**Mots-clés: ATLAS, LHC, collisionneur, SUSY, charge, électrons, identification, analyse.**

# Abstract

Supersymmetry is currently the leading candidate for physics beyond the Standard Model. The LHC, operating as the highest centre-of-mass energy collider to date, has been providing physicists with ample opportunities for verifying if supersymmetry exists.

The treatment of signal electrons represents a significant part in searches for supersymmetry that involve leptons (electrons and muons) in the final state at ATLAS. In processes that can yield a final state that consists of a pair of same-sign leptons, correct electron charge measurement is extremely important, because of the potentially large contribution to the background due to (overwhelmingly) large Standard Model sources of opposite-sign dileptons. An estimation of the rate of electron charge mis-identification by a likelihood function is presented; the method has been applied to correct simulation predictions for mis-identification rates by the ATLAS collaboration.

On the other hand, processes that target gluino pair-production are highly motivated by the naturalness problem and their high cross-section at the LHC. A search on the data collected in the 2015-2016 period, at $\sqrt{s} = 13$ TeV and corresponding to an integrated luminosity of 36.1 fb$^{-1}$, is presented. The final state consists of large missing transverse momentum and multiple jets, of which at least three must be $b$-jets. The leptonic channel, which requires in addition at least one lepton (an electron or a muon), is discussed in detail, including the boosted $p_T$-dependent muon-jet overlap-removal scheme used in the analysis as well as the optimization of the signal regions. No discovery is claimed. Model-independent limits are set on the visible cross-section for new physics processes, and model-dependent limits are set for gluino and neutralino masses. Gluino masses of less than 1.97 TeV for neutralino masses below approximately 300 GeV are excluded at the 95% CL, showing an improvement over the same analysis using the 2015 dataset alone.

Boosted top quark decays, in which the daughter particles of the top quarks are found close to each other, were expected to occur more frequently as the centre-of-mass of the LHC underwent an upgrade to 13 TeV starting early 2015. In supersymmetry searches that involve supersymmetric particles decaying into the Standard Model top quarks, such decays lead to a considerable increase in signal acceptance as electrons overlapping with jets are selected. A discussion of the method and the initial measurement of the identification

efficiencies for electrons overlapping with jets is presented, representing the first attempt at such measurements for electrons produced inside boosted top quarks.

# Contents

# List of tables

# List of figures

17

# Liste des sigles et des abréviations

ALICE    A Large Ion Collider Experiment.

ATLAS    A Toroidal LHC Apparatus.

CERN    European Organization for Nuclear Research.

LHC    Large Hadron Collider.

CMS    Compact Muon Solenoid.

CR    Control Region.

EM    Electromagnetic.

HLT    High-level Trigger.

ID    Inner Detector.

LEP    Large Electron-Positon Collider.

LHCb            Large Hadron Collider beauty.

pdf             Probability Distribution Function.

QCD             Quantum Chromodynamics.

QED             Quantum Electrodynamics.

SCT             Semiconductor Tracker.

SR              Signal Region.

TRT             Transition Radiation Tracker.

SUSY            Supersymmetry.

VR              Validation Region.

# Acknowledgement

I would like to begin by thanking my supervisor Jean-François Arguin. Not only is Jean-François a great scientist, he is a great supervisor as well, and I am forever grateful for his kind and patient support and guidance over the past years. The group of experimental particle physics at the Université de Montréal is a dedicated group, and the dedication of the professors, Claude Leroy and Georges Azuelos (and of course Jean-François), to research and teaching has always filled me with a deep admiration. I would like to take this opportunity to thank Claude and Georges for their kind support over the past years as well. Claude, professor Paul Charbonneau, and professor Manu Paranjape were in my predoc committee, and I will never forget their encouragement.

I am also enormously thankful to other students at the department of physics whom I have had the opportunities to know over the years. Louis-Guillaume, Dominique, Chloé, Thomas, Benjamin, Kazuya, Otilia, Léa, Merlin, Reyhaneh, Fatemeh, Frédérick, Hubert, Jérôme, and Jacinthe. I have learned many things from them. During my entire study, I have had chances to interact with physicists and students from all corners and I really appreciate every interaction.

Finally, I would like to thank my mom, my dad, and my brother, who have always been a source of comfort and encouragement for me. My brother, Tu, has been in Montréal with me since the beginning of my study and I'm thankful for that.

# Chapter 1

# INTRODUCTION

For centuries philosophers and scientists, among them physicists, have pursued the idea that there is a simplicity underneath the apparent complexity of natural phenomena. This quest for simplicity, which to many is also a quest for beauty, have led physicists to contemplate the universe at ever smaller and ever larger scales. As they progress, physicists have become more and more convinced that their quest is fruitful, that a satisfactory picture of the physical world is attainable, even though major paradigm shifts have occurred many times over.

In the search for a theoretical understanding of physical phenomena at ever smaller scales, particle physicists have been guided by the idea that matter is made up from a small number of elementary particles, that these particles interact through certain fundamental forces, and that a knowledge of the elementary particles and their fundamental interactions is equivalent to a full understanding of the physical world.

This simple yet profound idea, that all one needs to know is a knowledge of the elementary particles and their fundamental interactions, has been implemented quantitatively. In the second half of the 20th century, particle physicists have been able to construct a theoretical framework, the Standard Model, in which the elementary particles and their interactions are identified and classified, and on the basis of which many calculations have been carried out with outstanding precision. The calculation of the magnetic moment of the electron is a famous example: The agreement between theoretical calculation and experimental measurement has reached the level of ten decimal figures [1], among the most precise in physics.

According to the Standard Model, there is a small number of elementary particles, classified into bosons and fermions. Fermions, which are the constituents of matter, carry spin 1/2 and, depending on their properties, interact with each other by one or more fundamental forces by exchanging bosons. The bosons, which have integer spins, are thus the force carriers. Bosons may themselves carry electric or color charges, making those that

do capable of interacting with each other. Particle physicists have, to a great extent, succeeded in proposing and clarifying, both qualitatively and quantitatively, these elementary interactions. More remarkably, they have found in the process that symmetry is a unifying principle of the Standard Model. The entire theoretical framework of the Standard Model is constrained by spacetime symmetries, the Poincaré group, and local gauge symmetries, the groups $U(1)$, $SU(2)$, and $SU(3)$, underlie its different components.

To particle physicists, the Standard Model, even though a fantastic achievement of 20th-century physics that ranks among the greatest intellectual achievements of all time, is not absolutely satisfactory. First of all, presently we know that there are four fundamental forces that exist in nature. The electromagnetic force takes place between particles that carry electric charges. Subatomic forces, i.e. the weak and the strong forces, take place between particles that carry the weak and the strong charges, respectively. The electromagnetic and the weak forces have been unified into a single force called the electroweak force, and together with the strong force, make up the three fundamental forces in the Standard Model. Gravity, a fundamental force that takes place between any two particles that carry masses, is however not part of the Standard Model. In this sense, the Standard Model is not seen as a complete physical theory of nature.

There are other problems with the Standard Model as well. Neutrino masses, the hierarchy problem, the nature of dark matter, the unification of the electromagnetic, weak, and strong forces, are questions whose answers are believed to lie beyond the scope of the Standard Model.

Among the many ideas that have been proposed, supersymmetry is perhaps the one that stands out and one that is most actively pursued. It is a theoretically consistent framework that centers on the question whether or not it would be possible to extend spacetime symmetries. Indeed, gauge symmetries are not related to spacetime symmetries, in the sense that the commutators between the generators of the gauge groups and those of the Poincaré groups all vanish. Spacetime symmetries may be extended, provided, along with adding new generators to the spacetime generators, we consider their anti-commutators. Supersymmetry unifies bosons and fermions, thereby in a sense further simplifying our picture of the physical world. It, however, adds some complexity into our perception of nature with a considerable increase in the number of elementary particles. At the same time, supersymmetry might play an important role in the solutions to a number of open questions that have been raised, such as the hierarchy problem, dark matter, and the unification of the three fundamental forces of the Standard Model.

For any physical theory, the ultimate test is experiments. Since its operation in 2009, the Large Hadron Collider (the LHC) based at CERN, as the world's largest and highest-energy particle collider, has given physicists opportunities to verify if supersymmetry is indeed a symmetry of nature. A great number of physicists is participating in this process, which is

still going on, by analyzing the data that have been collected and are being collected at the LHC, searching for signs if supersymmetry exists.

The LHC centre-of-mass energy makes it possible to probe a number of physics models that extend the Standard Model. Many of these models predict unstable hypothetical particles that decay into Standard Model particles such as the top quarks and weak bosons, which are also produced from pure Standard Model processes and which, being unstable themselves, decay either leptonically or hadronically. Such leptonic processes, expected in a fraction of the total number of interactions, can produce electrons and muons. Because of their clean experimental signature, especially since most particles produced at the LHC are hadrons, electrons and muons are important physics objects in the search for new physics and need to be accurately reconstructed and calibrated.

The common theme of this thesis is electrons, specifically improving the handling of signal electrons in SUSY searches[1]. It is one among many works that have been carried out by experimental physicists at CERN as the search for supersymmetry continues. The context of the present study is:

- Several SUSY processes can yield a final state consisting of a pair of same-sign leptons, where the leptons are electrons and muons. In general, SUSY cross sections are much smaller than the Standard Model background cross sections. As we continue to push to unexplored phase space, we often have to deal with situations that involve a small signal on top of a large background. Correct determination of the charges of the leptons in these searches is essential. In ATLAS, electron charge is determined from the curvature of the track reconstructed in the Inner Detector (which is embedded in a solenoidal magnetic field). This determination is not always correct, however, due to the apparent straightness of the track or bremsstrahlung, and as a result the sign of the charge could be mis-measured, or mis-identified. Electron charge mis-identification rates occur on the order of $O(1\%)$, while Standard Model processes that provide opposite-sign dileptons (dominantly $Z \rightarrow e^+e^-$ bosons) occur approximately $10^3$ times more commonly than genuine Standard Model sources of same-sign leptons (dominantly $WZ$ production). Accordingly, opposite-sign sources of dileptons can constitute a large background to final states that involve same-sign lepton pairs. In this thesis, an estimation of the rate of charge mis-identification by a likelihood function is described in Chapter 5.
- Many SUSY searches target strongly-interacting processes because of their relatively high cross sections. Processes that involve pair productions of gluinos, which are hypothetical partners of the Standard Model gluons, is an example. The searches for these superpartners are also highly motivated as they are expected by naturalness

---

[1] The work is applicable to other beyond-the-Standard-Model searches.

to have a mass around the TeV scale [**2**], and as such are producible at the LHC. This thesis describes, in Chapter 6, a search in which the final state consists of large missing transverse momentum due to the neutralino, as well as multiple jets, where at least three of the jets must be $b$-jets. The focus is on the leptonic channel[2] where electrons and muons are involved, and we describe in some detail a new scheme of overlap removal between jets and muons that was introduced into the analysis, to maximize signal acceptance in the presence of boosted top quarks.

In the same chapter we also discuss the optimization of some important discriminating variables which were used in the design of the signal regions of the analysis. The analysis result for the data collected in the period 2015-2016, at 13 TeV centre-of-mass energy and corresponding to an integrated luminosity of 36.1 fb$^{-1}$, is also presented.

- Starting from Run 2, the LHC centre-of-mass was upgraded to 13 TeV. In a number of SUSY searches that involve leptons in the final state, including the search that targets pair productions of gluinos mentioned above, more electrons were found inside jets, and selecting such electrons has led to a considerable increase in signal acceptance. At ATLAS, only electrons non-overlapping with jets are calibrated, and it is important to make sure that this calibration, in particular for the identification efficiencies, remains valid for electrons found inside jets. This thesis, specifically Chapter 7, develops a method for measuring the identification efficiencies for electrons found inside jets and performs the initial measurement. The measurement uses a dilepton $(e\mu)$ $t\bar{t}$ sample enriched in boosted top quarks[3], and the electrons selected for the measurement are located inside the $b$-quarks from the decays of the top quarks.

  Prior to the work initiated in this thesis, no attempt had been made to measure the identification efficiencies for electrons produced inside boosted top quarks.

The remaining chapters are organized as follow. Chapter 2 discusses briefly the symmetry principles that underlie the Standard Model, as well as its particle contents and forces. In the same chapter we also present a general discussion of the shortcomings of the Standard Model, as well as a discussion of the basic ideas of supersymmetry. Chaper 3 describes the LHC, including a discussion of the LHC accelerator and the ATLAS detector. All the works in this thesis are associated with the ATLAS experiment. Chapter 4, on the other hand, presents an introduction to electron reconstruction and identification at ATLAS.

---

[2]The hadronic channel which requires zero lepton is also part of the analysis; however, the chapter only focuses on the leptonic channel as it is directly related the work done in this thesis.
[3]The top quark decays almost all of the time into a $W$ and $b$-quark.

# Chapter 2

---

# THE STANDARD MODEL OF PARTICLE PHYSICS AND SUPERSYMMETRY

The LHC was designed to explore the Standard Model physics, including the Higgs boson, and to search for some beyond-Standard-Model physics accessible at the TeV scale. The theoretical foundation underlying these interactions was worked out by physicists in the second half of the 20th century and laid out in the Standard Model of particle physics, a mathematical framework that makes possible quantitative predictions of particle interactions. This chapter touches on some aspects of the Standard Model, including the principle of symmetry, which is an important organizing principle of the Standard Model.

On the other hand, it is well-known that there are issues concerning the Standard Model. Some of these are reviewed in the present chapter. Supersymmetry, one among several attempts to go beyond the Standard Model, provides potential answers to some of these issues. Supersymmetry has been and still is being actively pursued at the LHC. The theory of supersymmetry, including some key points on phenomenology, is discussed briefly at the end of the chapter.

## 2.1. The Standard Model of Particle Physics

The known elementary particles and their fundamental interactions, excluding gravity, are fully represented in the Standard Model [3, 4, 5]. The concept of symmetry plays an essential role, as each component of the Standard Model — QED (quantum electrodynamics), the weak interaction, and the strong interaction (quantum chromodynamics, or QCD) — can be obtained by imposing an appropriate symmetry, a so-called local gauge symmetry; in addition, each component also respects spacetime symmetries [6]. Section 2.1.1 discusses briefly spacetime symmetries as well as the local gauge symmetries that underline the Standard Model, while Section 2.1.2 discusses in some detail the particle contents of the Standard Model as well as several of its aspects.

## 2.1.1. Symmetries

A symmetry is mathematically represented by a group. Spacetime symmetries are represented by the Poincaré group, and local gauge symmetries are represented by local gauge groups. They are discussed in the following.


2.1.1.1. The Poincaré Group. Spacetime symmetries include the Lorentz symmetry, which refers to the equivalence between inertial observers with regard to physical laws. If $K$ and $K'$ are inertial frames, the relativity principle requires physical laws as observed in $K$ to be the same physical laws as observed in $K'$. Thus, let $x, y, z$ and $t$ be the coordinates of an event as measured in $K$, and $x', y', z'$ and $t'$ those of the same event as measured in $K'$. According to special relativity, these coordinates are related by a Lorentz transformation

$$x'^{\mu} = \Lambda^{\mu}_{\nu} x^{\nu}.$$

The Lorentz transformations form a group, called the Lorentz group. They are formally transformations that leave the four-dimensional distance

$$\eta_{\mu\nu} x^{\mu} x^{\nu} = (ct)^2 - x^2 - y^2 - z^2$$

invariant ($c$ is the speed of light). Physically, Lorentz symmetry concerns rotations and boosts between inertial frames.

To the Lorentz symmetry may be added possible displacements of the origins of the frames, including time and spatial displacements,

$$x'^{\mu} = x^{\mu} + a^{\mu}.$$

In this way, the full spacetime symmetries, or Poincaré symmetry, are obtained. The corresponding group is called the Poincaré group.

A physical theory is said to be constrained by spacetime symmetries if its Lagrangian is invariant with respect to the Poincaré group. This applies to the Standard Model physics as well as physics that extends it. This concept will be illustrated below when we discuss gauge groups in the context of the Standard Model physics.


2.1.1.2. Gauge Groups. The known fundamental interactions in the Standard Model, namely quantum electrodynamics, the weak force, and the strong force, have been discovered to follow the principle of symmetry, in the sense that each of them can be obtained when an appropriate symmetry is required. The associated symmetry groups can be classified into abelian groups and non-abelian groups. In this section we review some general considerations in the use of such groups.

The Abelian group $U(1)$. The global $U(1)$ group arises when we consider a transformation of the form

$$\psi \to e^{i\theta}\psi, \tag{2.1.1}$$

where $\theta$ is a real number. The gauge principle turns $\theta$ into a function of spacetime coordinates, $\theta(x)$, where $x = (ct, \mathbf{x})$, and the resulting transformation is called a local gauge transformation. In a theory that makes use of this symmetry, the Lagrangian of the theory is required to be invariant under this local gauge transformation.

We will consider as an example the Dirac Lagrangian

$$L = \bar{\psi}(i\gamma^\mu \partial_\mu - m)\psi, \qquad \mu = 0, 1, 2, 3$$

which conforms to spacetime symmetries, but which is not invariant under the local gauge transformation just discussed, since the transformed Lagrangian is

$$L' = L + \bar{\psi}\gamma_\mu\psi(\partial^\mu\theta).$$

To arrive at a new Lagrangian that would be invariant, we introduce a new field, called a gauge field and denoted $A_\mu$, together with the covariant derivative operation

$$D_\mu = \partial_\mu + ieA_\mu,$$

and the requirement that under the local gauge transformation, the $A_\mu$ would have to transform according to

$$A_\mu \to A'_\mu = A_\mu + \frac{1}{e}\partial_\mu\theta.$$

The kinematics of $A_\mu$ will be taken into account in the new Lagrangian through the term

$$-\frac{1}{4}F_{\mu\nu}F^{\mu\nu},$$

where, by definition,

$$F_{\mu\nu} = \partial_\mu A_\nu - \partial_\nu A_\mu.$$

The new Lagrangian that would be invariant under the local gauge transform is

$$L = \bar{\psi}(i\gamma^\mu D_\mu - m)\psi - \frac{1}{4}F_{\mu\nu}F^{\mu\nu}.$$

This Lagrangian is actually the Lagrangian of QED. The field $A_\mu$ represents the photon. If the covariant derivative is expanded we will see in the Lagrangian the term $e\bar{\psi}\gamma_\mu\psi A^\mu$, which involves not only the photon term $A_\mu$ but also the charged fermion terms $\bar{\psi}$ and $\psi$; it represents the elementary electromagnetic interaction and expresses the fact that at the most fundamental level currently known, electrodynamic interactions are to be understood in terms of one simple elementary interaction that always involves a photon and a pair of charged fermions. This knowledge is also usually expressed graphically in Figure 1 where the wiggly line depicts the photon, and the two straight lines with arrows depict the charged

particles. This single diagram encodes different possibilities, we may understand it as the annihilation of a charged particle-anti-particle pair in which a photon is seen at the end, or a process in which a charged particle radiates a photon, or a process where the photon radiates a pair of particle-antiparticle.[1]
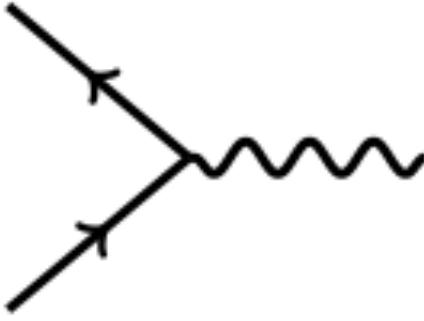


**Fig. 1.** The Elementary QED vertex

Non-Abelian Groups $SU(n)$. $SU(n)$ may be understood as the group of all $n \times n$ unitary matrices whose determinants equal 1. Such a matrix, say $U$, may be written in the form

$$U = \exp\left(-i\frac{T^a}{2}\alpha^a\right).$$

The gauge principle turns the parameters $\alpha^a$'s into functions of spacetime coordinates $\alpha^a(x)$'s. The $T^\alpha$ are called the generators of the group and satisfy the relations

$$[T^a, T^b] = i f_c^{ab} T^c.$$

As in the case of QED discussed earlier, in order to write down a Lagrangian that would be invariant under the local gauge transformation $SU(n)$, we are forced to introduce new fields that represent bosons in the theory, the number of bosons corresponding to the number of generators of the group, plus the covariant derivative operation and the kinematic terms involving these fields. The possible elementary interactions of the theory may then be read off by looking at the various terms in the Lagrangian. In QCD, for example, where the gauge group is $SU(3)$, there are eight generators that correspond to eight gluons in the theory. Apart from a quark-gluon vertex as shown in Figure 2, which is of the type seen in QED, there are the three-point vertex and four-point vertex, shown in Figure 3, that correspond to gluon self-interactions; these additional self-interactions are characteristic of non-Abelian interactions.

---

[1]Photon emission and photon conversion to electron-positron pair are important to physics at the LHC.
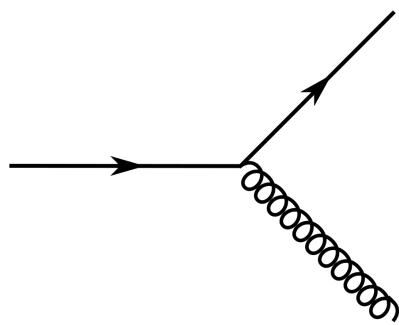
**Fig. 2.** The QCD quark-gluon vertex
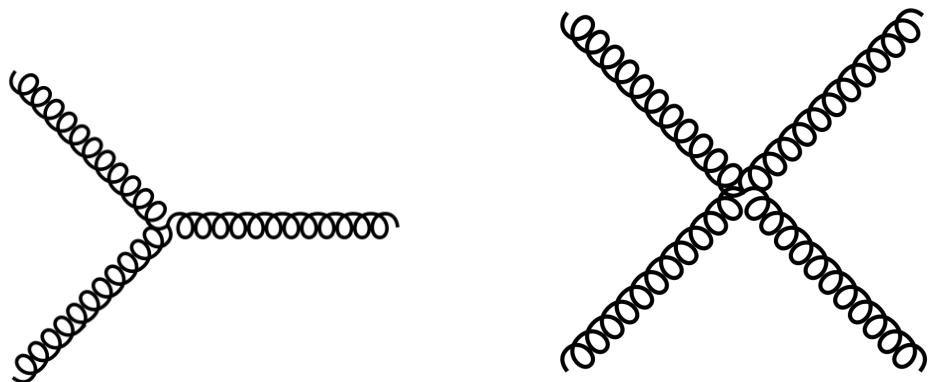


**Fig. 3.** The QCD gluon self-interactions

## 2.1.2. The Standard Model Particles and Forces

The Standard Model is the quantitative implementation of the idea that physics is to be understood in terms of a small number of elementary particles and their fundamental interactions. The elementary particles are classified into fermions and bosons. Fermions are further classified into three families, each family is made up of a pair of leptons and two quarks; they are listed in Table 1.

| Leptons | | | | Quarks | | | |
|---|---|---|---|---|---|---|---|
| | Particle | | Mass | Charge | Particle | | Mass | Charge |
| I | electron | $e$ | 0.511 MeV | -1 | Up | $u$ | 2.3 MeV | $+\frac{2}{3}$ |
| | $e$ neutrino | $\nu_e$ | < 2 eV | 0 | Down | $d$ | 4.8 MeV | $-\frac{1}{3}$ |
| II | muon | $\mu$ | 105.658 MeV | -1 | Charm | $c$ | 1.275 GeV | $+\frac{2}{3}$ |
| | $\mu$ neutrino | $\nu_\mu$ | < 2 eV | 0 | Strange | $s$ | 95 MeV | $-\frac{1}{3}$ |
| III | tau | $e$ | 1776.82 MeV | -1 | Top | $t$ | 173.07 GeV | $+\frac{2}{3}$ |
| | $\tau$ neutrino | $\nu_\tau$ | < 2 eV | 0 | Bottom | $b$ | 4.18 MeV | $-\frac{1}{3}$ |

**Table 1.** The Standard Model fermions. All are spin 1/2 particles.

The only difference between the families is the masses of the particles, and it is still an open question why three families in fact exist.

The bosons mediate the forces between the fermions. They carry integer spins, and are listed in table 2.

| Particle | | Mass | Charge | Spin |
|---|---|---|---|---|
| Photon | $\gamma$ | 0 GeV | 0 | 1 |
| $W^\pm$ | | 80.385 GeV | $\pm 1$ | 1 |
| $Z$ | | 91.1876 GeV | 0 | 1 |
| Gluon | $g$ | 0 GeV | 0 | 1 |
| Higgs | $h$ | 125.9 GeV | 0 | 0 |

**Table 2.** The Standard Model bosons. All have integer spins.

The fundamental interactions are QED, QCD, and weak interactions, mediated by the photon, the gluons, and the weak gauge bosons respectively. QED and the weak theory have been unified into a single electroweak theory. The relevant gauge groups are $SU_L(2) \otimes U_Y(1)$ for electroweak and $SU_C(3)$ for QCD. It is a general property of local gauge theories that the gauge bosons are massless. The photon and the gluons are massless, but the weak bosons are not. This contradictory fact was resolved with a mechanism known as spontaneous symmetry breaking [**7, 8, 9**], in which the electroweak group $SU_L(2) \otimes U_Y(1)$ is broken to the group $U_{em}(1)$. The result is the introduction of a new scalar field, the Higgs field, whose interactions with elementary particles would give them masses. The particles associated with the Higgs field are called the Higgs particles. The Higgs boson was discovered in 2012 [**10, 11**], its mass has been measured to be $\sim 125$ GeV, giving a confirmation of electroweak unification as well as the role of the Higgs field in giving masses to elementary particles.

## 2.2. Beyond the Standard Model

The Standard Model has been tested very extensively in terms of its quantitative predictions of elementary particle interactions, and has hitherto withstood all the tests. It is,

however, not the ultimate physics theory in which many of our important questions about the physical world can be answered satisfactorily. This section discusses some problems that cannot be answered within the framework of the Standard Model; the section also discusses supersymmetry, an attempt to go beyond the Standard Model to address some of the questions that we still have.

## 2.2.1. Problems with the Standard Model

Gravity. A law of gravitational interactions was first proposed by Newton. A mass $M$ was postulated to exert an attractive force on another mass $m$, given by

$$\mathbf{F} = -G\frac{Mm}{r^2}\hat{\mathbf{r}}$$

where $\hat{\mathbf{r}}$ is the unit vector pointing from $M$ to $m$, and $G$ the gravitational constant. Einstein proposed a fundamental change to the understanding of gravitational interactions, in which forces are completely eliminated [12]. In general relativity there is a direct link between the distribution of matter and energy in a spacetime region to the geometry of spacetime, the link being given according to the equation

$$G_{\mu\nu} = -\kappa T_{\mu\nu}, \qquad \mu, \nu = 0, 1, 2, 3$$

where $\kappa = 8\pi G/c^4$, $T_{\mu\nu}$ is the energy-momentum tensor, and

$$G_{\mu\nu} = R_{\mu\nu} - \frac{1}{2}Rg_{\mu\nu}$$

is the Einstein tensor, which has been written in terms of the Ricci tensor $R_{\mu\nu}$ and the curvature scalar $R$, both of which are functions of the metric tensor $g_{\mu\nu}$ which characterizes a spacetime geometry. In this new scheme the paths of objects follow the geodesics of a spacetime geometry.

Gravitational interactions are not accounted for in the Standard Model. Even though these interactions are well-understood for macroscopic objects, there is still a lot of debate as to whether or not a truly successful and testable quantum theory of gravity has been or will ever be attained. In any case, gravity is not part of the Standard Model, and as long as we are still searching for a single, all-encompassing theoretical framework to address all of our questions about the physical world, the Standard Model is not a complete theory.

The hierarchy problem [13, 14]. At the energy scale of the LHC, gravitational interactions are completely negligible. A rough comparison between the gravitational force between two equal masses $M$ separated by a distance $r$, which is $GM^2/r^2$, with the electrostatic force between two charges $|e|$ separated by a distance $r$, which is $e^2/r^2$, will indicate the relative weakness of gravity. Indeed, taking as the unit of mass $Mc^2 = 1$ GeV, the electromagnetic

coupling

$$\alpha = \frac{e^2}{4\pi\hbar c} = \frac{1}{136.036}$$

is to be compared with

$$\frac{GM^2}{4\pi\hbar c} = 5.3 \times 10^{-40}.$$

It follows that gravity is negligible at the GeV or TeV scale. In fact, gravitational interactions are negligible up to the Planck scale $(hc/G)^{1/2} \sim 10^{19}$ GeV. Given that there are only four forces currently known that span from the scale of a few hundreds GeV to the Planck scale, it might seem reasonable to assume that any additional force in between should have been discovered, and accordingly the Standard Model physics could be assumed to be valid up to Planck scale, i.e. up to that scale there is no new physics. However, it has been pointed out that this assumption leads to the following issue.

In quantum field theory the physical mass of an elementary particle is the sum of its bare mass plus the corrections due to interactions. The Higgs is self-interacting and due to its mass receives a major correction from self-interaction; in addition it receives another major correction from its interaction with the top quark, the heaviest Standard Model particle. If $\mu$ denotes the Higgs mass, $\mu_B$ its bare mass, then the corrections have been determined to take the form

$$\mu^2 \simeq \mu_B^2 + \frac{\lambda}{8\pi^2}\Lambda^2 - \frac{3y_t^2}{8\pi^2}\Lambda^2 + \ldots$$

where $\Lambda$ is the momentum scale up to which the corrections are applied, $\lambda$ is the Higgs coupling strength, and $y_t$ is the coupling strengh between the top and the Higgs. If $\Lambda$ is taken to be the Planck scale, the corrections have to be extremely precise to fit the physical Higgs mass $\mu \sim 100$ GeV. This is referred to as the hierarchy problem.

Dark matter. Astronomical and cosmological measurements accumulated over the years [**15, 16, 17**] have argued overwhelmingly for the inadequacy of ordinary matter to account for the total matter in the universe. Indeed, currently it is estimated that Standard Model particles account for only about 5% of all matter in the universe, while dark matter and dark energy account for the rest, about 27% and 68% respectively [**18, 19**]. At present, the nature of dark matter is still unknown, even though there is considerable indirect cosmological evidence that points to its existence. Thus, for instance, theoretically we expect to see a smaller rotational velocity of objects that are increasingly distant from the galaxy to which they belong, shown by the disk line in Figure 4. Actual measurements, however, have shown that the rotational curve is rather flat, as indicated by the NGC 3198 line in the same figure. It is thus concluded that there is invisible mass that not only cannot be seen but is also distributed differently from ordinary matter.

There are many other examples as well, among which gravitational lensing furnishes another convincing evidence that indicates the existence of dark matter. The amount of

deflection of light from distant galaxies may be used to estimate the amount of matter in the galaxy clusters between the Earth and the distant galaxies, and has led to the conclusion that the galaxy clusters are in co-existence with an enormous amount of dark matter [**15, 16, 17, 18, 19**].

DISTRIBUTION OF DARK MATTER IN NGC 3198
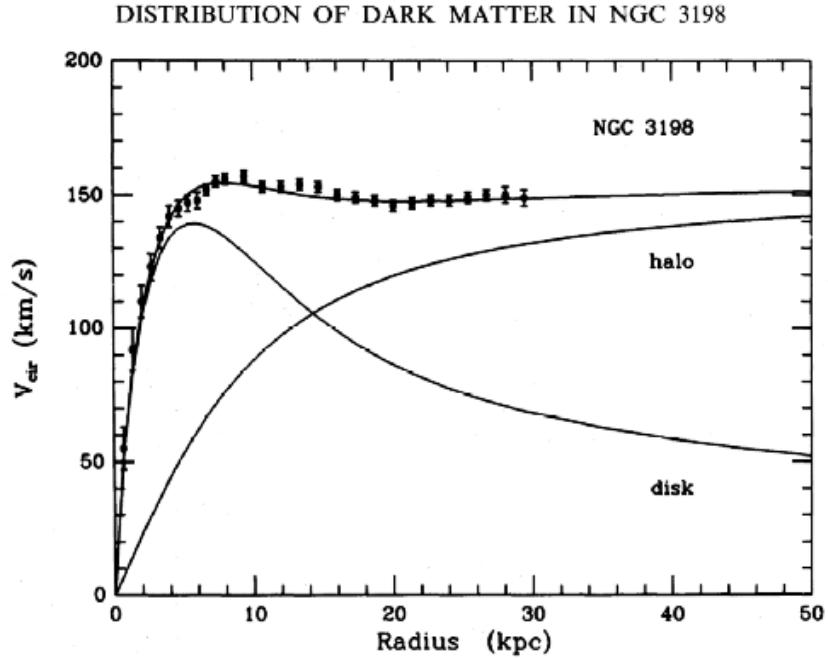


**Fig. 4.** The rotation curve of NGC 3198 [**20**].

The majority of dark matter is expected to be cold dark matter made up of non-relativistic particles. Most Standard Model particles are not dark matter candidates except the neutrinos, which are both stable and weakly interacting. However, neutrinos are relativistic particles and might only account for the so-called hot dark matter, which is only a small fraction of the total amount of dark matter.

## 2.2.2. Supersymmetry

Supersymmetry [**21, 22, 23, 24, 25, 26**] is an extension of the Standard Model that offers potential solutions to many currently unsolved problems [**27, 28, 29, 30, 31**]. It centers around the question whether or not spacetime symmetries, the Poincaré group, can be extended in a non-trivial way. This is to be contrasted with gauge symmetries, which are trivial extensions of spacetime symmetries, in the sense that the generators of the gauge groups commute with the generators of the Poincaré group.

This section gives a brief discussion of supersymmetry. A more complete reference is provided in Ref. [**32**].

The Poincaré Algebra and Supersymmetry. The Poincaré group, as discussed in Section 2.1.1.1, is made up of the Lorentz group and the group of spacetime translations. The elements of the groups are functions of ten real continuous parameters, six coming from rotations and boosts in the Lorentz group, and four from the translation group. Mathematically the Poincaré group is associated with a set of ten generators, six associated with the Lorentz group and usually denoted $J^{\mu\nu}$, and four associated with the translation group, which will be denoted $P^\mu$. Among these generators there exist commutation relations

$$[P^\mu, J^{\rho\sigma}], \quad [P^\mu, P^\nu], \quad [J^{\mu\nu}, J^{\rho\sigma}]$$

whose expressions involve only the generators $J^{\mu\nu}$ and $P^\mu$. The generators and the commutation relations are said to form the Poincaré algebra. The question of the extension of the Poincaré group becomes the question of whether or not new generators could be added to the existing set of generators, such that the new commutation relations that arise are not all trivial, and that they are expressions that involve only the old and the new generators.

The Poincaré algebra has been found to be extensible, but on the condition that, when adding the new generators, we have to consider not only the commutation relations between the old and the new generators, but also the anticommutation relations among the new generators themselves. The result is a set of generators and commutation and anticommutation relations among them that form a system called the super-Poincaré algebra. One of the consequences that follows is that the new generators map bosons into fermions and vice versa. Theoretical considerations then require supersymmetric theory to contain only two possible multiplets, the chiral supermultiplet that consists of two scalar and two spinor fields, or the vector supermultiplet that consists of two spinor and two vector fields[2]. It has been found necessary, also on theoretical ground, to introduce one or more new particles for every Standard Model particle that differs by spin 1/2, called its superparners. The particles in a multiplet otherwise have the same mass and other quantum numbers.

Supersymmetry may be classified depending on the number of new generators that are added to the Poincaré generator. The case where there is only one new generator added is called $N = 1$ supersymmetry. The Minimal Supersymmetric Standard Model (MSSM) is $N = 1$ supersymmetry [**32, 33**], it is the extension of the Standard Model with the least possible number of new particles that need to be introduced. The particle contents are listed in Table 3.

---

[2]If only one supersymmetric generator is considered.

| | Boson | | Fermions | $SU(3), SU(2), U(1)$ |
|---|---|---|---|---|
| Gluons | $g$ | Gluinos | $\tilde{g}$ | $(8, 1, 0)$ |
| Gauge bosons | $W^{\pm}, W^0$ | Gauginos | $\tilde{W}^{\pm}, \tilde{W}^0$ | $(1, 3, 0)$ |
| B boson | $B$ | Bino | $\tilde{B}$ | $(1, 1, 0)$ |
| Sleptons | $\tilde{\nu}_L, \tilde{e}_L$ | Leptons | $\nu_L, e_L$ | $(1, 2, -1)$ |
| | $\tilde{\bar{e}}_L$ | | $\bar{e}_L$ | $(1, 1, -2)$ |
| Squarks | $\tilde{u}_L, \tilde{d}_L$ | Quarks | $u_l, d_L$ | $(3, 2, \frac{1}{3})$ |
| | $\tilde{u}_R$ | | $u_R$ | $(3, 1, \frac{4}{3})$ |
| | $\tilde{d}_R$ | | $d_R$ | $(3, 1, \frac{-2}{3})$ |
| Higgs | $H_d^0, H_d^-$ | Higgsinos | $\tilde{H}_d^0, \tilde{H}_d^-$ | $(1, 2, -1)$ |
| | $H_d^+, H_u^0$ | | $\tilde{H}_u^+, \tilde{H}_u^0$ | $(1, 2, 1)$ |

**Table 3.** Particles in the MSSM. Mixing of the interaction eigenstates are possible, for examples the Higgsino and the gaugino fields mix to form the neutralino $\tilde{\chi}_i^0$ and the chargino $\tilde{\chi}_i^{\pm}$ mass eigenstates (not shown in the table).

If supersymmetry exists, it has to be broken, for otherwise supersymmetric particles would have been detected alongside Standard Model particles. Supersymmetry is thought be broken spontaneously, analogously to the way the Standard Model electroweak theory is broken spontaneously. A more detail discussion on supersymmetry breaking is provided in Ref. [**32**].

Supersymmetry Phenomenology at the LHC. At the LHC, a class of MSSM models known as $R$-parity conserving models figures predominantly. $R$-parity [**32, 33**] is a multiplicative quantum number defined by

$$P_R = (-1)^{3(B-L)+2S}$$

where $B$ is the baryon number, $L$ the lepton number, and $S$ the spin. Then each Standard Model particle is assigned the value $+1$ while each supersymmetric particle the value $-1$. Phenomenologically, $R$-parity conservation implies that

- The lightest supersymmetric particle (LSP) is stable;
- All other supersymmetric particles decay into a state that has an odd number of LSPs;
- Supersymmetric particles are produced in pairs.

In phenomenologically viable models, the LSP does not participate in known interactions and manifests itself as missing transverse energy in a detector. It is a good candidate for dark matter. At the LHC, both strong and electroweak interactions are expected to produce supersymmetric particles, where the former is expected to dominate. Many searches for supersymmetric particles have been carried out since the start of the LHC, many of which are motivated by SUSY solution to the hierarchy problem (Section 2.2.1). In this scenario,

the superparners reachable at the LHC fall into the so-called natural SUSY spectrum, shown in Figure 5, in which the gluinos are among the candidates most likely to be discovered early. A SUSY search for gluino pair-production will be discussed in Chapter 6 of this thesis.
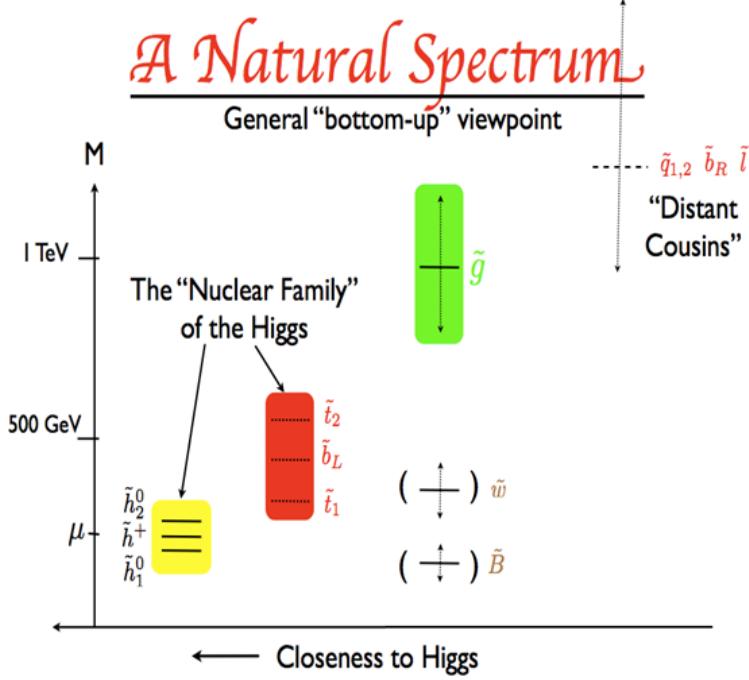


**Fig. 5.** The natural SUSY mass spectrum [**34**].

Ref. [**35**] provides a detailed discussion of SUSY and its solutions to the hierarchy problem, grand unification, and dark matter.

# Chapter 3

---

# LHC AND THE ATLAS DETECTOR

Among the principal instruments of modern experimental particle physics are accelerators and detectors. Accelerators accelerate particles to some energy before colliding them, and subsequently the collision debris in the form of new particles are collected and analysed in the detectors. A high centre-of-mass energy, which is required to reach high mass scale physics, leads to many technical challenges as well as an increase in the overall complexity of modern accelerators and detectors.

This chapter discusses the Large Hadron Collider (LHC) based at CERN and the ATLAS detector, one among the four main detectors located at the LHC.

## 3.1. CERN AND THE LARGE HADRON COLLIDER

Broadly speaking, the development of physics rests upon two sources, the first, the availability of a set of physical phenomena and the second, active theoretical investigations. At the turn of the 20th century, atomic phenomena confirmed the discrete nature of physical quantities previously thought to be continuous and motivated the development of quantum mechanics. Subsequently, the quest to unify quantum mechanics and special relativity, in parallel with probes into sub-atomic phenomena, led to the development of quantum field theory and eventually gave birth to the Standard Model of particle physics. At present, more than ever before, both technological advances and active theoretical investigations are being pushed to the limit to scrutinize the Standard Model and go beyond it. In this respect, the Large Hadron Collider based at CERN has been playing a leading role, being the most powerful collider to date.

CERN [36], also known as European Organization for Nuclear Research, was established in the post-war era, the 1940s, to foster physics development and scientific collaboration in Europe. The Large Hadron Collider [37] at CERN was designed to explore physics beyond the Standard Model and Higgs physics. It is a complex of successive accelerators that increase

the accelerated particle energy by approximately an order of magnitude at each pass from one accelerator to the next.

The LHC reuses the Large Electron Position (LEP) tunnel, which produced $e^+e^-$ collisions. It is 26.7 km in circumference and lies between 45 m and 170 m underground. The designed centre-of-mass energy is 14 TeV, at which Higgs physics and some beyond the Standard Model physics are accessible. It has two rings with counter-rotating proton beams. The beams are accelerated by a high-frequency standing wave, and by design take the form of bunches of particles, which are spaced by 25 ns and each of which contains up to $1.1 \times 10^{11}$ protons. The beam particles are kept along a circular trajectory using dipole magnets; in addition they are focused near the collision points using quadrupole magnets. Notable at the LHC is the use of superconducting magnets that operate at 1.9K.

Figure 1 shows the CERN's accelerator complex. The four main detectors are ATLAS, CMS, ALICE, and LHCb, all located at different collision points. Among them, the general-purpose experiments are ATLAS and CMS.
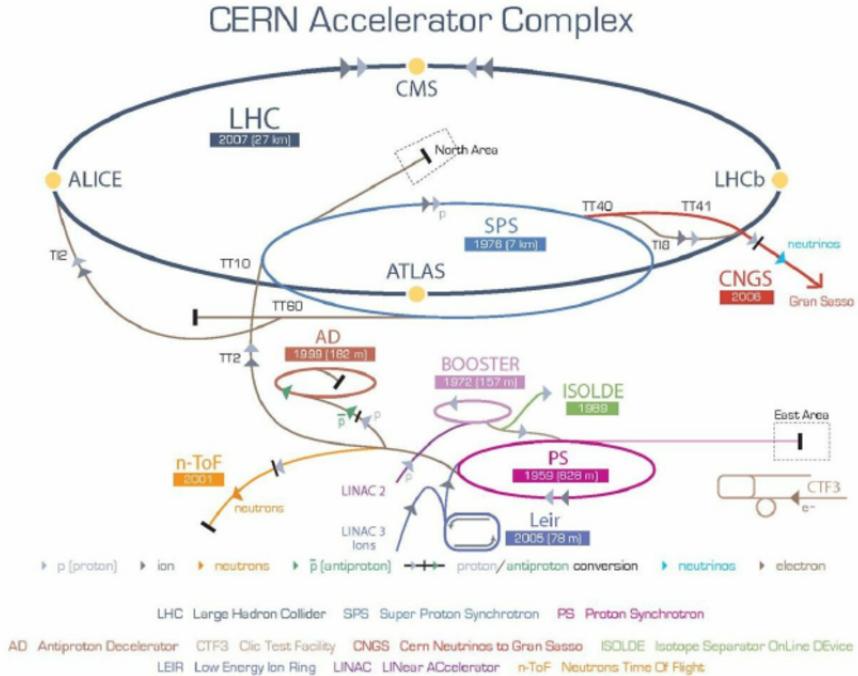


**Fig. 1.** CERN's Accelerator Complex
[**38**]

Initially in Run-1 (2010-2012), the LHC was operating at 7 and 8 TeV center-of-mass energies. The superconducting beampipe magnets were upgraded during the long shutdown 2012-2015, helping to reach 13 TeV center-of-mass energy in Run-2 (2015-2018). Following Run-2 there is currently another shutdown (2019-2020), during which upgrades are performed in preparation for Run-3 (2021-2013).

At the end of Run-2 a total of approximately 160 fb$^{-1}$ of data was delivered by the LHC. This total integrated luminosity, denoted $L$, is related to the number of events $N$ produced for a physics process with cross section $\sigma$, according to the formula

$$N = \sigma L.$$

The number of events produced per unit time is a function of the instantaneous luminosity $L_I$ which is related to $L$ by

$$L = \int L_I dt.$$

The LHC was designed to achieve high instantaneous luminosity. The peak luminosity to date was achieved during Run-2 (2018), at $\sim 2.0 \times 10^{34}$ cm$^{-2}$s$^{-1}$. In general, given two colliding beams with $N_1$ and $N_2$ number of particles, a general formula for the instantaneous luminosity, assuming Gaussian profiles of the beams, is

$$L_I = f \frac{N_1 N_2}{4\pi \sigma_x \sigma_y},$$

where

- $f$ is the frequency at which the beams collide
- $\sigma_x$ and $\sigma_y$ are the root-mean-square horizontal and vertical beam sizes.

At such high luminosity we need to deal with so-called pileup events. They are undesired events on top of the hard scattering, and may occur in two scenarios. Either many interactions occur in each collision, in which case we have in-time pileup, or interactions that belong to different collisions are (incorrectly) recorded together, in which case we have out-of-time pileup. The proton bunches have been set to cross every 25 ns, down from the previous 50 ns during 2012 data taking period, to satisfy the design luminosity requirement. Such high frequencies increase out-of-time pileup as several ATLAS subdetectors take longer than 25 ns to integrate a particle's signal.

## 3.2. THE ATLAS DETECTOR

ATLAS [39] is a general-purpose detector located at one among several collision points at the LHC. The LHC, at 14 TeV designed centre-of-mass energy, is capable of probing not only Higgs physics but also some beyond Standard Model physics. Since the new hypothetical particles are typically expected to decay to energetic Standard Model particles, ATLAS is designed to be able to identify and measure important physics objects such as photons, electrons, muons, taus, hadronic jets, neutrinos, and other weakly interacting particles. In addition, with regard to jets, it is expected to be able to distinguish between heavy flavour jets ($b$ and $c$ quarks) and other light jets.

Figure 2 shows an overview of the ATLAS detector. It is 25 m in diameter and 44 m in length, and weights approximately 7000 tons.

In conformity with modern detector design, ATLAS is made up of a number of subsystems that surround one another in layers. Innermost is the inner detector, or the tracker. Next, in order, are the electromagnetic calorimeter, the hadronic calorimeter, and the muon chambers. These subsystems work in combination to provide detection capability in many possible physics scenarios. They are built out of components that are fast, precise, and that can stand against high radiation. Moreover, they are supplemented by an efficient trigger system.
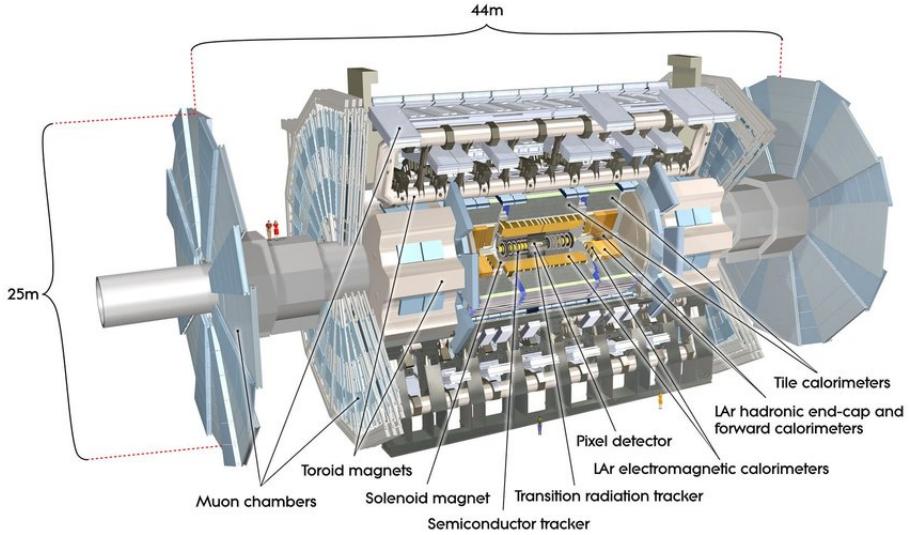


**Fig. 2.** The ATLAS Detector
[**39**]

The entire detector is nominally forward-backward symmetric with respect to the interaction point. The magnet configuration, which determines the overall design of the detector, consists of

- A thin superconducting solenoid that surrounds the inner-detector cavity,
- Three large superconducting toroids around the calorimeters, arranged with an eight-fold azimuthal symmetry.

### 3.2.1. The ATLAS Coordinate System

Each nominal interaction is given a coordinate system [**39**], where

- The origin is taken to be the interaction point;
- The $z$-axis is defined by the beam direction

Thus the $x - y$ plane is transverse to the beam direction. The positive $x$-axis points from the interaction point to the centre of the LHC ring. The positive $y$-axis points upwards.

The following quantities are used to reconstruct the kinematic Lorentz vectors of the final state particles; some of them are illustrated in Figure 3, which also illustrates the ATLAS coordinate system.

- The azimuthal angle $\phi$,
- The polar angle $\theta$,
- The rapidity

$$y = \frac{1}{2} \ln \left( \frac{E + p_z}{E - p_z} \right),$$

whose interval is invariant with respect to Lorentz boosts along the $z$-direction. This implies that the number of particles produced per unit of rapidity is approximately constant.

- The pseudorapidity

$$\eta = - \ln \left( \tan \frac{\theta}{2} \right).$$

For a particle with zero mass, $\eta$ almost coincides with $y$ but is much more convenient to measure.
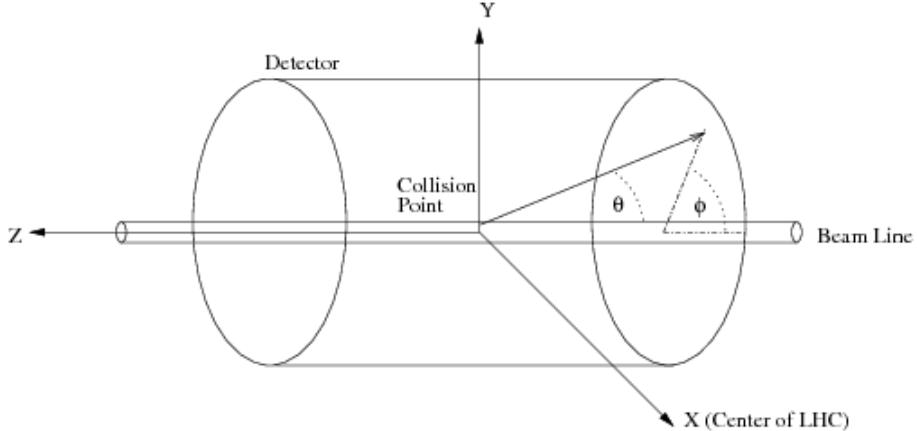


**Fig. 3.** The ATLAS Coordinate System [40]

In the transverse plane perpendicular to the beam-axis the transverse momenta and the transverse energy are defined according to the formulas

$$p_T = p \sin \theta, \qquad E_\mathrm{T} = E \sin \theta.$$

Distances in the $\eta - \phi$-plane are measured using a quantity called the angular separation

$$\Delta R = \left( \Delta \eta^2 + \Delta \phi^2 \right)^{1/2}. \tag{3.2.1}$$

### 3.2.2. The ATLAS Detector Components

3.2.2.1. The Inner Detector. The Inner Detector (ID) [**39**], also called the tracker, is built to reconstruct trajectories of charged particles from which momenta can be computed. It is capable, at high precision and high resolution, of momentum and primary vertex measurements. Moreover, it is also able to measure impact parameters and secondary vertices, and thus is capable of identifying heavy flavour jets.

Figure 4 illustrates the ID. The ID is 2.1 m in diameter and 6.2 m in length.
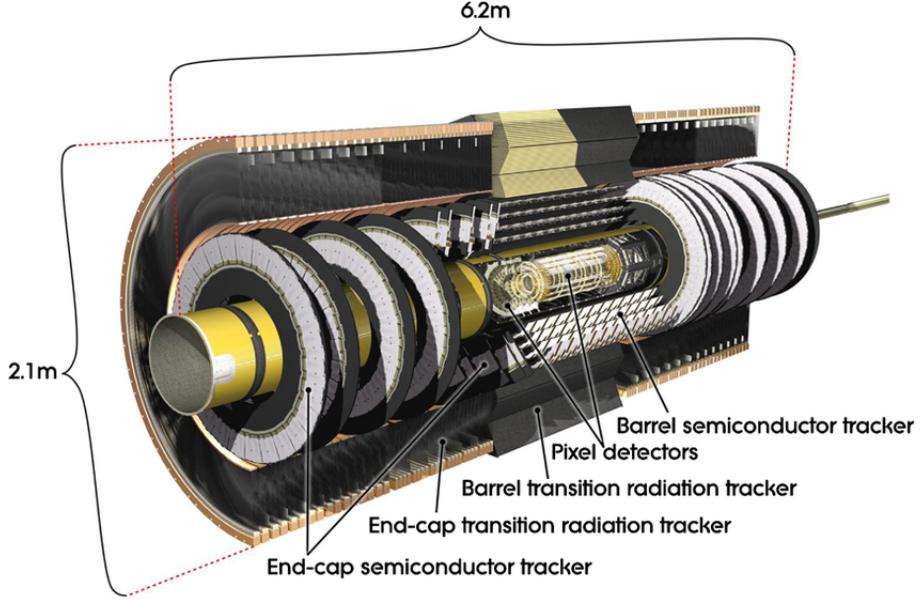


**Fig. 4.** The ATLAS Inner Detector [**39**]

The ID is surrounded by a 2T magnetic field parallel to the beam axis. This field deflects the paths of charged particles, and the path curvatures are used for the measurements of their momenta and charges.

To achieve the desired performance, the ID is built up of semiconductor pixel and strip detectors in the inner part and straw-tube tracking detectors in the outer part. The pixel and the strip detectors are silicon detectors.

The ID is divided into three main components. Thus, the Pixel Detector and the semiconductor tracker (SCT) are to work in combination with the transition radiation tracker (TRT).

The Pixel Detector and the SCT work with each other to provide precision tracking near the interaction point. They cover the region $|\eta| < 2.5$. In terms of arrangement:

- In the barrel region, they lie on concentric cylinders around the beam axis.
- In the end-cap regions, they lie on disks perpendicular to the beam axis.

The Pixel Detector. The Pixel Detector surrounds the beam pipe. Being made up of silicon pixel detectors, it is able to cope with very high track density that is typically expected.

The detector is constructed in the form of segmented layers of identical sensors in the $R - \phi$ plane and along the $z$-axis, where the sensors are of size $50 \times 400$ $\mu$m$^2$. Typically, a track is expected to cross three such layers. The achieved accuracies in the barrel are approximately 10 $\mu$m in the $R - \phi$ plane and 115 $\mu$m in the $z$ direction. The Pixel Detector has approximately 80.4 millions readout channels.

In May 2014, an additional pixel layer was installed between the pixels and the beam spot, at an average radius of 3.3 cm from the beam pipe. It is called the insertable B-layer (the IBL [**41**]) and provides an additional 8 millions pixels. The results are improvements in track reconstruction, vertex measurement, and $b$-jet identification.

SCT. A track is typically expected to cross eight strip layers of the SCT. In the barrel region, the $R - \phi$ coordinates are measured by small-angle stereo strips that lie along the beam direction, and which are distributed one set per layer. In the end-cap regions there are two sets of strips, one running radially and one at a small angle. The accuracies achieved in the barrel are 17 $\mu$m in the $R - \phi$ plane and 580 $\mu$m in the $z$ direction, and so are those in the disks in the $R$ direction. The SCT has approximately 6.3 millions readout channels in total.

TRT. The TRT measures only $R - \phi$ coordinates and covers the region $|\eta| < 2.0$. It consists of straw tubes, 4mm in diameter, that typically register 36 hits per track. Each straw tube achieves an accuracy of 130 $\mu$m. In terms of arrangement:

- In the barrel region, the straw tubes are manufactured at length 144 cm and lie parallel to the beam axis.
- In the end-cap regions, they are manufactured at length 37 cm and lie radically, in wheels.

The TRT is installed at a larger radius, and has approximately 351000 readout channels. High precision momentum measurement is achieved with a large number of measurements and longer track lengths. In addition, the TRT provides electron identification capability through the detection of transition radiation X-ray photons.

The resulting resolution is $\sigma_{p_T}/p_T = 0.05\%$ $p_T \oplus 1\%$.

The ID system supplements the calorimeters and the muon detector, which will be discussed below.

3.2.2.2. The Calorimeters. Calorimeters are built to measure energies of particles, using the fact that most particles (except muons and weakly interacting particles such as neutrinos)

that reach the calorimeters will interact with their high density material and produce a shower of particles. Calorimeters are designed to be able to contain these showers and measure the particles' positions and deposited energies.

The ATLAS calorimeters [**39**] consist of two systems, the Electromagnetic Calorimeter and the Hadronic Calorimeter, designed to measure the energies of electrons/photons and hadrons respectively. An outline of the calorimeter system is shown in Figure 5. The required resolutions are

- The Electromagnetic Calorimeter: $\sigma_E/E = 10\%/\sqrt{E} \oplus 0.7\%$,
- The Hadronic Calorimeter: $\sigma_E/E = 50\%/\sqrt{E} \oplus 3\%$ (barrel and end-cap regions), $\sigma_E/E = 100\%/\sqrt{E} \oplus 10\%$ (forward region),

where each resolution is a quadratic combination of two separation terms, one — the stochastic term — that takes into acount the statistical nature of the shower shape, and one constant term that includes the effects of detector instabilities and mis-calibration. The effect of the stochastic term decreases with growing energy.
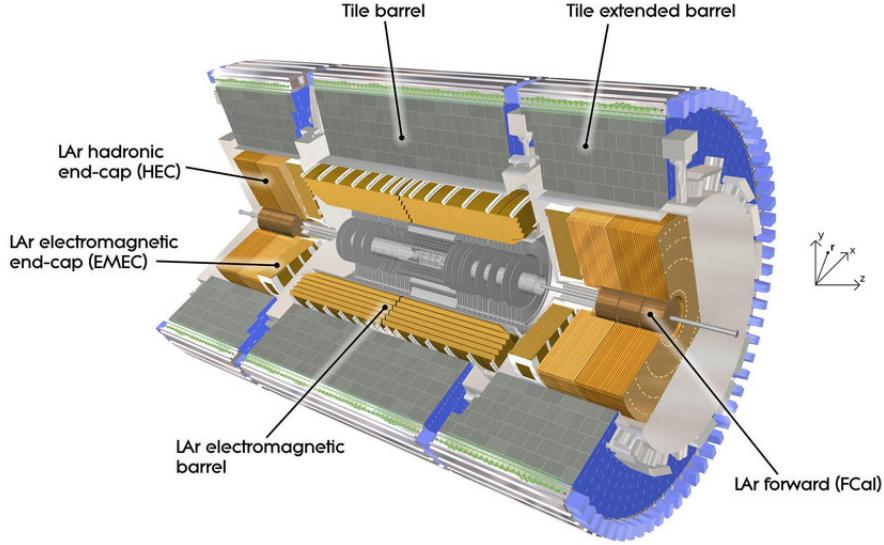


**Fig. 5.** The ATLAS Calorimeter System
[**39**]

The Electromagnetic Calorimeter. The Electromagnetic Calorimeter provides electron and photon identification and kinematic measurements. These particles lose their energies mainly through bremsstrahlung, pair production, and ionization, where the first two dominate for high-energy particles, leading to the development of shower shapes in the calorimeter.

By design, the Electromagnetic Calorimeter is a lead-LAr (Liquid Argon) detector. The lead, in the form of lead plates having an accordion shape to achieve a low capacitance of

the detecting elements and thereby a fast signal, functions as an absorber, and the liquid argon is used in the active layers.

There are:

- The barrel part, covering the region $|\eta| < 1.475$, which is $> 22$ radiation lengths in thickness.
- Two end-cap components, covering the region $1.375 < |\eta| < 3.2$, where each is $> 24$ radiation lengths in thickness.

The barrel is made up of two identical half-barrels, with a gap of 4 mm in between at $z = 0$. On the other hand, each end-cap is made up of an outer wheel that covers the region $1.375 < |\eta| < 2.5$ and an inner wheel that covers the remaining region.

There is a presampler detector, which is an active LAr layer of 1.1 cm in thickness in the barrel and 0.5 cm in thickness in each end-cap, covering the region $|\eta| < 1.8$. It is used to correct the energy lost by electrons and photons in the materials they traverse before they reach the calorimeter, such as those in the inner detector.

The Electromagnetic Calorimeter is complemented by the Hadronic Calorimeter, discussed below. Together, they contain electromagnetic and hadronic showers and limit penetration into the muon system.

The Hadronic Calorimeter. The Hadronic Calorimeter surrounds the Electromagnetic Calorimeter. It is built to measure the energy of hadronic particles, which show up in the form of showers in the calorimeter.

In terms of thickness, the Hadronic Calorimeter is approximately 10 interaction lengths in the barrel region as well as in the end-cap regions. It is divided into three parts:

- Tile calorimeter: A sampling calorimeter, where steel is used as the absorber and scintillating tiles as the active material. It is placed directly outside the EM calorimeter envelope. It has a barrel that covers the region $|\eta| < 1.0$ and two extended barrels which cover the region $0.8 < |\eta| < 1.7$, each made up of three layers.
- LAr hadronic end-cap calorimeter: The Hadronic End-cap Calorimeter covers the pseudorapidity range $1.4 < |\eta| < 3.2$. It is also a sampling calorimeter, where copper in the form of plates functions as the absorber and LAr gaps as the active medium. It has two independent wheels per end-cap. The wheels are put directly behind the end-cap electromagnetic calorimeters. Those closest to the interaction points use 25 mm parallel copper plates, and the rest uses 50 mm copper plates. The copper plates extend a radius from approximately 0.4 m to approximately 2 m, and in between are gaps of LAr materials.

- LAr forward calorimeter: The Forward Calorimeter extends the coverage up to $|\eta| = 5$, and is approximately 10 interaction lengths in depth. It has three modules in each end-cap, with one (copper) optimized for electromagnetic measurements and the remaining two (tungsten) hadronic measurements. Each module is a metal matrix of longitudinal channels, where the channels are filled with electrode structure which are in turns made up of concentric rods and tubes parallel to the beam axis, with LAr between them.

3.2.2.3. The Muon Spectrometer. Muons, being more massive than electrons (approximately 200 times), are subject to reduced bremsstrahlung as compared to electrons, and are able to pass through the ATLAS calorimeters with minimal interactions. The Muon Spectrometer [**39**] provides muon identification as well as muon momentum and charge measurement. It is capable of identifying muon candidates with $p_T$ from 3 GeV and has a design resolution of 10% for muons with $p_T = 1$ TeV.

The Muon Spectrometer surrounds the hadronic calorimeter and defines the overall dimensions of the ATLAS detector (Figure 6). It is made up of three layers of precision tracking chambers plus trigger chambers.

Deflection of the muon tracks is effected by the built-in superconducting magnets, which is a system of three large air-core toroids. In detail:

- The barrel toroid provides deflection over the range $|\eta| < 1.4$.
- The end-cap magnets at both ends of the barrel toroid, over the range $1.6 < |\eta| < 2.7$.
- A combination of the barrel and end-cap magnetic fields are used over the range $1.4 < |\eta| < 1.6$ (also called the transition region).

Muon tracks are measured in the tracking chambers. They are the Monitored Drift Tubes over most of the $|\eta|$-range, and Cathode Strip Chambers at large $|\eta|$-range. The chambers are arranged in the following manner:

- Around the beam axis, in the form of three cylindrical layers.
- In the transition ($1.4 < |\eta| < 1.6$) and end-cap regions, in three planes perpendicular to the beam.
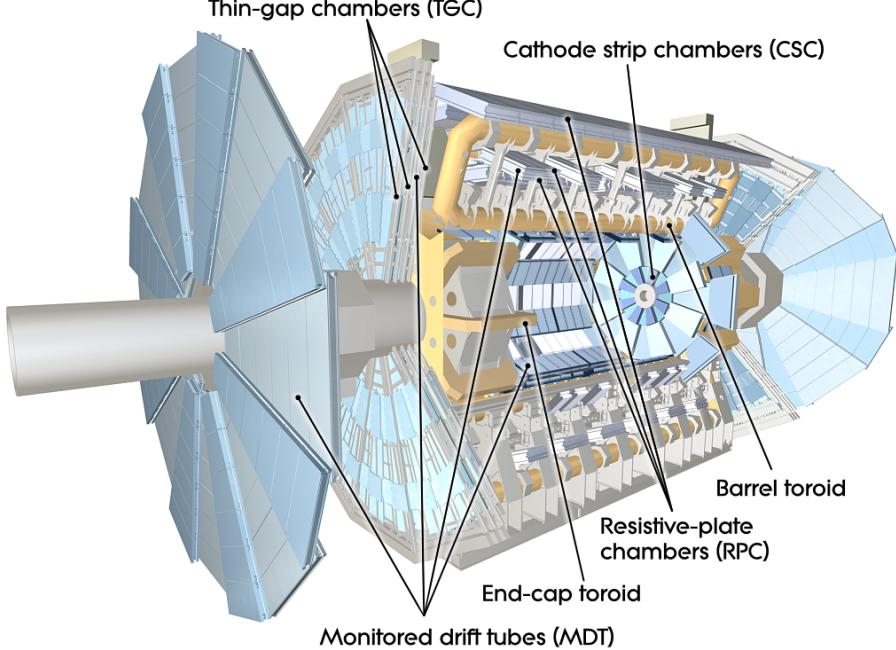
**Fig. 6.** The ATLAS Muon Spectrometer [**39**]

The trigger system works in the range $|\eta| < 2.4$. The trigger chambers, which are Resistive Plate Chambers in the barrel and Thin Gap Chambers in the end-cap regions, provide the following functionalities:

- Bunch-crossing identification.
- Well-defined transverse momentum thresholds.
- Measurements muon coordinate in the direction orthogonal to that determined by the precision-tracking chambers.

### 3.2.3. The ATLAS Trigger System

Due to the high luminosity of the LHC, the ATLAS detector, with limited storage capacity and technology, is only able to record potentially interesting physics events. This is achieved in Run-2 with a trigger system made up of two levels, the hardware level L1 and the High Level Trigger (HLT) software trigger, which together reduce the event rate from approximately 40 MHz to approximately 1 kHz [**42**].

L1 reduces the rate to about 100 kHz, taking 2.5 $\mu$s to decide for each event. It identifies high transverse-momentum muons, electrons, photons, jets, and/or taus that decay into hadrons. It also searches for events with large missing or total transverse energy. L1 is implemented using custom-made electronics, and uses low-resolution information from the calorimeters and the muon spectrometer. For each event that passes L1, one or more regions

of interests — for examples the $\eta$ and $\phi$ coordinates where something potentially useful has been seen — are defined, before the event is passed to the HLT.

On the other hand, the HLT is a software-based trigger. It reduces the event rate to about 1 kHz, using information either in the regions of interests defined by L1 or the whole event. At the HLT each event takes on average about 200 ms to process.

# Chapter 4

# ELECTRON RECONSTRUCTION AND IDENTIFICATION AT ATLAS

The central theme of this thesis is the improvement of the reconstruction and identification of signal electrons in SUSY searches. In particular, Chapter 5 deals with the estimation of electron charge mis-identification, Chapter 6 discusses a supersymmetry search that involves leptons (electrons or muons) in the final state where work on improving the selection of leptons will be presented, and Chapter 7 presents a measurement of the identification efficiencies for in-jet electrons[1]. This chapter introduces electron reconstruction and identification at ATLAS [**43**].

In ATLAS, a signal (prompt) electron refers to an electron that originates from the prompt decays of particles such as $W$, $Z$, Higgs bosons, and other potential beyond the Standard Model particles. It is expected to leave a track in the inner detector and deposits its energy in the electromagnetic calorimeter. But non-prompt electrons from heavy-flavor decays, charged hadrons, taus, and high energy muons[2] can imitate the electron signature, and distinguishing these from signal electrons is a major activity at ATLAS.

A signal electron that has been selected passes through two major steps, reconstruction and identification. Electron reconstruction, discussed in Section 4.1, is the selection, using information from the inner detector and the electromagnetic calorimeter, of a set of objects which are called electron candidates. Electron identification, on the other hand, applies criteria on tracking and calorimeter variables to select signal electrons; it is discussed in Section 4.2.

Figure 1 [**43**] shows the hypothetical path of an electron, in the red trajectory, through the ATLAS detector. The electron emerges near the collision point, passes the tracking system (made up of the pixel detectors, the silicon-strip detectors, and the TRT) before

---

[1]These refer to electrons that are found within $\Delta R = 0.4$ of high $p_T$ jets.
[2]In this case, bremsstrahlung may produce photons. The muon leaves a track in the inner detector, and the photons leave energy deposits in the calorimeter.

entering the electromagnetic calorimeter. Also shown in the figure is the path of a photon, in dashed trajectory, produced by the interaction of the electron with the material in the tracking system.
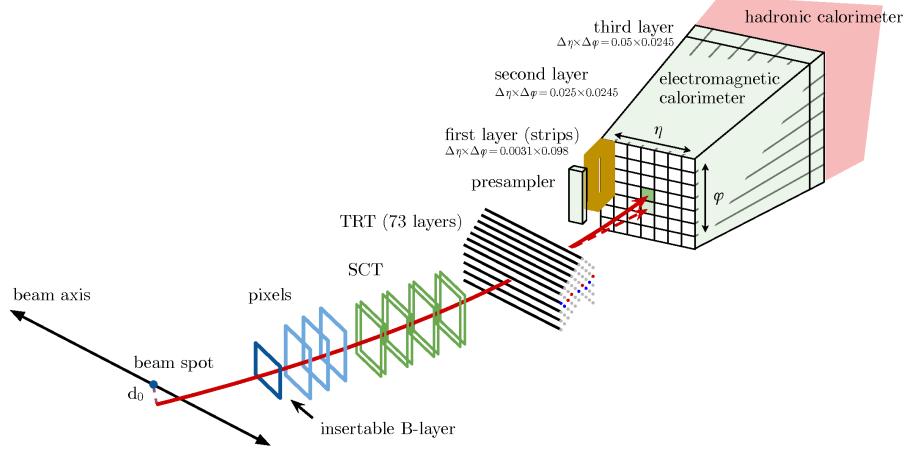


**Fig. 1.** The hypothetical path of an electron through the detector [**43**] is shown in red in the figure. The electron moves through the tracking system (pixel detectors, silicon-strip detectors, and the TRT) before entering the electromagnetic calorimeter. The dashed red line shows the path of a photon that comes from the interaction of the electron with the material in the tracking system.

## 4.1. Electron Reconstruction

Electron reconstruction at ATLAS consists of three fundamental components that characterize the signature of electrons:

- Localized clusters of energy deposits in the electromagnetic calorimeter;
- Tracks in the inner detector;
- Matching of tracks to the clusters.

These components will be discussed in some detail in the following. As this thesis is based on 2015-2016 data (analyzed by release 20 of the ATLAS software), the discussion focuses on the methods used prior to the introduction of a new electron and photon reconstruction method, dynamic and topological cell clustering-based [**44**] (which will be in release 21 of the ATLAS software).

### 4.1.1. Seed-cluster reconstruction

Electromagnetic energy cluster candidates are reconstructed from localized energy deposits in the electromagnetic calorimeter (Section 3.2.2.2) using an algorithm known as the sliding-window algorithm [**45**]. To this end, the $\eta \times \phi$ plane of the electromagnetic calorimeter

is divided into a grid of $200\times256$ elements, also called towers, of size $\Delta\eta\times\Delta\phi = 0.025\times0.025$. The algorithm starts from localized energy deposits of size $3 \times 5$ towers in $\eta \times \phi$ where the total transverse energy exceeds 2.5 GeV, moving in steps of 0.025 in either the $\eta$ or the $\phi$ direction and amassing neighboring localized energy deposits. These accumulated clusters of energy deposits are referred to as seed-cluster candidates. In the case where two candidates overlap within an area of $\Delta\eta \times \Delta\phi = 5 \times 9$ units of $0.025 \times 0.025$, both will undergo a selection process in which

- Only the one that has transverse energy at least 10% higher than the other is kept; or otherwise
- Only the one that contains the highest transverse momentum in the central tower is kept.

The reconstruction efficiency of this seed-cluster algorithm is found to depend on $\eta$ and on the transverse energy. Figure 2 shows the dependency on $E_T$. The efficiency ranges from 96% at $E_T = 7$ GeV to more than 99% above $E_T = 15$ GeV.

## 4.1.2. Track reconstruction

The interactions of charged particles with the inner detector material create hits [46] in the latter. In track reconstruction, these hits are assembled into clusters in the pixel and SCT detectors, from which three-dimensional measurements called space-points are built. In the silicon-detector layers, sets of three space-points are used to form track seeds. Then a pattern-recognition algorithm proceeds to build track candidates, in which energy loss of a particle due to its interactions with the detector material is modelled assuming the particle is a pion. A modified pattern-recognition will be used in the case where a track seed having $p_T > 1$ GeV cannot be extended to a full track of at least seven hits per track candidate and the associated electromagnetic calorimeter cluster satisfies shower width and depth requirements. The modified algorithm allows up to 30% energy loss for bremsstrahlung at each intersection of the track with the detector material.

Track candidates with $p_T > 400$ MeV are fit using the ATLAS Global $\chi^2$ Track Fitter [47], taking into account which pattern-recognition algorithm was used. Ambiguities arising from track candidates sharing hits are also resolved in this step. Figure 2 shows that the track reconstruction efficiency reaches more than 98% above $E_T = 10$ GeV.

An additional fit, using the Gaussian-sum filter (GSF) [48] method to better model energy loss of the particle, is applied on tracks having at least four silicon hits and that are loosely matched to electromagnetic clusters. The method takes into account non-linear effects related to bremsstrahlung and models experimental noise by a sum of Gaussian functions.
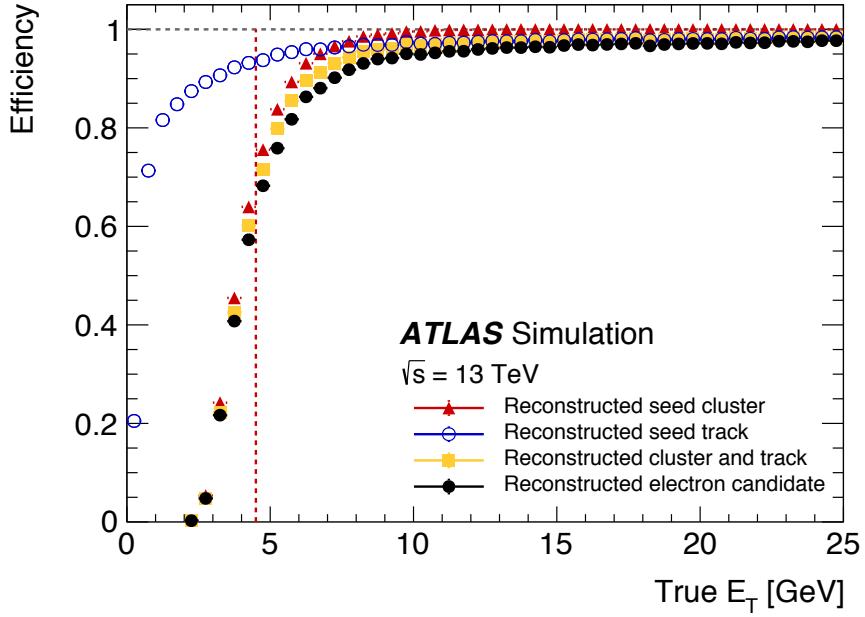
**Fig. 2.** The efficiencies for simulated electrons in a single-electron sample as a function of the true generator $E_T$ for each step in the reconstruction process, as well as the total efficiency: $\Delta\eta \times \Delta\phi = 3 \times 5$ seed-cluster reconstruction (red triangles), seed-track reconstruction using the Global $\chi^2$ Track Fitter (blue open circles), both steps but using GST tracking (yellow squares), and the final reconstructed electron candidate (black closed circles) [**43**].

### 4.1.3. Electron-candidate reconstruction

In this final step, the GSF-track candidate is matched to the candidate calorimeter seed cluster and the final cluster size is determined. If during the matching procedure several tracks may be matched to a same cluster, an algorithm using such information as the number of hits in the silicon detectors, the number of hits in the innermost silicon layer, and others, is applied to select out the primary track. The resulting object is called an electron candidate if it has an associated track with at least four hits in the silicon layers and no association with a vertex from photon conversion. If on the other hand its primary track can be matched to a secondary vertex and has no pixel hits, the object is classified as a photon candidate instead.

Subsequently the candidate electron undergoes an additional classification — mainly to keep a high photon reconstruction efficiency — to determine if it still should be considered as a potential photon candidate. The classification uses the candidate electron's $E/p$ and $p_T$, the presence of a pixel hit, and the secondary-vertex information.

The energy of the final electron candidate is computed from the calibrated energy of the extended-window cluster, which is formed from the original seed cluster by expanding the size of the latter of $\phi$ or $\eta$. The calibration uses multivariate techniques [**49, 50**].

Figures 2 and 3 show the total reconstruction efficiency as a function of $E_T$ and as a function of $\eta$ in bins of $E_T$, respectively, for single-electron and $Z \to e^+e^-$ events, respectively. This efficiency is defined as the ratio of the number of reconstructed electron candidates and the number of electromagnetic-cluster candidates. For $E_T > 15$ GeV, the reconstruction efficiency varies from approximately 97% to 99%. In Figure 3, the data efficiency is measured in $Z \to e^+e^-$ events using the tag and probe method [43], and it can be seen that simulation efficiency is lower than data efficiency (within three percents) in the low $E_T$ region ($E_T < 30$ GeV) but is higher (up to a few percents) in the higher $E_T$ region ($E_T > 30$ GeV).
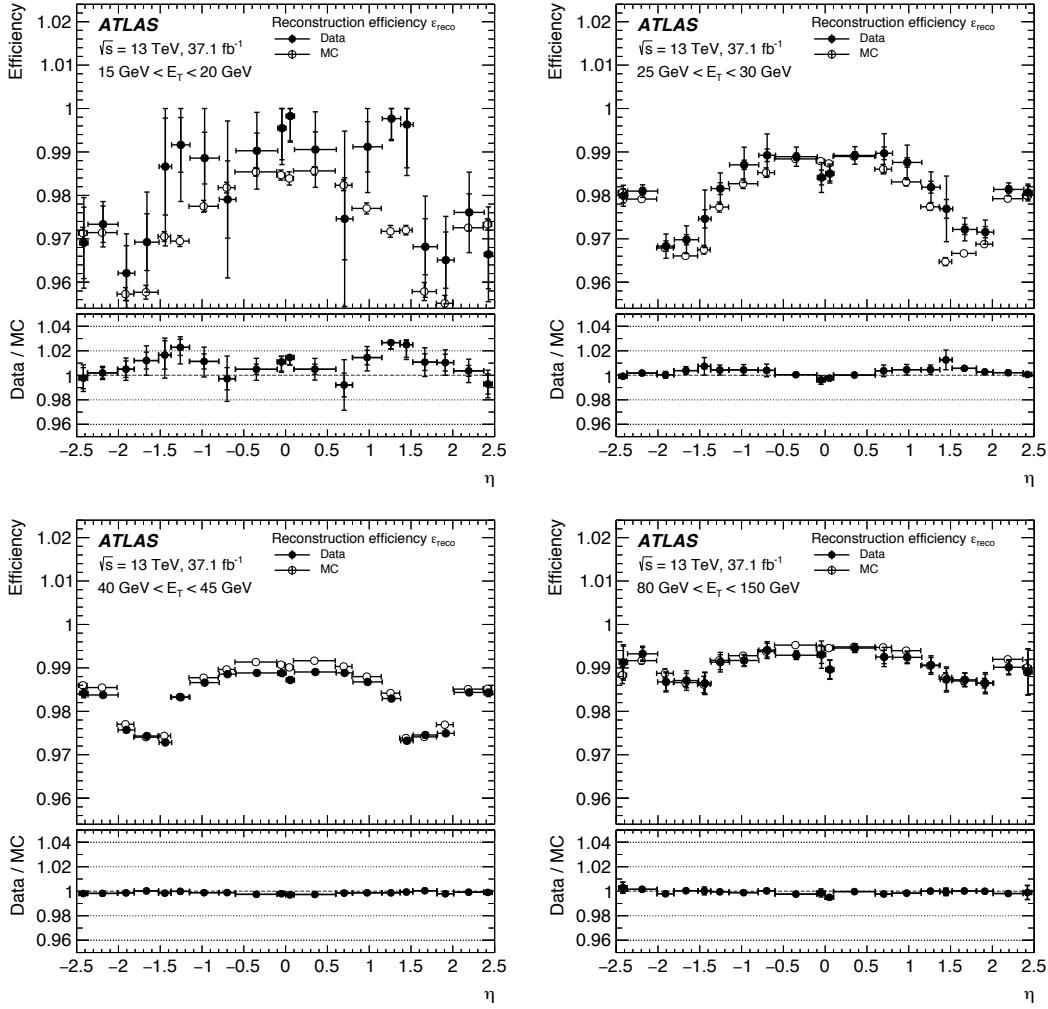


**Fig. 3.** The total reconstruction efficiencies, defined as the ratio of the number of reconstructed electron candidates and the number of electromagnetic-cluster candidates, evalued in the 2015-2016 dataset (closed points) and in simulation (open points) and the ratios between the two in $Z \to ee$ events. The efficiencies are shown as a function of $\eta$ in four $E_T$ bins: 15-20 GeV (top left), 25-30 GeV (top right), 40-45 GeV (bottom left), and 80-150 GeV (bottom right) [43].

## 4.2. Electron Identification

Electron candidates emerging from reconstruction consist mostly of background electrons that are made up of hadrons, electrons from photon conversions, and electrons from heavy-flavor decays. Electron identification is the step whereby these background electrons are reduced.

### 4.2.1. Likelihood Identification

Prompt electrons that enter the central region ($|\eta| < 2.47$) are selected using a method called the likelihood identification. Non-prompt and fake electrons are expected to suffer track conditions, deviate from the ratio $E/p \sim 1$, and have a wider and deeper shower shape, and in the likelihood method, these differences between them and prompt electrons are analyzed in detail. The method uses seven types of variables, namely hadronic leakage, third layer of the EM calorimeter, second layer of the EM calorimeter, first layer of the EM calorimeter, track conditions, TRT, and track-cluster matching [43]. Hadronic leakage, for instance, includes quantities that exploit the fact that hadrons reconstructed as electron candidates will reach the hadronic calorimeter, while real electrons are expected to be absorbed entirely in the electromagnetic calorimeter.

- Hadronic leakage.
  - $R_{\mathrm{had1}}$: Ratio of the transverse momentum in the first layer of the Hadronic Calorimeter to that of the Electromagnetic Calorimeter.
  - $R_{\mathrm{had}}$: Ratio of the transverse momentum in the Hadronic Calorimeter to that of the Electromagnetic Calorimeter cluster (used in range $0.8 < |\eta| < 1.37$).
- Third layer of EM calorimeter
  - $f_3$: Ratio of the energy in the third layer to the total energy in the Electromagnetic Calorimeter (used only for $E_T < 80$ GeV).
- Second layer of EM calorimeter
  - $\omega_{\eta^2}$: Lateral shower width.
  - $R_\phi$: Ratio of the energy in $3 \times 3$ cells over the energy in $3 \times 7$ cells centered at the electron cluster position.
  - $R_\eta$: Ratio of the energy in $3 \times 7$ cells over the energy in $7 \times 7$ cells centered at the electron cluster position.
- First layer of EM calorimeter
  - $\omega_{\mathrm{stot}}$: Shower width.
  - $E_{\mathrm{ratio}}$: Ratio of the energy difference between the maximum energy deposit and the energy deposit in a secondary maximum in the cluster to the sum of these energies.

- $f_1$: Ratio of the energy in the first layer to the total energy in the EM calorimeter.
- Track conditions
  - $n_{\text{Blayer}}$: The number of hits in the innermost pixel layer.
  - $n_{\text{Pixel}}$: The number of hits in the Pixel detector.
  - $n_{\text{Si}}$: The total number of hits in the pixel and SCT detectors.
  - $d_0$: Transverse impact parameter relative to the beam-line.
  - $|d_0/\sigma(d_0)|$: Significance of transverse impact parameter defined as the ratio of $d_0$ to its uncertainty.
  - $\Delta p/p$: Momentum lost by the track between the perigee and the last measurement point divided by the momentum at perigee.
- TRT
  - eProbabilityHT: Likelihood probability based on transition radition in the TRT.
- Track-cluster matching
  - $\Delta\eta_1$: $\Delta\eta$ between the cluster position in the first layer and the extrapolated track
  - $\Delta\phi_{\text{res}}$: $\Delta\phi$ between the cluster position in the second layer of the EM calorimeter and the momentum-rescaled track, extrapolated from the perigee, times the charge $q$
  - $E/p$: ratio of the cluster energy to the track momentum (for $E_T > 150$ GeV)

These are used as inputs to two likelihood functions, one for signal electrons and one for background electrons, that take the forms

$$L_S(\mathbf{x}) = \prod_{i=1}^{n} P_{S,i}(x_i), \qquad L_B(\mathbf{x}) = \prod_{i=1}^{n} P_{B,i}(x_i),$$

respectively. Here $\mathbf{x}$ is a vector of entries $x_i$ which are the inputs that correspond to the quantities listed above, each of which has a signal probability distribution function (pdf) and a background pdf. The correlations between the input variables $\mathbf{x}$ are neglected in this method. $P_{S,i}(x_i)$ is the value of the signal pdf of the quantity $i$ at the value $x_i$, and likewise $P_{B,i}(x_i)$ is the value of the background pdf. The pdfs are derived using simulation samples, with corrections applied when discrepancies with the corresponding data are found. The correlations between the inputs are neglected.

Then, from each electron candidate discriminant value $d_L$ is computed according to the formula

$$d_L = \frac{L_S}{L_S + L_B}.$$

This discriminant is actually transformed into

$$d'_L = -\tau^{-1}\ln(d_L^{-1} - 1), \tag{4.2.1}$$

which then serves as a quantity to assess if an electron candidate should be considered a prompt electron. The parameter $\tau$ is set to 15 [**51**]. Figure 4 shows the transformed discriminant $d'_L$ for prompt electrons from $Z$-boson decays and for background, illustrating the effective separation between the two.

## 4.2.2. Operating Points

Background rejection and identification efficiency are inversely related i.e. the higher is one, the lower is the other, and vice versa. In order to cover various signal efficiencies and background rejection factors as needed by physics analyses, ATLAS has defined four so-called identification operating points. They are, in order of increasing background rejection power, VeryLoose, Loose, Medium, and Tight. All operating points have fixed requirements on tracking criteria:

- Loose, Medium, and Tight: at least two hits in the Pixel detector and a total of seven hits in the pixel and silicon strip detectors combined. To reduce background from photon conversions, Medium and Tight require one of these pixel hits to be in the innermost pixel layer or, if this layer is out of order, the layer immediately after it. There is a variation of the Loose operating point, called LooseAndBLayer, that is the same as Loose except with the addition of the requirement of a hit in the innermost layer also.

- VeryLoose: one hit in the pixel detector, regardless of the layer.

A particular value of $d'_L$ (Equation 4.2.1) is defined for each of them, and in the context of an operating point, electron candidates with computed $d'_L$ larger than the defined value are considered prompt electrons. In the likelihood method, candidates that pass an operating point having a higher background rejection power also pass the operating points having lower background rejection powers.
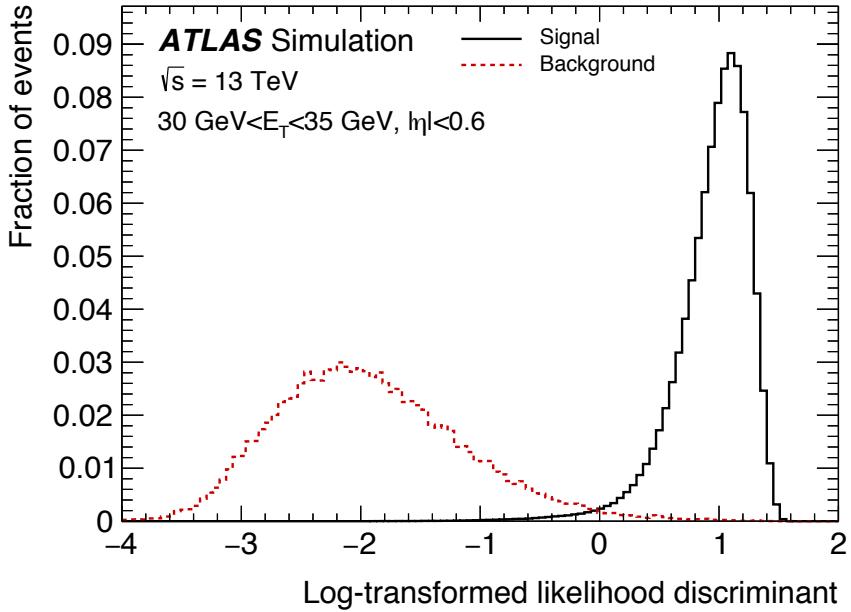
**Fig. 4.** The discriminant $d'$ (Formula 4.2.1) for reconstructed electron candidates with good quality tracks with $30$ GeV $< E_T < 35$ GeV. The black distribution shows prompt electrons in a $Z \to ee$ simulation sample, and the red distribution shows background electrons in a generic two-to-two process simulation sample [**43**].

Figure 5 shows the efficiencies measured in $J/\psi \to ee$ and $Z \to ee$ events for data and the corresponding data-to-simulation ratios. Specifically, the variations of the efficiencies in $E_T$ and $\eta$ for the Loose, Medium, and Tight operating points are displayed. The efficiency ranges from 55% at $E_T = 4.5$ GeV to 90% at $E_T = 100$ GeV for the Tight point, and from 85% at $E_T = 20$ GeV to 96% at $E_T = 100$ GeV for the Loose point. On the other hand, the efficiency decreases as we move to higher $|\eta|$, the decreases could be as large as 10%.

The lower efficiencies of the Medium and Tight operating points result in an increased rejection of misidentified electrons. In the $E_T$ range of $4 - 50$ GeV, the rejection factors for misidentified electrons from multijet production increase by factors of $\sim 2.5$ for the Medium point and $\sim 5$ for the Tight point compared to the Loose point [**43**].
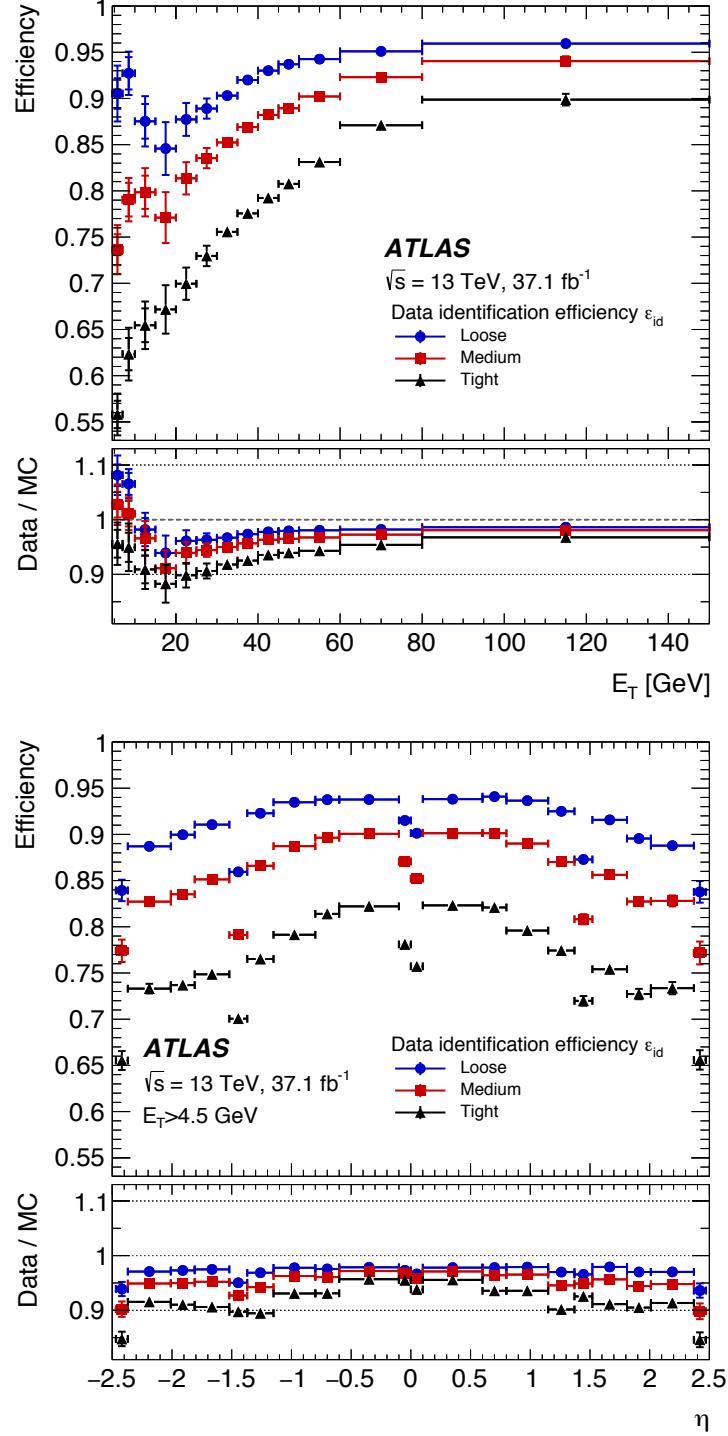
**Fig. 5.** The likelihood identification efficiencies as functions of $E_T$ and $\eta$ in $Z \rightarrow ee$ events for Loose, Medium, and Tight (shown in blue, red, and black respectively). The data efficiencies are obtained by applying data-to-simulation efficiency ratios measured in $J/\psi \rightarrow ee$ and $Z \rightarrow ee$ events to $Z \rightarrow ee$ simulation [43].

# Chapter 5

---

# ESTIMATING THE RATES OF ELECTRON CHARGE MIS-IDENTIFICATION

Many physics analyses involve charged leptons in their final states, where leptons typically refer to electrons or muons. Not only are the kinematic quantities associated with these particles measured, their charges have to be determined as well, using the curvatures of the tracks which result from the inner detector magnetic field. As will be discussed below, the measured charges are not always correct, causing what is called charge mis-identification.

Estimating charge mis-identification is important for analyses that involve same-sign leptons [1] in the final state, such as measurements of the same-sign $WW$ scattering [**53**], Higgs production in association with a $t\bar{t}$ pair ($t\bar{t}H$) [**54**], or SUSY search with two same-sign leptons [**55**]. In general, electron charge mis-identification rates occur on the order of O(1%), whereas Standard Model processes that provide opposite-sign dileptons, dominantly $Z \rightarrow e^+e^-$, occur approximately $10^3$ times more commonly than genuine Standard Model sources of same-sign leptons (dominantly $WZ$ production). Accordingly, opposite-sign sources of dileptons that suffer from charge mis-identification can constitute a significant background in these searches, and must therefore be estimated as precisely as possible.

This chapter describes a method for estimating the rate of charge mis-identification using a likelihood function. Section 5.1 discusses briefly how electron charge mis-identification might arise in ATLAS. Section 5.2 discusses the likelihood method, including the Poisson likelihood used as well as how it is applied to $Z \rightarrow e^+e^-$ events to measure the charge mis-identification rates. Finally, Section 5.3 provides some conclusions.

---

[1]For all practical purposes, muon charge mis-identification is negligible in ATLAS [**52**]. Compared to electrons, muons are much less likely to undergo bremsstrahlung and pair-production in the detector. Moreover, muon tracks are measured in the inner detector as well as in the muon spectrometer, prodiving a larger lever arm for curvature measurements.

The data used was collected with the ATLAS detector in 2012, at 8 TeV center-of-mass energy and corresponds to an integrated luminosity of 20.3 fb$^{-1}$.

## 5.1. Electron Charge Mis-identification

In ATLAS, the sign of the charge of an electron is determined from the sign of the curvature of its track in the inner detector (Section 3.2.2.1). Charge mis-identification occurs mainly because of two reasons:

- The electron may radiate photons as it passes through the detector and interacts with the detector materials. These radiated photons may in turn convert to electron-positron pairs. A charge mis-identification occurs when the electron candidate is matched to the wrong track. This is the dominant source of charge mis-identification.
- The reconstructed track associated with the electron has a small curvature, which may happen due to very high momentum or large pseudorapidity, the latter case because of the limit of the lever arm of the tracker. Indeed, for $|\eta| \geq 2.0$, the track is oriented in the endcap region of the ATLAS detector and will not reach the full available lever arm of $\sim 1.2$ m transverse to the beam of the inner detector.

## 5.2. The Likelihood Method

We assume that there is a probability associated to charge mis-identification and seek to determine this rate in a sample of electrons. In ATLAS, $Z \to e^+e^-$ events are used for this purpose because they are a dominant source of opposite-sign electrons as compared to other Standard Model sources. A very clean and high-statistics sample of electrons may be obtained by selecting two isolated electrons around the invariant $Z$ mass peak. Due to charge mis-identification, not only are opposite-sign pair of electrons observed, same-sign pairs will be encountered as well, from which the charge mis-identification rates could be determined. More specifically, the mis-identification rates to be extracted are parameters of a Poisson likelihood function that will be discussed below.

The rates obtained will be applied to an opposite-sign control sample in data, or to correct the MC simulation, to estimate the electron charge mis-identification background in a same-sign lepton analysis.

### 5.2.1. The $Z \to e^+e^-$ Sample

In ATLAS, electron charge mis-identification rates are extracted from $Z \to e^+e^-$ events using a likelihood function (Section 5.2.2). These events are required to undergo the following preliminary selections. Further selections that will be applied before the rates are extracted are discussed in Section 5.2.3.

Preliminary event selections.

- A logical OR between two single-electron triggers, one with $E_T > 24$ GeV plus Medium identification, and one with $E_T > 60$ GeV plus Loose identification.
- At least two reconstructed electron candidates with $|\eta| < 2.47$. The invariant mass of the electron pair must be within $\pm 15$ GeV of the $Z$ mass.

Figure 1 [43] shows the invariant mass distribution $m_{ee}$ in data and simulation for $E_T$ between 25 GeV and 50 GeV and $0.0 < \eta < 0.8$ (left) or $2.0 < \eta < 2.47$ (right). Due to charge mis-identification, same-sign electron pairs also exist in addition to opposite-sign pairs, indicating a charge mis-identification rate of $\sim 10^{-3}$ in the central region and $\sim 10\%$ in the high $\eta$ region. The higher rates in the latter is expected because of the larger amount of material and the limited lever arm in the forward region. In both cases, same-sign pairs show a broader peak that is also shifted slightly towards lower values, consistent with the fact that the radiation that causes charge mis-identification also results in energy loss.
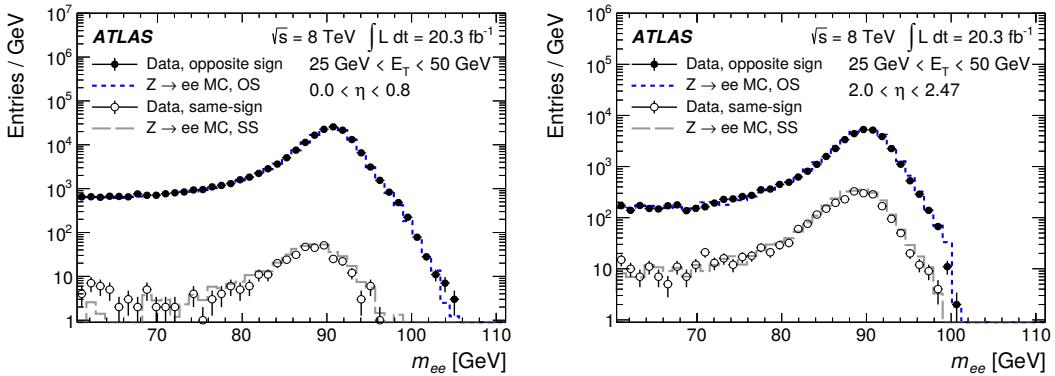


**Fig. 1.** Distribution of the invariant mass $m_{ee}$ for $E_T$ between 25 and 50 GeV and $|\eta|$ between 0.0 and 0.8 [43]. Due to charge mis-identification same-sign pairs as well as opposite-sign pairs are observed.

The next section discusses the Poisson likelihood function that is used to fit the data.

## 5.2.2. The Poisson Likelihood

In a truth-level (MC simulated) $e^+e^-$ pair, which will also be called a truth-level opposite-sign pair, if the charge of any one of the electrons is mis-identified, then a same-sign pair will be observed instead[2]. Assuming a probability $p$ that a truth-level opposite-pair will be identified as a same-sign pair, then in considering $n$ truth-level pairs $e^+e^-$, the probability that exactly $n_{ss}$ same-sign pairs will be counted follows the binomial distribution

---

[2]In order to distinguish between truth-level electron pairs and identified ones, we will always write truth-level to indicate the former. Thus if a pair is not preceded by "truth-level", it is tacitly understood to be an identified pair.

$$P(n_{ss}) = \binom{n}{n_{ss}} p^{n_{ss}} (1-p)^{n-n_{ss}}.$$

The charge mis-identification probability $p$ is typically small while the sample of $n$ pairs of electrons considered is typically very large, and therefore the Poisson distribution may be used instead. Thus, let

$$m_{ss} = np \tag{5.2.1}$$

denote the expected number of same-sign pairs, then the Poisson distribution

$$P(n_{ss}) = \frac{m_{ss}^{n_{ss}} e^{-m_{ss}}}{n_{ss}!} \tag{5.2.2}$$

gives the probability of counting $n_{ss}$ same-sign pairs, given the expected number of same-sign pairs $m_{ss}$. This will be used to obtain a likelihood function, to be maximized to extract the charge mis-identification rates, as will be explained further below.

The probability $p$ that a truth-level opposite-pair will be identified as a same-sign pair may be written directly in term of the probability of charge mis-identification associated to an individual electron. If $\epsilon$ denotes the latter probability, then because a same-sign pair will be observed precisely when only one of the electrons has its charge mis-identified, we may write

$$p = (1-\epsilon)\epsilon + \epsilon(1-\epsilon). \tag{5.2.3}$$

The Poisson probability function of Equation 5.2.2 may now be written to depend explicitly on $\epsilon$:

$$P(n_{ss}|\epsilon) = \frac{m_{ss}^{n_{ss}} e^{-m_{ss}}}{n_{ss}!}, \quad \text{where} \quad m_{ss} = np = n[(1-\epsilon)\epsilon + \epsilon(1-\epsilon)]. \tag{5.2.4}$$

This function is turned into a likelihood that is maximized with respect to the agreement with the data, which yields the most likely estimate of the mis-identification rates $\epsilon$'s.

However, because charge mis-identification rates are expected to show strong dependencies on $p_T$ and $\eta$ of the electrons (Section 5.1), they are often measured in bins of these two quantities. In such a situation the electrons in a pair generally belong to different bins and that needs to be taken into account in the likelihood function. Thus, the electrons are assigned charge mis-identification probabilities $\epsilon_i$ and $\epsilon_j$, where the indices $i$ and $j$ indicate the bins, and we write

- The probability

$$p_{ij} = (1-\epsilon_i)\epsilon_j + \epsilon_i(1-\epsilon_j) \tag{5.2.5}$$

in place of the probability $p$ in Equation 5.2.3. This is the probability an opposite-sign pair may be seen as a same-sign pair in the bin pair $(i,j)$.

- The number of electron pairs considered, $n_{ij}$, in the bin pair $(i,j)$.
- The expected number of same-sign pairs

$$m_{ss,ij} = n_{ij}p_{ij} \tag{5.2.6}$$

  in place of the expected number of same-sign pairs in Equation 5.2.1.
- The Poisson likelihood

$$P(n_{ss,ij}|\epsilon_i, \epsilon_j) = \frac{m_{ss,ij}^{n_{ss,ij}} e^{-m_{ss,ij}}}{n_{ss,ij}!}, \quad \text{where} \quad m_{ss,ij} = n_{ij}p_{ij} = n_{ij}[(1-\epsilon_i)\epsilon_j + \epsilon_i(1-\epsilon_j)], \tag{5.2.7}$$

  in place of the Poisson likelihood in Equation 5.2.4. This will also be denoted simply as $L_{ij}$.

These equations are valid whether the rates are extracted in only $p_T$ bins, only $\eta$ bins, or both, because in the latter case the grid of two-dimensional bins may be treated as a long one-dimensional sequence of bins. On the other hand, all the possible bin pairs $(i,j)$ need to be used and therefore, assuming statistically-independent rates, the rates $\epsilon_i$ to be extracted emerge from the maximization of the likelihood function

$$L = \prod_{i,j} L_{ij},$$

the data being $n_{ij}$, the numbers of electrons observed in the bin pair $(i,j)$, and $n_{ss,ij}$, the number of same-sign electron pairs observed in the bin pair $(i,j)$.

Background subtractions. Backgrounds to $Z \to e^+e^-$ events consist mostly of events involving top quarks, multijets, diboson events, and $W$+jets events. They are assumed to be flat in the invariant $Z$ mass peak selection and are subtracted by a method called the sideband method. To this end, we will denote the invariant mass interval around the $Z$ mass peak by $(m_l, m_h)$, where $m_l = 15$ GeV and $m_h = 15$ GeV are the sizes of the intervals. Then an interval of 15 GeV is selected to the left of $m_l$ and to the right of $m_h$, i.e. $m_l = m_h = 15$ GeV and there are now two side intervals $(m_l - w_l, m_l)$ and $(m_h, m_h + w_h)$ in addition to the original interval $(m_l, m_h)$. The side intervals are assumed to be dominated by background events and are used to compute the backgrounds in the $(m_l, m_h)$ interval, i.e. to subtract background contamination in $n_{ij}$ and $n_{ss,ij}$, quantities that need to be counted in the $(m_l, m_h)$ interval. We will write $b(n_{ij})$ for the background contamination in $n_{ij}$, and $b(n_{ss,ij})$ for the background contamination in $n_{ss,ij}$; they will be computed as weighted quantities:

$$b(n_{ij}) = \frac{w_l \times n_{ij}^l + w_h \times n_{ij}^h}{w_l + w_h}, \qquad b(n_{ss,ij}) = \frac{w_l \times n_{ss,ij}^l + w_h \times n_{ss,ij}^h}{w_l + w_h}.$$

The terms $n_{ij}$ and $n_{ss,ij}$ and the background terms $b(n_{ij})$ and $b(n_{ss,ij})$ are put into the Poisson likelihood (Equation 5.2.7):

$$P(n_{ss,ij}|\epsilon_i, \epsilon_j) = \frac{m_{ss,ij}^{n_{ss,ij}} e^{-m_{ss,ij}}}{n_{ss,ij}!}$$

in which the background terms make a contribution to the expected number of same-sign $m_{ss,ij}$ in the likelihood, modifying it from $m_{ss,ij} = n_{ij}p_{ij}$ (Equation 5.2.6) to

$$m_{ss,ij} = (n_{ij} - b(n_{ij})) \times p_{ij} + b(n_{ss,ij}).$$

The first quantity on the right in the equation above is the same-sign contribution from signal events where the background events have to be subtracted, and the second quantity is the contribution from background events.

## 5.2.3. Charge Mis-identification Rates and Uncertainties

The rates are obtained upon the maximization of the likelihood function discussed in the previous section. The statistical uncertainties associated with the estimated rates depend on the statistics of the data, and are given by the statistical tool that maximizes the Poisson likelihood.

The following sources of systematic uncertainties are evaluated:

- The systematic uncertainty that comes from background subtraction, which is evaluated by determining the rates with and without background subtraction. The inclusion of this uncertainty ensures a conservative figure of systematic uncertainty in the charge mis-identification rates; it has a small impact because the background is small.
- The invariant mass interval $(m_l, m_h)$ may be varied, from 15 GeV around the $Z$ mass to 10 and 20 GeV additionally. This provides an estimation of the impact of the choice of mass window on the measure rates.
- The invariant mass widths $w_l$ and $w_h$ may be varied, taking values 20, 25, or 30 GeV. Thus, the uncertainty on the rates due to the choice of a mass width is taken into account.

The actual rates are estimated for the following three sets of requirements:

- Medium: Medium identification requirements.
- Tight + isolation: Tight identification requirements plus track isolation cut $p_T^{\text{cone } 0.2}/E_T < 0.14$.
- Tight + isolation + impact parameter: Tight identification plus $E_T^{\text{cone } 0.3}/E_T < 0.14$ and $p_T^{\text{cone } 0.2}/E_T < 0.07$ and additionally $|z_0| \times \sin\theta < 0.5$ mm and $|d_0|/\sigma_{d_0} < 5.0$.

Figure 2 [**43**] shows the estimated rates in data and simulation, for electron $E_T$ between 25 and 50 GeV as a function of $\eta$, the variable upon which they depend the most. The dashed lines indicate the bins in which the rates are calculated. The total uncertainty, which is computed as the sum in quadrature of statistical and systematic uncertainties, is also shown. Charge mis-identification rates vary from $\sim 10^{-3}$ in the central region to $\sim 10\%$ in high $\eta$ region, reflecting the correlation of the rates with bremsstrahlung, and thus a dependency on the amount of the material traversed. On the other hand, tighter selection criteria, in particular requirements on the isolation or track parameters, may decrease the charge misidentification probability by a factor of up to four, depending on the additional selection requirements[3]. Moreover, as is seen, simulation overestimates the rates as compared to the data by 5-20% depending on $\eta$ and electron requirements.

Charge mis-identification rates are known to show a positive correlation with $p_T$ as well (Figure 3).

---

[3]The energy in the cone around an electron could indicate the amount of energy deposited by bremsstrahlung, and large values of the track impact parameters could mean that the track matched to the electron is not a prompt track from the primary vertex but from a secondary interaction or bremsstrahlung and a subsequent conversion [**43**].
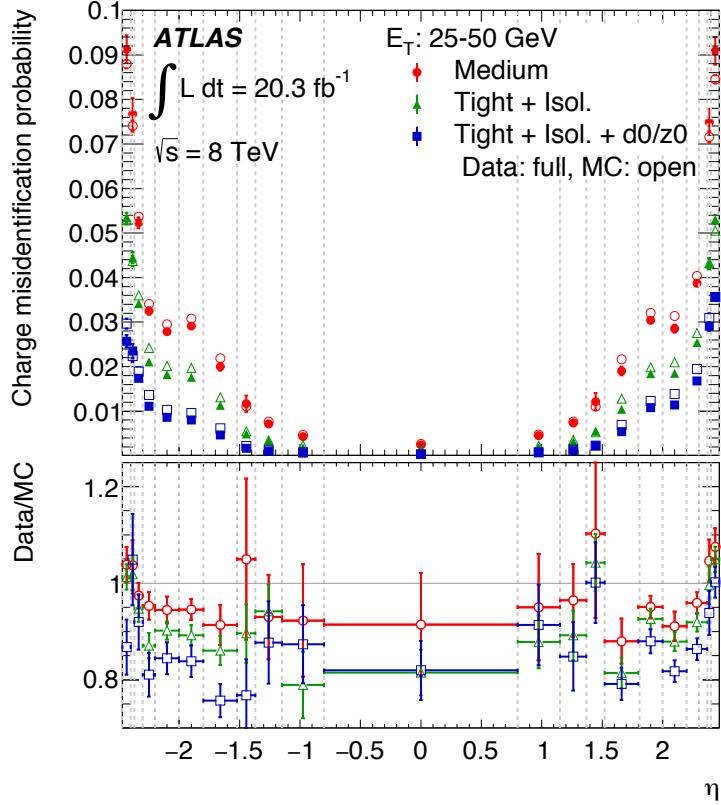
**Fig. 2.** Charge mis-identification probabilities in $\eta$ bins, $E_T$ between 25 GeV and 50 GeV [**43**]. Three different sets of selection requirements (Medium, Tight + Isolation, and Tight + Isolation + impact parameter) are shown, along with simulation expectations. Displayed in the lower panel is the data-to-simulation ratios. The uncertainties are the total uncertainties from the sum in quadrature of statistical and systematic uncertainties. The dashed lines indicate the bins in which the rates are calculated.

## 5.2.4. Estimating Charge Mis-identification Background from the Charge Mis-identification Rates

In this section we give an example of how the charge mis-identification rates may be used to estimate the charge mis-identification background in analysis with a same-sign lepton pair signature. This technique is used for example in the SUSY same-sign leptons search [**55**]. Thus, given $n_{ss,ij}$ of same-sign electron pairs that has been selected in the bin pairs $(i,j)$ (Section 5.2), we want to determine the charge mis-identification contribution to it.

To begin, the number of same-sign electron pairs $n_{ss,ij}$ that has been selected under a set of selection requirements is to be distinguished from the number of truth-level same-sign electron pairs. The latter is what would be counted in the bin pairs $(i,j)$ if there were no charge mis-identification. In the following we will denote it by $\bar{n}_{ss,ij}$.

A charge mis-identification contribution occurs whenever there is a truth-level opposite-sign pair of electrons in which one of the electron has its charge mis-identified. The probability for this to happen is, according to Equation 5.2.5,

$$p_{ij} = (1 - \epsilon_i)\epsilon_j + \epsilon_i(1 - \epsilon_j),$$

where $\epsilon_i$ and $\epsilon_j$ are the charge mis-identification rates in the bins. Now, in the same bin pair $(i,j)$ the number of opposite-sign pairs obtained from the same selection requirements may be counted as well, and we will write it as $n_{\mathrm{os,ij}}$. Moreover, as for the same-sign case, this has to be distinguished from the number of truth-level opposite-sign pairs, which will be denoted $\bar{n}_{\mathrm{os,ij}}$. The number of interest is $\bar{n}_{\mathrm{os,ij}}$, because given the mis-identification rate $p_{ij}$, the charge mis-identification contribution to $n_{\mathrm{ss,ij}}$ is simply $\bar{n}_{\mathrm{os,ij}} \times p_{ij}$.

The only quantities known are $n_{\mathrm{ss,ij}}$, $n_{\mathrm{os,ij}}$, and the mis-identification rates $\epsilon_i$ and $\epsilon_j$, while $\bar{n}_{\mathrm{ss,ij}}$ and $\bar{n}_{\mathrm{os,ij}}$ are unknown. However, the following relation holds

$$n_{\mathrm{os,ij}} = \bar{n}_{\mathrm{os,ij}} - \bar{n}_{\mathrm{os,ij}} \times p_{ij} + \bar{n}_{\mathrm{ss,ij}} \times p_{ij},$$

which reflects the fact that the number of opposite-sign lepton pairs counted in the bin pair $(i,j)$ is the corresponding truth-level number minus the portion that is identified as same-sign plus the contribution from truth-level same-sign pairs. This may be re-written as

$$n_{\mathrm{os,ij}} = \bar{n}_{\mathrm{os,ij}} \times (1 - p_{ij}) + \bar{n}_{\mathrm{ss,ij}} \times p_{ij}.$$

Similarly we have the following relation

$$n_{\mathrm{ss,ij}} = \bar{n}_{\mathrm{ss,ij}} \times (1 - p_{ij}) + \bar{n}_{\mathrm{os,ij}} \times p_{ij}.$$

Thus there are two equations in two unknowns and as a result $\bar{n}_{\mathrm{os,ij}}$ and $\bar{n}_{\mathrm{ss,ij}}$ may be solved.

In ATLAS, charge mis-identification rates are also provided to different analyses as scale factors (the ratios of charge mis-identification rates in data over those in simulation), to be applied to charge mis-identification rates in simulations to match the data. If charge mis-identification rates on data are provided directly instead of the scale factors, and if the control region has the same selections as the signal region except for the signs of the charges selected, we can avoid the need for the use of all systematic uncertainties that are associated with the use of simulation samples.

## 5.3. Conclusions

This chapter describes the electron charge mis-identification problem in ATLAS and how the charge mis-identification rates are extracted by fitting a Poisson likelihood function using the $Z \to e^+e^-$ data sample, collected at 8 TeV LHC center-of-mass energy in 2012 with the ATLAS detector and corresponding to an integrated luminosity of 20.3 fb$^{-1}$. Three sets of charge mis-identification rates are measured and provided to ATLAS analyses, corresponding

to three different sets of selection requirements (Medium, Tight + Isolation, and Tight + Isolation + impact parameter). The rates show a variation from less than 1% to nearly 10% depending on $\eta$ and $p_T$. It is also observed from the measurements that, in general, simulation overestimates the charge mis-identification rates as compared to those in the data.

In Run 2, in addition to measuring the charge mis-identification rates, a separate effort was started by the physics team at Université de Montréal, aiming at reducing charge mis-identification. The technique relies on the output of a boosted decision tree using a simulated sample of single electrons. Figure 3 shows the impact of applying the BDT requirement on charge mis-identification rates; it has been demonstrated to reduce charge mis-identification rates by about a factor of 10 while maintaining a 97% efficiency on signal electrons. More details may be found in Ref. [**43**].
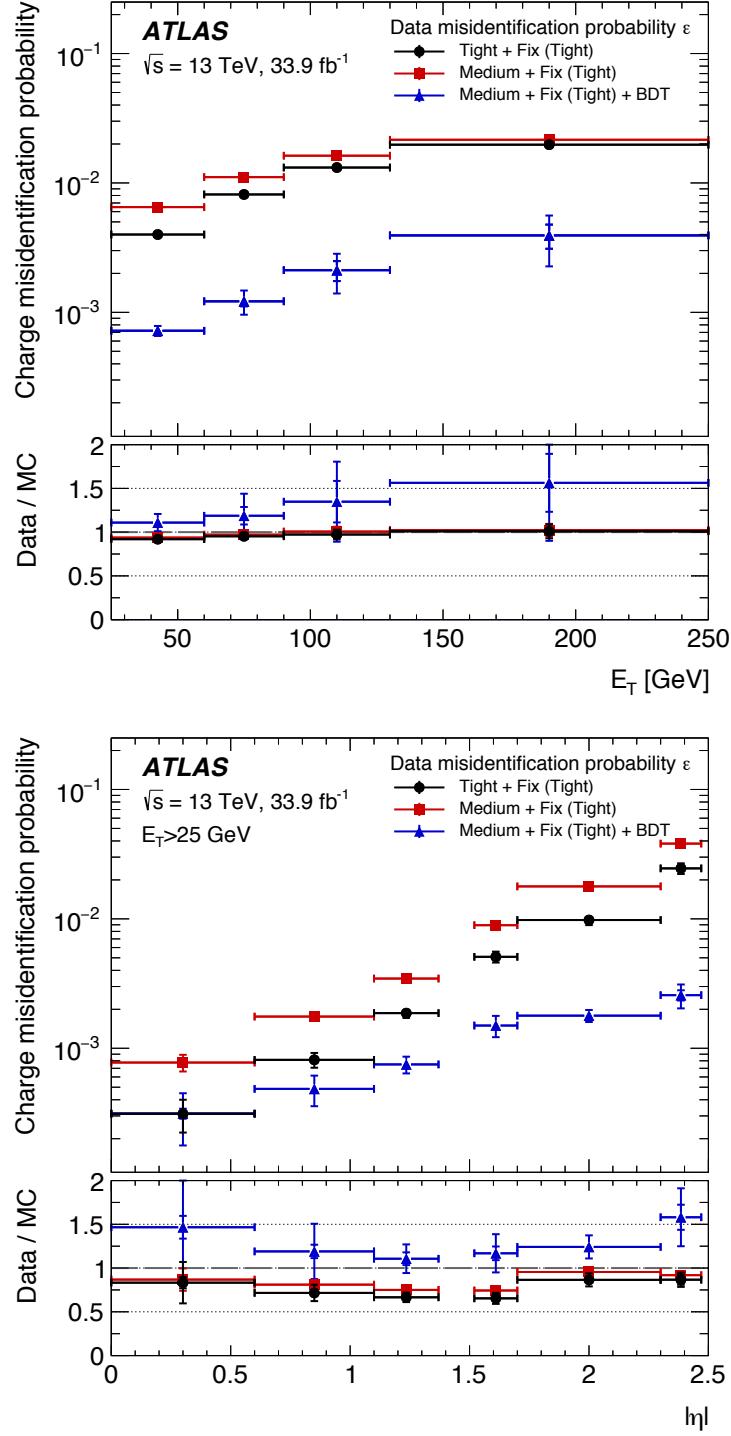
**Fig. 3.** Charge mis-identification probabilities in 2016 data and $Z \rightarrow e^+e^-$ events as a function of $E_T$ (top) and $|\eta|$ (bottom) that shows also the impact of applying the BDT requirement (in blue) to suppress charge mis-identification. In the legend, "Fix" means that a fixed isolation requirement is applied on the electron candidates [43].

# Chapter 6

---

# SEARCH FOR SUPERSYMMETRY IN EVENTS WITH MISSING TRANSVERSE MOMENTUM AND MULTIPLE $B$-JETS

Supersymmetry (SUSY) [**21, 22, 23, 24, 25, 26**] is an extension of spacetime symmetries (Section 2.2). Not only does SUSY unify fermions and bosons, it also potentially solves a number of problems, including the hierachy problem and the nature of dark matter. It is a leading candidate for beyond-the-Standard-Model physics.

Searching for SUSY is one of the most active research topics at ATLAS. This chapter discusses a SUSY search that targets gluino pair-production, where the final state includes missing transverse energy and multiple jets, of which at least three must be $b$-tagged jets. Section 6.1 presents an introduction to the gluino pair-production model. Section 6.2 discusses the data and simulation samples that are used in the analysis. Section 6.3 discusses the physics objects involved. Section 6.4 discusses event selection. Section 6.5 discusses analysis strategies and the results of the search. Section 6.6 discusses the interpretation of the search. Finally, some conclusions are given in Section 6.7.

The data were collected in the period 2015–2016, at 13 TeV centre-of-mass energy and corresponds to an integrated luminosity of 36.1 fb$^{-1}$.

## 6.1. Gluino Pair-Production

The hierarchy problem in the Standard Model (Section 2.2.1) is solved in SUSY provided the superpartners of the top quarks, the stops, are relatively light (masses at the electroweak scale $\sim$ O(100) GeV) [**56**]. This in turn implies the superpartners of the gluons, the gluinos, to have masses $\sim$ O(1) TeV [**57**]. In R-parity conserving SUSY theories, the gluinos are produced in pairs with a cross section much larger than the cross section for direct pair produced stops. As a result, searching for gluinos decaying into stops and sbottoms is highly motivated at ATLAS.

The gluino pair-production models in this analysis are called Gbb and Gtt. They belong to the class of simplified models[1] [**58, 59**], and are used to optimize search event selections as well as to interpret the search results. In terms of signature, these simplified models always contain at least four $b$-jets that originate either from gluino or top quark decays, and two neutralinos.

In Gbb and Gtt, the gluinos, which are superpartners of the Standard Model gluons, are hypothesized to be produced in pairs (Figure 1). Each of the gluino $\tilde{g}$ in the pair $\tilde{g}\tilde{g}$ is assumed to decay into a $\tilde{b}\bar{b}$ pair (in Gbb) or a $\tilde{t}\bar{t}$ pair (in Gtt) at 100% branching ratio[2]. In both models the supersymmetric $\tilde{t}$ is assumed to be off-shell and massive, and therefore implies a three-body decay of the gluino; this assumption has been found to have a small impact on the search while at the same time simplifying the analysis and the interpretation of the results [**60**]. Accordingly the parameters of the models consist of only two parameters, the mass of $\tilde{g}$ and the mass of $\tilde{\chi}^0_1$. The $\tilde{\chi}^0_1$'s are assumed to be the lightest supersymmetric particles; they are stable and serve as candidates for dark matter.
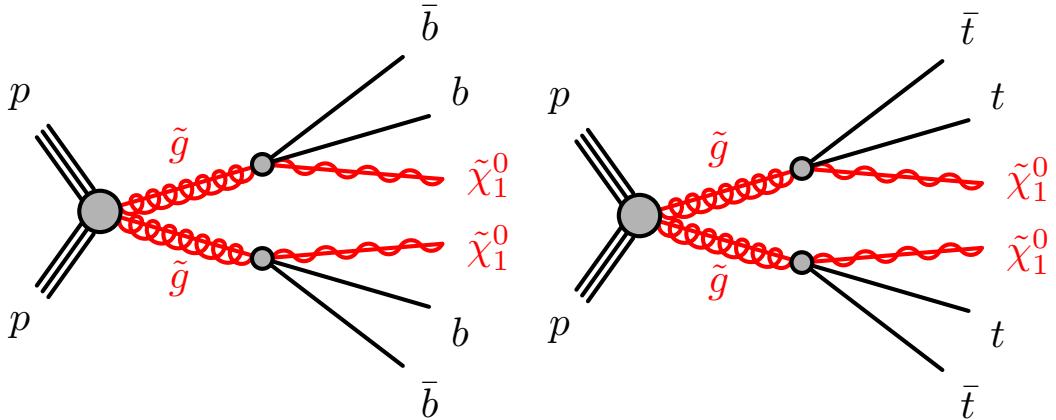


**Fig. 1.** The Gbb and Gtt models. Both belong to the class of simplified SUSY models. In both models, the supersymmetric $\tilde{t}$ is assumed to be off-shell. The parameters of the models are the mass of $\tilde{g}$ and the mass of $\tilde{\chi}^0_1$.

In the present chapter the Gtt model search is discussed in detail[3]. Because of the top quark decay mode $t \to Wb$, and the subsequent decays of the four $W$ bosons, we expect signal regions in Gtt to have higher jet multiplicity than those in Gbb. The final state is anticipated to consist of

- Four $b$-jets from the decays of the four top quarks.

---

[1]Generally simplified models can be understood as limits of more complete models, each of which focuses on a specific signature and involves only a few particles and decay modes.

[2]The possibility that one gluino in the pair will decay to $\tilde{t}\bar{b}$ and the other will decay to $\tilde{t}\bar{t}$ is not discussed in the present chapter, however it has been studied [**60**].

[3]It is connected directly with my contribution to the analysis. Moreover, as will be mentioned later, my contribution is also connected directly with the leptonic final state of the analysis.

- As many as twelve jets if all $W$ bosons' decays are purely hadronic, or otherwise additional jets and leptons (electrons or muons, the number of which depends on the number of leptonic $W$ boson decays), along with missing transverse energy from the daughter neutrinos of the $W$ bosons and the $\tilde{\chi}_1^0$'s, assuming the latter do not participate in known interactions and manifest themselves as missing transverse energy.

The full analysis includes a leptonic and a hadronic channel. In this chapter, only the leptonic final state is discussed in detail; it consists of one or more leptons, large missing transverse energy, and multiple jets in which at least three must be identified as $b$-jets. As will be discussed in the following section, at 13 TeV we expect so-called boosted top quark decays and consequently an increasing number of leptons found inside the $b$-jets. This motivates the use of a new overlap removal scheme as well as the measurements of the identification efficiencies for such electrons. The former will be discussed in Section 6.3 and the latter was developed after the analysis presented in the current section, and will be the topic of Chapter 7.

## 6.2. Data and Simulated Event Samples

The data used in the analysis were collected by the ATLAS detector [**39**] in the period 2015–2016, delivered by the LHC at 13 TeV centre-of-mas energy and 25 ns bunch spacing. The full data corresponds to an integrated luminosity of 36.1 fb$^{-1}$, of which the associated uncertainty is 2.1% [**61**]. An HLT $E_{\mathrm{T}}^{\mathrm{miss}}$ trigger is applied on the data at three online thresholds, 70 GeV for 2015, 100 GeV for early 2016, and 110 GeV for late 2016. The trigger is fully efficient for the events that pass the preselection requirement defined in Section 6.4.2, which imposes the offline condition $E_{\mathrm{T}}^{\mathrm{miss}} > 200$ GeV.

Most of the signal and background processes considered in this analysis are generated using simulations, described below. An exception is the multi-jet process, which is estimated from data, and which is only non-negligible for the all-hadronic channel. All simulated event samples were passed through the full ATLAS detector simulation using Geant4 [**62**].

SUSY signal samples. The signal processes, where gluino pairs $\tilde{g}\tilde{g}$ are produced and each member in the pair decays according to $\tilde{g} \to t\bar{t}\tilde{\chi}_1^0$, are generated with up to two additional partons using MadGraph5_aMC@NLO [**63**] at leading order, the parton distribution function (PDF) set being NNPDF 2.3 [**64**]. The samples are interfaced to Pythiav8.186 [**65**] for parton showering, hadronization, and underlying events. All signal samples are normalized with NLO cross-section calculations.

Standard Model background samples. The dominant background is $t\bar{t}$ plus high $p_T$ jets. It is generated with the Powheg-Box [**66**] v2 event generator using the CT10 [**67**] PDF set,

interfaced with PYTHIAv6.428. Events in which all the top quarks decay hadronically are excluded because of insufficient $E_{\mathrm{T}}^{\mathrm{miss}}$ to constitute a significant background.

The POWHEG-BOX v2 event generator is also used for single top quark in the $Wt$- and $s$- channels, along with the CT10 PDF set and PYTHIAv6.428. POWHEG-BOX v1 is used for the $t$- channel process. All events with at least one $W$ boson that decays leptonically are included, and events in which all top quarks decay hadronically are excluded because of insufficient $E_{\mathrm{T}}^{\mathrm{miss}}$.

Smaller background contributions include $t\bar{t}$ plus $W/Z/h$ possibly along with jets, and $t\bar{t}t\bar{t}$, $W/Z$+jets, and $WW/WZ/ZZ$ events. Their generations are described below:

- $t\bar{t}$ plus $W/Z$: MADGRAPH5_aMC@NLO v2.2.2 and PYTHIAv8.186. The PDF set is NNPDF 2.3.
- $t\bar{t}h$: MADGRAPH5_aMC@NLOv2.2.1 and HERWIG++ [68] v2.7.1. The PDF set is CT10.
- $t\bar{t}t\bar{t}$: MADGRAPH5_aMC@NLOv2.2.2 and PYTHIAv8.186.
- $W/Z$+jets: SHERPAv2.2.0 [69] and the NNPDF 3.0 PDF set.
- $WW/WZ/ZZ$: SHERPAv2.1.1 and the CT10 PDT set.

Other potential sources of backgrounds, such as three top quark or three gauge boson processes, have been determined to be negligible.

## 6.3.  Physics Objects

Physics objects that are used to select events for the analysis are described in this section. The main objects, electrons, muons, and jets, are required to undergo an overlap removal procedure to remove double-counting. The overlap removal procedure is described in the section as well.

Interaction vertices. Each interaction vertex in the event is required to be associated with at least two tracks, each of which must have $p_T > 0.4$ GeV. The primary vertex is defined to be the vertex that has the largest sum of squares of transverse momenta of the associated tracks [70].

Jets. Candidate jets are reconstructed using the anti-$k_t$ jet algorithm [71, 72, 73] with a radius parameter $\Delta R = 0.4$; these jets will be referred to as small $R$-jets. They are required to have $p_T > 20$ GeV and $|\eta| < 2.8$, and must undergo an overlap removal procedure with electrons and muons, described below, after which they are required to pass the requirement $p_T > 30$ GeV.

An event is rejected if it contains jets that arise from non-collision sources or detector noise or pile-up interactions [74].

*b*-jets. The hadronization of a *b*-quark in the event creates a physics object referred to as a *b*-jet. A *b*-hadron has a lifetime of about $10^{-12}$ s and decays after travelling a short distance (typically mm) from the primary vertex, creating a secondary vertex from which additional tracks originate (Figure 2 [75]). The *b*-jets in the event are identified by a multivariate algorithm, which relies on three pieces of information: The impact parameters of the tracks that belong to the jets, the secondary vertices that are present in the event, and the flight paths of heavy hadrons inside the jets [76, 77]. Identifying *b*-jets using the algorithm is referred to as *b*-tagging. In this analysis the *b*-tagging working point that corresponds to a 77% efficiency for *b*-jets with $p_T > 20$ GeV is chosen, which has a rejection factor of 6 on charm and 134 on light-jets.
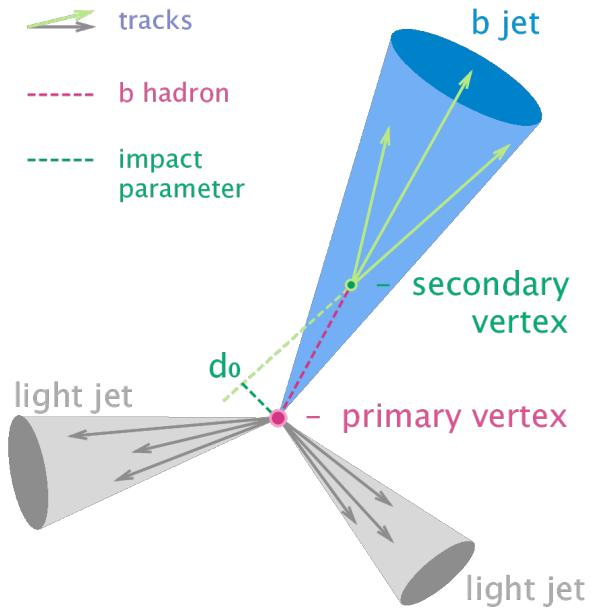


**Fig. 2.** *b*-jet secondary vertex which is displaced with respect to the primary vertex. In addition to tracks that originate from the primary vertex there are tracks that originate from the secondary vertex as well [75].

Large *R*-jets. These jets refer to jets that are re-clustered from the small *R*-jet candidates [78] that have undergone overlap removals with electrons and muons, using the anti-$k_t$ algorithm with $R = 0.8$. These large *R*-jets are required to have $p_T > 100$ GeV and $|\eta| < 2.0$. They are a tool to identify boosted top quarks, as a boosted top quark that decays hadronically will produce jets that stay collimated to each other (Figure 3). In Gtt, this is expected in events with a large mass difference between the gluino and the neutralino.
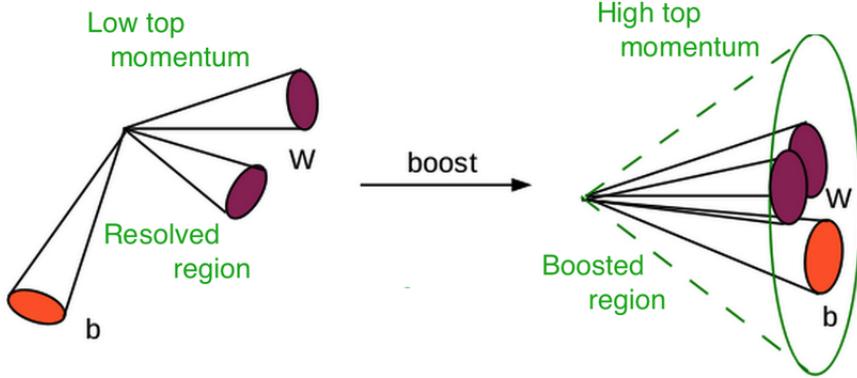
**Fig. 3.** Boosted top quark decay (right) compared to low-$p_T$ top quark decay. In the former case, the decay products stay collimated.

Leptons. The leptons in the analysis include electrons and muons. Initially, each electron candidate must pass the Loose quality criteria [**49, 79**] and is required to have $|\eta| < 2.47$. On othe other hand, each muon candidate must pass the Medium quality criteria [**80**] and must have $|\eta| < 2.5$.

Subsequently, the leptons undergo overlap removal and those passing this step are required to pass an isolation requirement, in order that fake and non-prompt leptons from jets may be removed. This isolation requirement uses a $p_T$-dependent cone with radius $\min(0.2, 10 \text{ GeV}/p_T^{\text{lep}})$, where $p_T^{\text{lep}}$ is the $p_T$ of the lepton, to take into account the fact that the angular separation between a lepton in the event and the $b$-jet narrows as $p_T$ of the top quark increases (Figure 3).

Signal leptons are selected as follows. Electrons are required to pass the Tight quality criteria [**49, 79**]. They are also matched to the primary vertex by requiring the ratio $|d_0|/\sigma_{d_0}$, where $d_0$ is the transverse impact parameter of the associated ID track and $\sigma_{d_0}$ is the measured uncertainty of $d_0$, to be $< 5$, as well as the longitudinal impact parameter $z_0$ to satisfy $|z_0 \sin\theta| < 0.5$ mm. On the other hand, muons are matched to the primary vertex by requiring $|d_0|/\sigma_{d_0} < 3$ and $|z_0 \sin\theta| < 0.5$ mm. Events that contain muons with $d_0 > 0.2$ mm or $z_0 > 1$ mm are rejected to suppress cosmic muons.

Missing Transverse Energy. This is defined as the magnitude of the negative vector sum of the transverse momenta of all calibrated objects in the event, with an extra term [**81, 82**] to account for energy deposits not associated with any of the selected objects.

Overlap Removal. Electrons, muons, and jets are required to undergo the following sequential overlap removal procedure.

- Electrons found inside $\Delta R < 0.01$ of a muon candidate are removed, to suppress contributions from muon bremsstrahlung.
- Next, overlap removal between electrons and jets are performed, in order to remove electrons reconstructed as jets, which is the case for electrons reconstructed at AT-LAS, as well as fake electrons from hadron decays. Thus, reconstructed non-$b$-tagged jets whose centroids lie within $\Delta R < 0.2$ of electrons are removed, unless the jets are $b$-jets, because then the electrons are likely to originate from semileptonic $b$-hadron decays. Subsequently, electrons with $E_T < 50$ GeV found within $\Delta R = 0.4$ of jets are removed while the jets are kept. Electrons with higher $E_T$ are likely to be in boosted top quark decays, in which case they are expected to be found closer to the jets the higher are their $E_T$. Accordingly, a distance[4] that takes into account this fact is used, $\Delta R = \min(0.4, 0.04 + 10 \text{ GeV})/E_T$, and any electron found within $\Delta R = 0.4$ of a jet will be treated as a potential signal electron, as long as its $E_T$ is high enough.
- Finally, overlap removal is applied on the remaining muons and jets. If a non-$b$-tagged-jet having fewer than three inner detector tracks whose centroid is found within a distance $\Delta R = 0.2$ of a muon, the jet is likely to come from high-$p_T$ muon bremsstrahlung and is removed. Then muons with $p_T < 50$ GeV that are found within $\Delta R = 0.4$ of jets are removed, to suppress non-prompt muons originating from jets. Muons having $p_T > 50$ GeV are, as in the case of high $E_T$ electrons, subject to the $p_T$-dependent overlap removal distance $\Delta R = \min(0.4, 0.04 + 10 \text{ GeV})/p_T$.

Boosted Overlap Removal Studies. The use of electrons inside jets had been initiated by the $t\bar{t}$ resonance search [**83**] in order to gain signal electron acceptance in scenarios that involve the decays of beyond-Standard-Model particles into the Standard-Model top quarks. Following the idea, the $p_T$-dependent distance $\Delta R = \min(0.4, 0.04 + 10 \text{ GeV})/p_T$ was studied, optimized, and introduced into the current analysis (first applied to 3.2 fb$^{-1}$ of data) for muons before being subsequently adopted for electrons in a later version of the analysis (at 36.1 fb$^{-1}$). The optimization study for muons was carried out on three samples, a $t\bar{t}$ sample, a Gtt sample where the mass of the gluino is 1300 GeV and that of the neutralino is 900 GeV, and another Gtt sample where the mass of the gluino is 1600 GeV and that of the neutralino is 100 GeV. The last sample, due to a large mass difference between the gluino and the neutralino, is also called a boosted sample, since it is expected to be a source of boosted top quarks. Figure 4, which plots the distance $\Delta R$ between the truth level muons and the closest jets, shows a large fraction of potential signal muons below $\Delta R = 0.4$ in the boosted sample. The other signal sample shows a smaller but still considerable fraction of potential signal muons below $\Delta R = 0.4$, most likely due to random overlap between the muons and

---

[4]The angular separation $\Delta R$ between the decay products of a particle of mass $m$ and tranverse momentum $p_T$ is given approximately by $2m/p_T$.

the top quarks (there are four top quarks as compared to two in the $t\bar{t}$ sample, the latter displays instead a mild peak in the region $\Delta R > 0.4$).
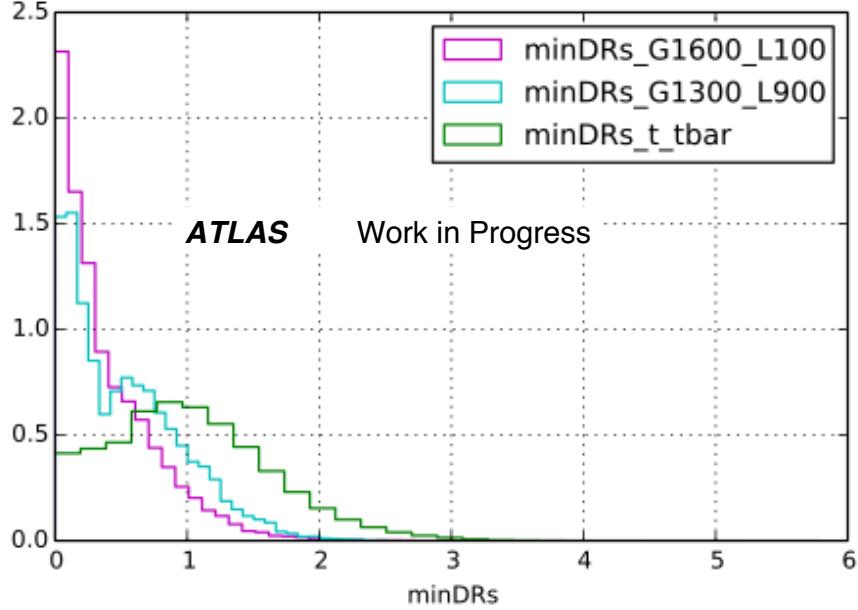


**Fig. 4.** $\Delta R$ between the truth-level muons and the closest jets. The boosted sample (in pink) where mass of the gluino is 1600 GeV and that of the neutralino is 100 GeV shows a high peak at low $\Delta R$. The other signal sample (in cyan) also displays but not as high. The $t\bar{t}$ sample (in green), exhibits a mild peak around $\Delta R = 1.0$.

The study consisted in optimizing the statistical significance of the SUSY signal as a function of the overlap-removal parameters. The adopted parameters results in a 15% gain in statistical significance as compared to the scheme in which a fixed $\Delta R = 0.4$ is used.

## 6.4. Event Selection

In this section the discriminating variables (Section 6.4.1) and the preselection criteria (Section 6.4.2) are discussed. The latter section also includes a discussion of the modelling of the data. Finally, the optimization of some important variables is discussed in Section 6.4.3.

### 6.4.1. Discriminating Variables

The following list of variables is found to be discriminating between signal and Standard Model backgrounds:

- The effective mass $m_{\text{eff}}$, defined as the scalar sum of missing transverse energy plus the transverse momenta of jets and leptons in the event:

$$m_{\text{eff}} = \sum_i p_T^{\text{jet}_i} + \sum_j p_T^{l_j} + E_{\text{T}}^{\text{miss}}.$$

This variable is typically much higher for signal events than for background events. It reflects the overall energy scale of the event, and is accordingly correlated to the masses of the SUSY particles in the signal.

- The transverse mass $m_{\text{T}}$, defined by

$$m_{\text{T}} = \left( 2 p_T^l E_{\text{T}}^{\text{miss}} \left( 1 - \cos(\Delta\phi) \right) \right)^{1/2},$$

where $\Delta\phi$ is the angle between missing transverse momentum of the event and the transverse momentum of the leading lepton.

In background events in which there is one $W$ boson that decays leptonically, such as in semileptonic $t\bar{t}$ and $W$+jets, this variable reaches a maximum at the value of the $W$ boson mass. It is expected to be higher for signal events where there are additional sources of missing transverse energy such as from the neutralinos.

- The transverse mass $m_{\text{T,min}}^{\text{b-jets}}$ defined by

$$m_{\text{T,min}}^{\text{b-jets}} = \min_{i\leq3} \left( 2 p_T^{\text{b-jets}_i} E_{\text{T}}^{\text{miss}} \left( 1 - \cos(\Delta\phi) \right) \right)^{1/2},$$

where $\Delta\phi$ is the angle between the missing transverse momentum and the $i$-th b-jet. Only the three highest pt $b$-jets are considered in the calculation of the mass.

In background $t\bar{t}$ events where a single top quark decays leptonically, this variable reaches a maximum at the value of the top quark mass. It is expected to be higher for signal events because of the additional source of missing transverse energy from the neutralinos.

- The total jet mass $M_J^{\Sigma}$, defined by

$$M_J^{\Sigma} = \sum_{i\leq4} m_{J,i},$$

where $m_{J,i}$ is the mass of the $i$-th large-radius re-clustered jet in the event. It is higher for signal events, because there are as many as four hadronically decaying top quarks, whereas the background is dominated by $t\bar{t}$ events where one or both of the tops decay leptonically. We note that dilepton $t\bar{t}$ becomes dominant after applying selections on $m_T$ and $m_{\text{T,min}}^{\text{b-jets}}$ defined above (Section 6.5).

## 6.4.2. Preselection and Modelling of the Data

Preselection. The preselection requirements include $E_{\mathrm{T}}^{\mathrm{miss}} > 200$ GeV, in addition to the $E_{\mathrm{T}}^{\mathrm{miss}}$ trigger requirement, at least one electron or muon, and at least four small $R$-jets of which at least two must be identified as $b$-jets.

Modelling of the Data. In the preselection sample, correction factors need to be extracted to account for shape discrepancies between data and the expected background for $m_{\mathrm{eff}}$. Thus, background-dominated regions are defined by requiring exactly two $b$-jets and $m_{\mathrm{T,min}}^{\mathrm{b\text{-}jets}} <$ 140 GeV, in which the correction factors are taken to be the ratio of the number of observed events to the predicted number of background events in a given $m_{\mathrm{eff}}$ bin. The correction factors range from 0.7 to 1.1; they are also taken as an uncertainty for both background and signal events.

Figure 5 show a number of variables after preselection, including the number of jets, the number of $b$-jets, $E_{\mathrm{T}}^{\mathrm{miss}}$, $m_{\mathrm{eff}}$, $M_J^{\Sigma}$, and $m_{\mathrm{T}}$, all having had the $m_{\mathrm{eff}}$ correction factor applied. The uncertainties shown include the statistical and experimental systematic uncertainties (Section 6.5.3), but exclude the theoretical uncertainties in background modelling.
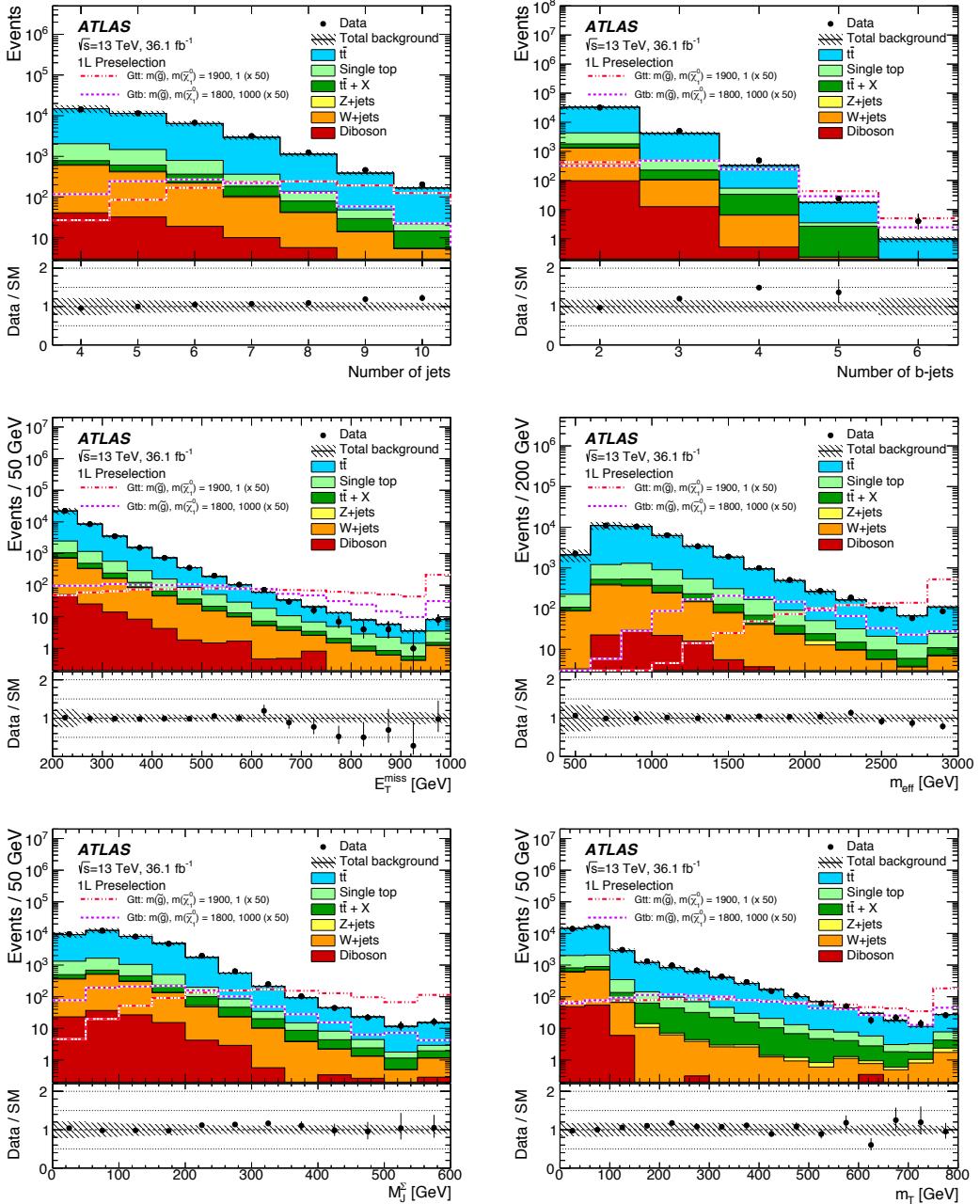
**Fig. 5.** The distributions of the number of jets, the number of $b$-jets, $E_{\mathrm{T}}^{\mathrm{miss}}$, $m_{\mathrm{eff}}$, $M_J^{\Sigma}$, and $m_{\mathrm{T}}$ after the preselection requirements. The uncertainty includes both statistical and experimental systematatic uncertainties (defined in Section 6.5.3). The last bin includes overflow events. The ratio of data to background prediction is also shown below each figure.

### 6.4.3. Optimization of Discriminating Variables

An optimization study was performed, at 25 fb$^{-1}$ luminosity, to optimize the selections for the leptonic channel of the analysis[5].

The number of jets (Section 6.3), $N_{\text{jet}}$, missing transverse energy, $E_T^{\text{miss}}$, and $m_{\text{eff}}$ are important variables that help with separating signal and background events. In the current analysis, a study was performed to decide on the optimal values of these variables (and of other potentially discriminating variables also). To this end, four samples were selected; they may be put into three groups:

- One sample where the mass of the gluino is 1900 GeV and that of the neutralino is 200 GeV. This will be referred to as the boosted sample, since it is expected to be a source of boosted top quarks.
- One sample where the mass of the gluino is 1900 GeV and that of the neutralino is 1000 GeV; this is a moderately boosted sample.
- Two samples in which the mass differences between the gluino and the neutralino are small. One sample has 1200 GeV and 800 GeV, and one has 1500 GeV and 1000 GeV, which will be called compressed samples number one and two respectively.

The optimization proceeds with different sets of values of potentially discriminating variables, among them including sets in which

- $N_{\text{jet}} \geq 6$, or $N_{\text{jet}} \geq 7$, or $N_{\text{jet}} \geq 8$, or $N_{\text{jet}} \geq 9$, or $N_{\text{jet}} \geq 10$;
- $E_T^{\text{miss}} > 200$ GeV, or $E_T^{\text{miss}} > 300$ GeV, or $E_T^{\text{miss}} > 400$ GeV, or $E_T^{\text{miss}} > 500$ GeV, or $E_T^{\text{miss}} > 600$ GeV;
- $m_{\text{eff}}$ is allowed to varied from 500 GeV to 3500 GeV, in steps of 200 GeV.

All possible combinations of the values of the variables are studied, using the search significance `BinomialExpZ` of `RooStats` defined according to the CLs method [**84, 85**], assuming a flat systematic uncertainty of 30% (taken from experience with previous analyses). The optimization finds that higher number of jets improve the search significance, especially for samples in which the mass differences between the gluino and the neutralino are small (the compressed samples). This is consistent with the fact that a small mass difference makes kinematic properties of the signal, such as $E_T^{\text{miss}}$, quite indistinguisable from those of the background, and consequently we have to push to the higher $N_{\text{jets}}$ regime. Figure 6 shows the significance as the number of jets is allowed to increase while all other variables are kept fixed, for the compressed sample number two. The red point indicates the best significance. Using this result, a higher number of jets was adopted in the definitions of the signal regions discussed in Section 6.5.2.

---

[5]As has been mentioned, the chapter focuses only on the leptonic channel and as such the fully hadronic channel, which was optimized separately, is not discussed in the current section.

The optimization also suggests that higher $E_{\mathrm{T}}^{\mathrm{miss}}$ would help when more data becomes available in future LHC run. Figure 7 shows the significance as $E_{\mathrm{T}}^{\mathrm{miss}}$ is allowed to increase while all other variables are kept fixed, for the boosted sample where the masses are 1900 GeV and 200 GeV.

As for $E_{\mathrm{T}}^{\mathrm{miss}}$, the optimization also suggests higher $m_{\mathrm{eff}}$ would help when more data becomes available in future LHC run. Figure 8 shows the significance as $m_{\mathrm{eff}}$ is allowed to increase while all other variables are kept fixed, for the boosted sample.

The optimization also discovered that the ratio $E_{\mathrm{T}}^{\mathrm{miss}}/m_{\mathrm{eff}}$, also called $E_{\mathrm{T}}$ significance, was potentially discriminating, in particular in compressed regions (Figure 9). Following this study, this variable has been adopted in the SUSY search with two same-sign leptons [86].
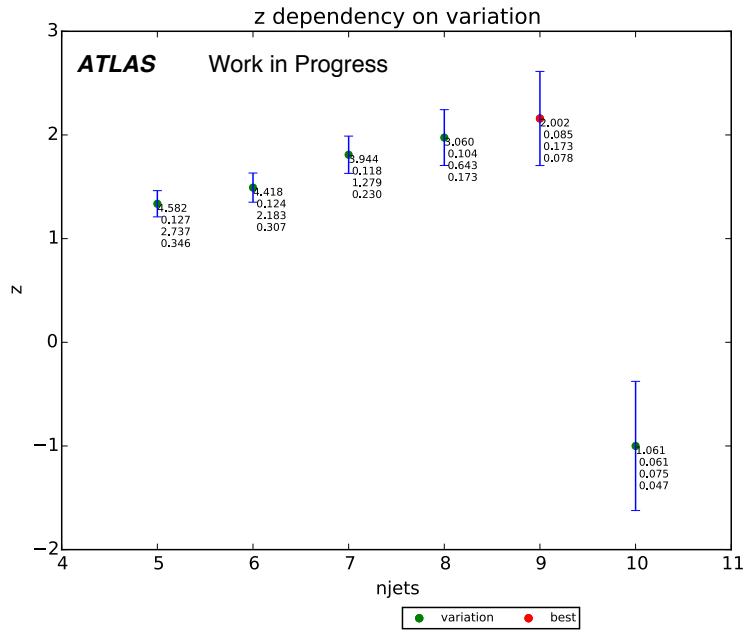


**Fig. 6.** The significance with respect to $N_{\mathrm{jets}}$ for the compressed sample number two, where the masses are 1500 GeV and 1000 GeV, at 25 fb$^{-1}$ luminosity. The red point indicates the best significance, and the numbers that show up below the points are the signal, the signal uncertainty, the background, and the background uncertainty, in that order. Whenever the calculations of the significance is no longer meaningful, such as when the number of unweighted background events is below 1 event, the significance is set to $-1$.
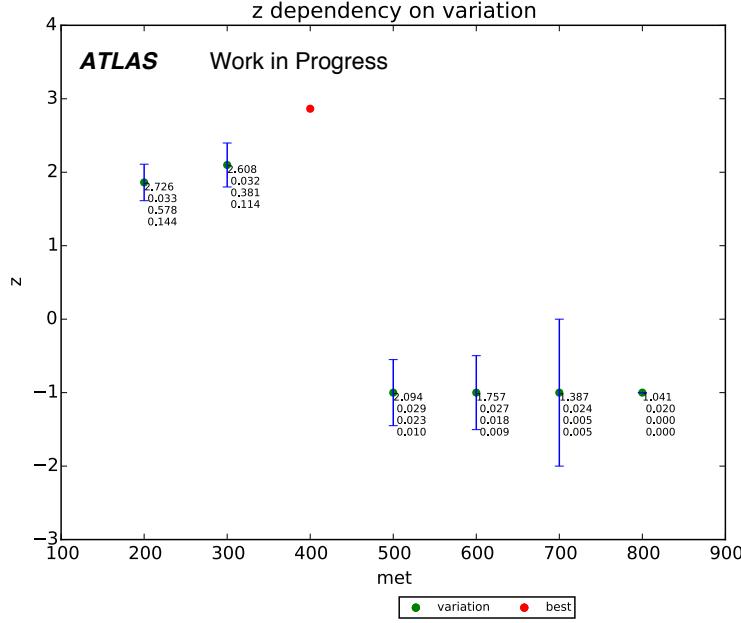
**Fig. 7.** The significance with respect to $E_T^{miss}$ for the boosed sample with masses 1900 GeV and 200 GeV, at 25 fb$^{-1}$ luminosity. The red point indicates the best significance, and the numbers that show up below the points are the signal, the signal uncertainty, the background, and the background uncertainty, in that order.
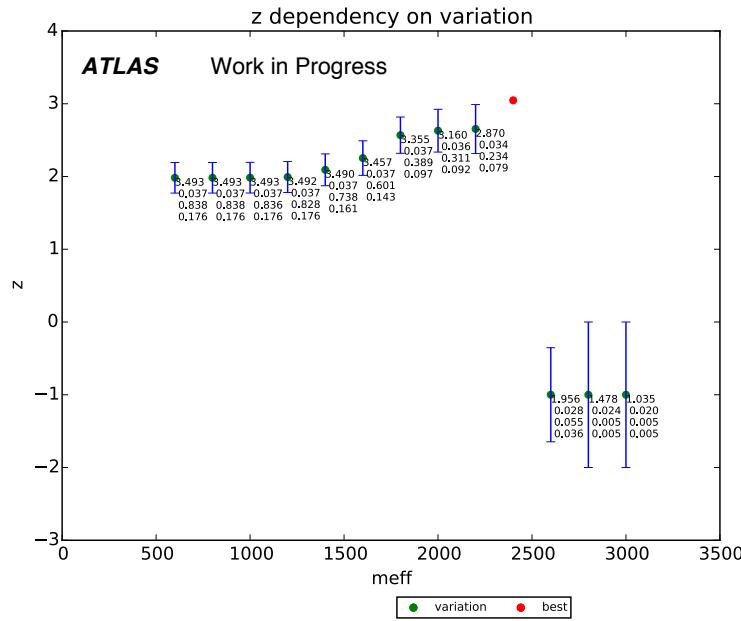


**Fig. 8.** The significance with respect to $m_{eff}$ for the boosted sample, where the masses are 1900 GeV and 200 GeV, at 25 fb$^{-1}$ luminosity. The red point indicates the best significance, and the numbers that show up below the points are the signal, the signal uncertainty, the background, and the background uncertainty, in that order.
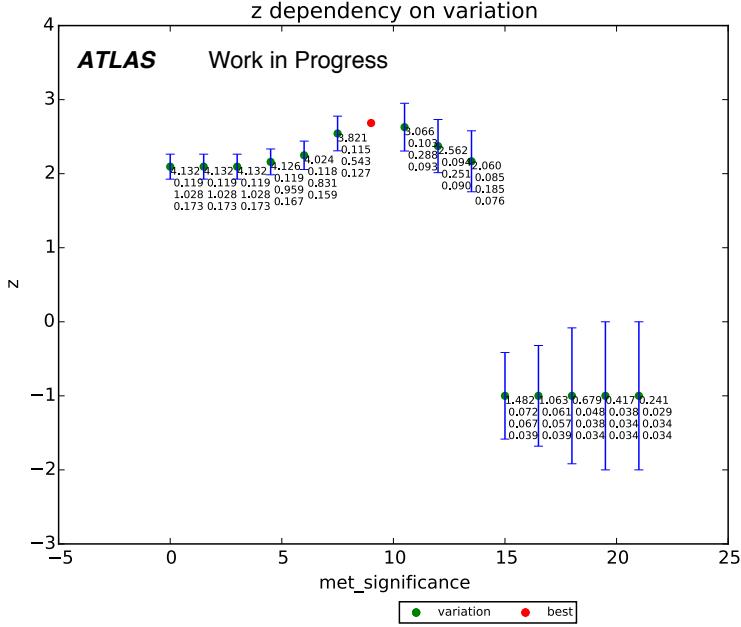
**Fig. 9.** The ratio $E_{\mathrm{T}}^{\mathrm{miss}}/m_{\mathrm{eff}}$ for the compressed sample number two, where the masses are 1500 GeV and 1000 GeV, at 25 fb$^{-1}$ luminosity. The red point indicates the best significance, and the numbers that show up below the points are the signal, the signal uncertainty, the background, and the background uncertainty, in that order.

## 6.5. Analysis and Results

A significant part of the analysis is the work of background estimation; it is discussed in Section 6.5.1. There are two search strategies, discussed in Section 6.5.2. Section 6.5.3 discusses the evaluation of systematic uncertainties, and Section 6.5.4 discusses the results of the search.

### 6.5.1. Background Estimation

Each signal region that is defined is contaminated with Standard Model backgrounds, the dominant source of which is $t\bar{t}$ plus jets, which is estimated using a normalization factor. This factor, which is obtained from data, will be applied on top of the simulation prediction. To this end, in addition to each signal region (SR), a control region (CR), orthogonal to the signal region, but otherwise comparable with it in terms of background composition and kinematics, is defined. Signal contamination in the control region is suppressed by inverting or relaxing some kinematic variables. The normalization factor is then verified in validation regions (VRs), designed to be similar to the signal region in terms of background composition.

The remaining backgrounds are made up of single-top, $W$+jets, $Z$+jets, $t\bar{t}+W/Z/h$, $t\bar{t}t\bar{t}$ and diboson events. They are estimated from simulations, which are normalized to the best

available theoretical cross sections. The multijet background was found to be negligible, but is still estimated using a procedure described in Ref.[**87**].

## 6.5.2. Analysis Strategy

Physics objects in the final state may fall into different kinematic ranges. These objects consist of those coming from Standard Model events as well as those coming from the hypothetical SUSY events. Naturally, not all kinematic ranges will be equal in terms of the relative distributions of the two kinds of events. The signal and background samples allow us to optimize, i.e. to arrive at one or more sets of kinematic ranges where we will have the best chances to assess whether or not an excess of events, relative to Standard Model distribution, is seen. This assessment can be based solely from judging the excess of events, and is referred to as the cut-and-count strategy. In this strategy, possibly overlapping kinematic regions targetting different gluinos masses are defined, to seek to answer the question if an excess of events is seen at all, in which case we may claim to have seen a signal, or to rule out the existence of any beyond-the-Standard-Model signal, if the number of events seen in fact does not deviate in any statistically significant way from the Standard Model prediction.

On the other hand, it is possible to design several non-overlapping signal regions that can be statistically combined to obtain an optimal excluding limits on the Gtt and Gbb processes. This strategy is called the multi-bin analysis.

Both strategies are followed in the current analysis for the hadronic channel as well as for the leptonic channel. However, only the leptonic channel will be discussed in the following.

Cut-and-Count Analysis. In this analysis strategy the signal points are grouped into three classes. Thus there are three signal regions together with their corresponding control and validation regions. The common selections include $\geq 1$ lepton, $p_T^{\text{jet}} > 30$ GeV, and $N_{b\text{-jets}} \geq 3$. The choice of values of other discriminating variables differentiates one class from another. The definitions of the regions are shown in Table 1.

- Region B, where B stands for boosted, is optimized for signals having a large mass difference between the gluino and the neutralino ($\geq 1.5$ TeV).
- Region C, where C stands for compressed, is optimized for signals where the mass difference is small ($\leq 300$ GeV).
- Region M, where M stands for moderate, is the region where the mass difference is in between those of boosted and compressed regions.

As is shown in the table, the selections on $m_{\text{eff}}$, $E_{\text{T}}^{\text{miss}}$, and $M_J^{\sum}$ are lower in signal region C than other signal regions because a Gtt compressed spectrum produces softer objects. The increase in background as a result of the lower cuts is managed by making tighter selections

on the number of jets, the number of $b$-jets, or $m_{\mathrm{T,\,min}}^{b\text{-jets}}$. In signal region M, the selections on those variables are intermediate between those of signal region B and signal region C.

The CRs are defined in the low $m_{\mathrm{T}}$ region to remove overlaps with the SRs. The $m_{\mathrm{T,\,min}}^{b\text{-jets}}$ cut is removed, and cuts on other variables are lowered to make sure that each CR would have $\geq 10$ events, in order that the normalization of the $t\bar{t}$ background would be determined with sufficient statistical accuracy. On the other hand, there are two types of VRs, VR-$m_{\mathrm{T}}$ to validate background prediction in high $m_{\mathrm{T}}$ region, and VR-$m_{\mathrm{T,\,min}}^{b\text{-jets}}$ in the high $m_{\mathrm{T,\,min}}^{b\text{-jets}}$ region. These VRs are ensured to be kinematically close to the SRs and the CRs by the cut on $N_{\mathrm{jets}}$, which at the same time ensures their non-overlapping. Cuts on other variables are also used to keep the VRs non-overlapping with their corresponding SRs, specifically $M_{\mathrm{J}}^{\Sigma}$ or $m_{\mathrm{T,\,min}}^{b\text{-jets}}$ in VR-$m_{\mathrm{T}}$ and $m_T$ in VR-$m_{\mathrm{T,\,min}}^{b\text{-jets}}$.

<div align="center">

**Gtt 1-lepton**

Criteria common to all regions: $\geq 1$ signal lepton , $p_T^{\mathrm{jet}} > 30$ GeV, $N_{b\text{-jets}} \geq 3$

</div>

| Targeted kinematics | Type | $N_{\mathrm{jet}}$ | $m_{\mathrm{T}}$ | $m_{\mathrm{T,\,min}}^{b\text{-jets}}$ | $E_{\mathrm{T}}^{\mathrm{miss}}$ | $m_{\mathrm{eff}}^{\mathrm{incl}}$ | $M_{\mathrm{J}\Sigma}$ |
|---|---|---|---|---|---|---|---|
| Region B (Boosted, Large $\Delta m$) | SR | $\geq 5$ | $> 150$ | $> 120$ | $> 500$ | $> 2200$ | $> 200$ |
| | CR | $= 5$ | $< 150$ | – | $> 300$ | $> 1700$ | $> 150$ |
| | VR-$m_T$ | $\geq 5$ | $> 150$ | – | $> 300$ | $> 1600$ | $< 200$ |
| | VR-$m_{\mathrm{T,\,min}}^{b\text{-jets}}$ | $> 5$ | $< 150$ | $> 120$ | $> 400$ | $> 1400$ | $> 200$ |
| Region M (Moderate $\Delta m$) | SR | $\geq 6$ | $> 150$ | $> 160$ | $> 450$ | $> 1800$ | $> 200$ |
| | CR | $= 6$ | $< 150$ | – | $> 400$ | $> 1500$ | $> 100$ |
| | VR-$m_T$ | $\geq 6$ | $> 200$ | – | $> 250$ | $> 1200$ | $< 100$ |
| | VR-$m_{\mathrm{T,\,min}}^{b\text{-jets}}$ | $> 6$ | $< 150$ | $> 140$ | $> 350$ | $> 1200$ | $> 150$ |
| Region C (Compressed, small $\Delta m$) | SR | $\geq 7$ | $> 150$ | $> 160$ | $> 350$ | $> 1000$ | – |
| | CR | $= 7$ | $< 150$ | – | $> 350$ | $> 1000$ | – |
| | VR-$m_T$ | $\geq 7$ | $> 150$ | $< 160$ | $> 300$ | $> 1000$ | – |
| | VR-$m_{\mathrm{T,\,min}}^{b\text{-jets}}$ | $> 7$ | $< 150$ | $> 160$ | $> 300$ | $> 1000$ | – |

**Table 1.** Definitions of the 1-lepton Gtt SRs, CRs and VRs of the cut-and-count analysis. The jet $p_T$ requirement is also applied to $b$-tagged jets.

Multi-bin Analysis. In this analysis strategy a number of non-overlapping regions are defined using $N_{\mathrm{jet}}$ and $m_{\mathrm{eff}}$. The regions are shown schematically in Figure 10. In each region

signal models having a specified range of mass difference are used to optimize all remaining kinematic variables.
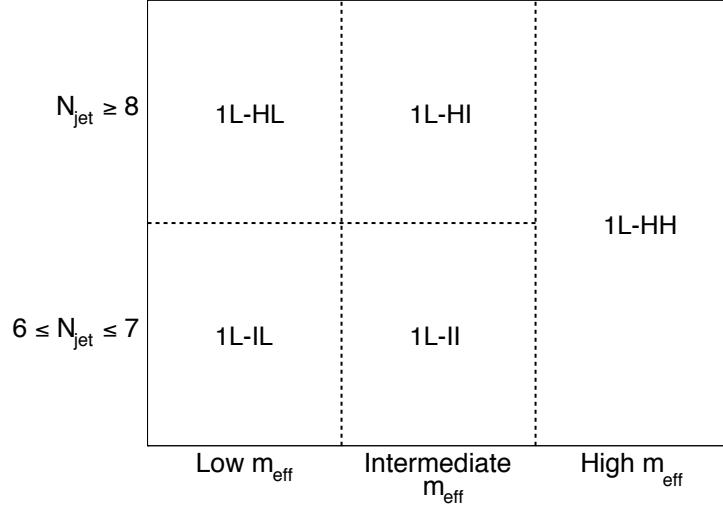


**Fig. 10.** Schematic illustration of the regions in the multi-bin analysis. This is a two-dimensional illustration in the variables $N_{\text{jet}}$ and $m_{\text{eff}}$.

The definitions of the regions are shown in Table 2, which shows high-$N_{\text{jet}}$ SRs, CRs, and VRs, and Table 3, which shows intermediate-$N_{\text{jet}}$ SRs, CRs, and VRs. The low $m_{\text{eff}}$ regions are designed for signals with low mass difference, while the high $m_{\text{eff}}$ for boosted events. For each SR, the CR is obtained by keeping most kinematic variables close while inverting the $m_{\text{T}}$ cut, so that there would be no overlapping with the SR. The VRs are obtained with cuts on $E_{\text{T}}^{\text{miss}}$ and $m_{\text{T, min}}^{b\text{-jets}}$.

**High-$N_{\rm jet}$ regions**

Criteria common to all regions: $N_{b\text{-jets}} \geq 3$, $p_T^{\rm jet} > 30$ GeV

| Targeted | Type | $N_{\rm lepton}$ | $m_T$ | $N_{\rm jet}$ | $m_{T,\,\min}^{b\text{-jets}}$ | $M_J^{\Sigma}$ | $E_T^{\rm miss}$ | $m_{\rm eff}$ |
|---|---|---|---|---|---|---|---|---|
| High-$m_{\rm eff}$ (HH) (Large $\Delta m$) | SR-1L | $\geq 1$ | $> 150$ | $\geq 6$ | $> 120$ | $> 200$ | $> 500$ | $> 2300$ |
| | CR | $\geq 1$ | $< 150$ | $\geq 6$ | $> 60$ | $> 150$ | $> 300$ | $> 2100$ |
| | VR-1L | $\geq 1$ | $> 150$ | $\geq 6$ | $< 140$ if $m_{\rm eff} > 2300$ | $-$ | $< 500$ | $> 2100$ |
| Intermediate-$m_{\rm eff}$ (HI) (Intermediate $\Delta m$) | SR-1L | $\geq 1$ | $> 150$ | $\geq 8$ | $> 140$ | $> 150$ | $> 300$ | $[1800, 2300]$ |
| | CR | $\geq 1$ | $< 150$ | $\geq 8$ | $> 60$ | $> 150$ | $> 200$ | $[1700, 2100]$ |
| | VR-1L | $\geq 1$ | $> 150$ | $\geq 8$ | $< 140$ if $E_T^{\rm miss} > 300$ | $-$ | $< 300$ if $m_{T,\,\min}^{b\text{-jets}} > 140$ | $[1600, 2100]$ |
| Low-$m_{\rm eff}$ (HL) (Small $\Delta m$) | SR-1L | $\geq 1$ | $> 150$ | $\geq 8$ | $> 140$ | $-$ | $> 300$ | $[900, 1800]$ |
| | CR | $\geq 1$ | $< 150$ | $\geq 8$ | $> 130$ | $-$ | $> 250$ | $[900, 1700]$ |
| | VR-1L | $\geq 1$ | $> 150$ | $\geq 8$ | $< 140$ | $-$ | $> 225$ | $[900, 1650]$ |

**Table 2.** Definition of the high-$N_{\rm jet}$ SRs, CRs and VRs of the multi-bin analysis.

**Intermediate-$N_\text{jet}$ regions**

Criteria common to all regions: $N_{b\text{-jets}} \geq 3$, $p_T^\text{jet} > 30$ GeV

| Targeted | Type | $N_\text{lepton}$ | $m_T$ | $N_\text{jet}$ | $m_{T,\,\min}^{b\text{-jets}}$ | $M_J^\Sigma$ | $E_T^\text{miss}$ | $m_\text{eff}$ |
|---|---|---|---|---|---|---|---|---|
| Intermediate-$m_\text{eff}$ | SR-1L | $\geq 1$ | $> 150$ | [6,7] | $> 140$ | $> 150$ | $> 300$ | [1600,2300] |
| (II) | CR | $\geq 1$ | $< 150$ | [6,7] | $> 110$ | $> 150$ | $> 200$ | [1600,2100] |
| (Intermediate $\Delta m$) | VR-1L | $\geq 1$ | $> 150$ | [6,7] | $< 140$ | $-$ | $> 225$ | [1450,2000] |
| Low-$m_\text{eff}$ | SR-1L | $\geq 1$ | $> 150$ | [6,7] | $> 140$ | $-$ | $> 300$ | [800,1600] |
| (IL) | CR | $\geq 1$ | $< 150$ | [6,7] | $> 130$ | $-$ | $> 300$ | [800,1600] |
| (Low $\Delta m$) | VR-1L | $\geq 1$ | $> 150$ | [6,7] | $< 140$ | $-$ | $> 300$ | [800,1450] |

**Table 3.** Definition of the intermediate-$N_\text{jet}$ SRs, CRs and VRs of the multi-bin analysis.

## 6.5.3. Systematic Uncertainties

The systematic uncertainties on the estimation of the backgrounds come from the extrapolation of the $t\bar{t}$ normalization from the CRs to the SRs, as well as from MC estimations of the minor backgrounds. The total systematic uncertainties vary from 20% to 80%; they are shown in Figure 11.
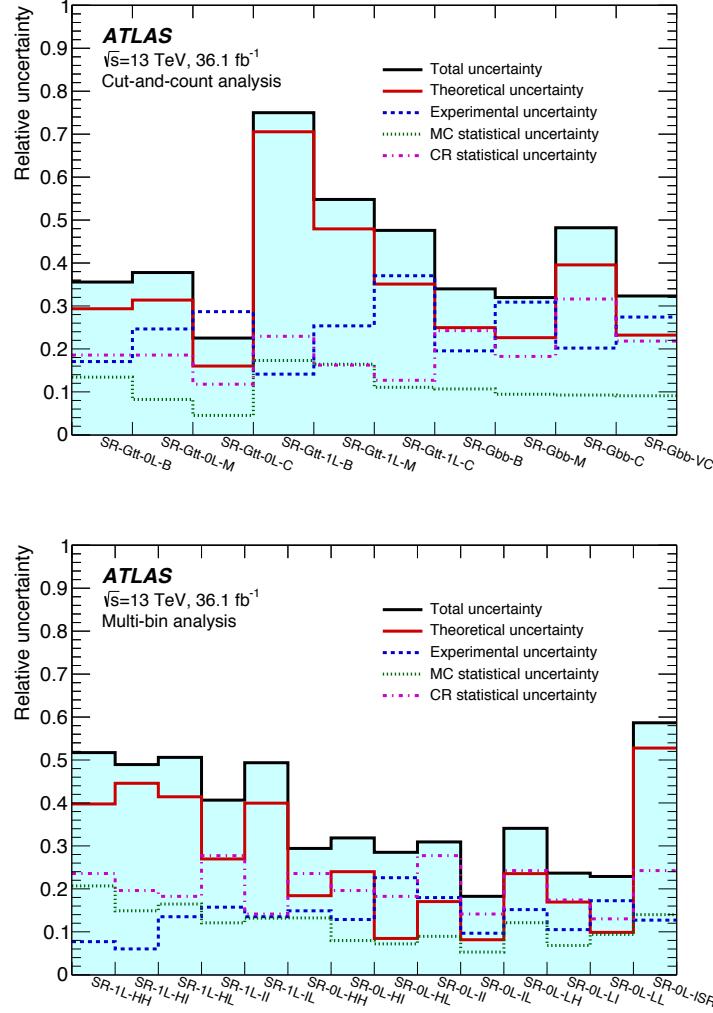


**Fig. 11.** Systematic uncertainties for the cut-and-count analysis (top) and multi-bin analysis (bottom).

As $t\bar{t}$ normalization takes place in the CRs, uncertainties due to $t\bar{t}$ simulation only make contributions to the extrapolation from the CRs to the SRs and the VRs.

Among the detector-related uncertainties, the largest contributions come from jet energy scale (JES), jet energy resolution (JER), and the $b$-tagging efficiencies and mistagging rates. The JES uncertainties are derived from $\sqrt{s} = 13$ TeV data and simulations, whereas the

JER uncertainties are derived from 8 TeV data using simulations [**88**]. These uncertainties are measured for small $R$-jets and are propagated to re-clustered large $R$-jets. The jet mass scale and resolution uncertainties make a negligible contribution to re-clustered jet mass. JES uncertainties contribute between 4% and 35% to the estimation of the backgrounds, and JER uncertainties up to 26%.

The $b$-tagging and mistagging rate uncertainties contribute between 3% to 24% to the the estimation of the backgrounds. Lepton reconstructions and energy measurement make a negligible contribution.

The theoretical uncertainty on the $t\bar{t}$ background is the sum in quadrature of the following sources:

- Hadronization and parton showering model uncertainties are estimated using a POWHEG sample, showered by HERWIG++ v2.7.1 with the UEEE5 underlying-event, by a comparison with the nominal sample generated with POWHEG and showered with PYTHIA.
- Uncertainties due to the simulation of initial- and final-state radiation are estimated using POWHEG samples, showered with PYTHIA v6.428. The renormalization and factorization scales are set to twice and then half of their nominal values, so that radiation in the events is increased and decreased respectively. The uncertainty in each case is taken to be the difference between the obtained value and the nominal value.
- The uncertainty due to the choice of matrix-element event generator is estimated by comparing background predictions in MADGRAPH5_aMC@NLO and POWHEG samples, both showered with HERWIG++ v2.7.1.

An additional uncertainty is assigned to $t\bar{t}$ heavy-flavour jets. It was found from simulation studies that each set of SR, CR, and VR had the same fractions of these events. Thus the uncertainties are similar among the regions, and $t\bar{t}$ normalization based on the predictions in the CR largely cancel out these uncertainties. The residual uncertainty is taken as the difference between the $t\bar{t}$ nominal prediction and that obtained after varying the cross-section of $t\bar{t}$ events with additional heavy-flavor jets by 30% [**89**]. It contributes up to 8% to the total $t\bar{t}$ background uncertainty (background expectation ranges from 5% to 76% in the regions). The statistical uncertainty of the CRs is included in the systematic uncertainties and varies from 10% to 30%.

The single-top simulation suffers from interference between $t\bar{t}$ and $Wt$ processes. This uncertainty is estimated using $WWbb$ events, generated using MADGRAPH5_aMC@NLO, where a comparison is made with the sum of $t\bar{t}$ and $Wt$ processes. Also, uncertainties due to initial- and final-state radiation are estimated using PYTHIA v6.428, as in the case of $t\bar{t}$ uncertainties. Moreover, an additional 5% uncertainty is included in the cross-section of

single-top processes [**89**]. The total uncertainty for the single-top process contributes to a change of the overall background of up to 11% in the regions.

Uncertainties in the $W/Z$+jets backgrounds are estimated by varying various parameter scales, and make a contribution up to 50% in the regions.

Finally, the uncertainties in the cross-sections of signal processes are determined from an envelope of different cross-section predictions. A systematic uncertainty is also assigned to the kinematic correction described in Section 6.4.2; the total size of the correction is used as an uncertainty.

## 6.5.4. Results

In each SR, the expected SM background is determined with a profile likelihood fit [**90**] implemented in the HistFitter framework [**91**], which will be referred to as a background-only fit. The fit uses as inputs the number of events predicted by simulation in each region, plus the number of events predicted in the associated CR. It is constrained by the number of observed events in the CR and outputs a $t\bar{t}$ normalization factor that is applied to the number of $t\bar{t}$ events predicted by simulation in the SR. The number of observed and predicted events are modelled as Poisson distributions, and the systematic uncertainties as Gaussian distributions having widths that correspond to the sizes of the uncertainties, treated as correlated where appropriate. The likelihood function is the product of the various distributions.

Figure 12 shows the values of the normalization factors resulting from the fit, the expected numbers of background events and observed data in all the CRs for the cut-and-count and multi-bin analyses. They can be seen to be mostly consistent with one within uncertainties. The normalization factors for the hadronic Gtt channel and Gbb, not discussed in detail in this chapter, are also shown.

Figure 13 shows the results of the fit to the CRs, extrapolated to the VRs for the cut-and-count and multi-bin analyses. The background predicted by the fit is compared to the data in the upper panel. The figure also shows in the lower panel the pull, which is the difference between the observed number of events and the predicted background divided by the total uncertainty. None of the pulls exceeds $2\sigma$ and thus no significant mis-modelling is indicated.

Since the agreements in the VRs are satisfactory, the SRs have been unblinded. Figure 14 shows the SRs for the cut-and-count and multi-bin analyses. The pull is shown in the lower panel. No significant excess relative to the predicted background is seen. The largest excess is observed in `SR-OL-HH` that belongs to the multi-bin analysis, showing a $2.3\sigma$ local excess [6]. The background is dominated by $t\bar{t}$ in all SRs.

---

[6]This excess was followed up in a subsequent analysis at 80 fb$^{-1}$ but no longer appeared.

Table 4 shows the observed number of events and predicted number of background events from the background fit for the cut-and-count analysis. In general, the central value of the fitted background is larger than the MC-only prediction. This is in part due to an underestimation of the cross-section of $t\bar{t}+ \geq 1b$ and $t\bar{t}+ \geq 1c$ processes in the simulation.
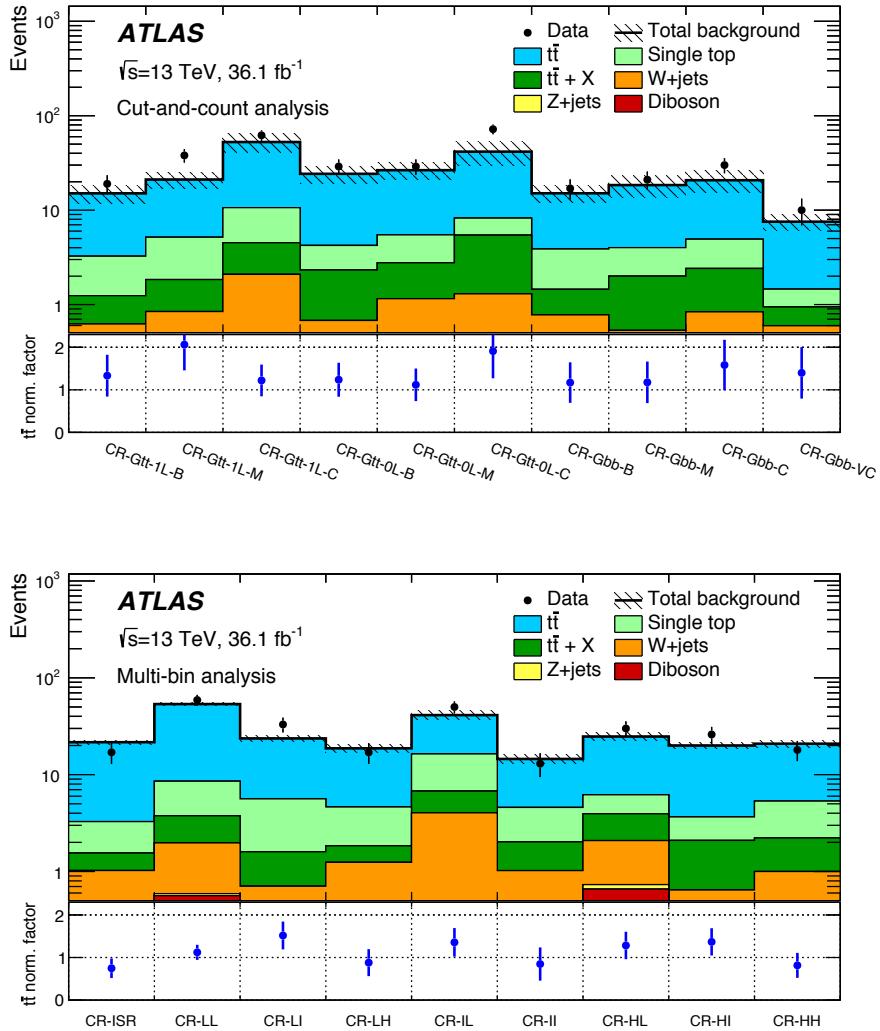


**Fig. 12.** Pre-fit events in CRs and the related $t\bar{t}$ normalization factors for the cut-and-count analysis (top) and multi-bin analysis (bottom). The upper panel shows the observed number of events and the predicted background before the fit. The background $t\bar{t}+X$ include $t\bar{t}W/Z$, $t\bar{t}H$, and $t\bar{t}t\bar{t}$ events. The multijet background is negligible. All uncertainties described in Section 6.5.3 are included in the uncertainty band. The $t\bar{t}$ normalization is obtained from the fit and is shown in the bottom panel.
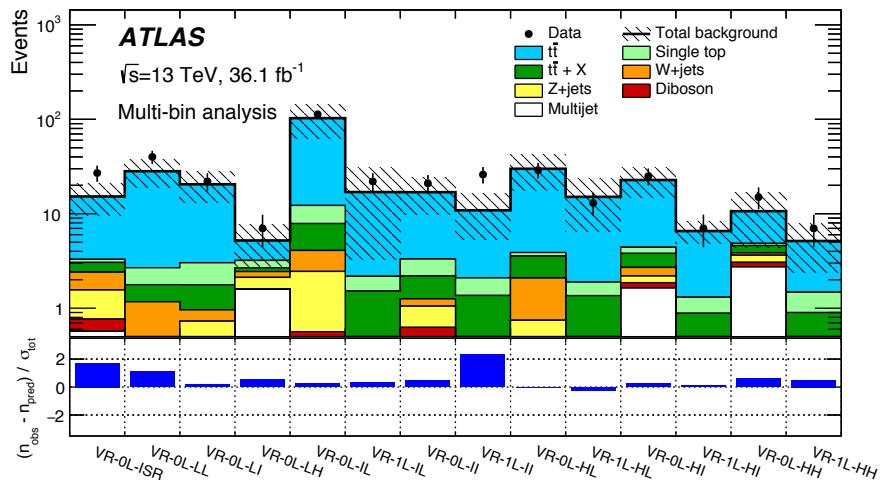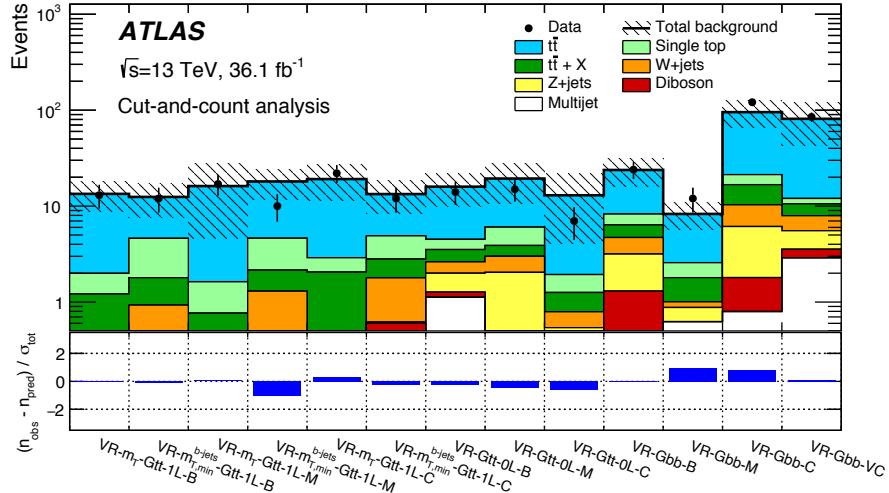
**Fig. 13.** Background fit extrapolated to the VRs of the cut-and-count analysis (top) and the multi-bin analysis (bottom). The $t\bar{t}$ normalization is obtained from the fit to the CRs shown in Figure 12. The upper panel shows the observed number of events and the predicted background. The background $t\bar{t} + X$ include $t\bar{t}W/Z$, $t\bar{t}H$, and $t\bar{t}t\bar{t}$ events. The lower panel shows the pulls in each VR. The last row displays the total background prediction when the $t\bar{t}$ normalization is obtained from a theoretical calculation [**92**].

|                      | SR-Gtt-1L |   |   |
|----------------------|-----------|---|---|
| Targeted kinematics  | B | M | C |
| Observed events      | 0 | 1 | 2 |
| Fitted background    | $0.5 \pm 0.4$ | $0.7 \pm 0.4$ | $2.1 \pm 1.0$ |
| $t\bar{t}$           | $0.4 \pm 0.4$ | $0.5 \pm 0.4$ | $1.2 \pm 0.8$ |
| Single-top           | $0.04 \pm 0.05$ | $0.03 \pm 0.06$ | $0.35 \pm 0.28$ |
| $t\bar{t} + X$       | $0.08 \pm 0.05$ | $0.09 \pm 0.06$ | $0.50 \pm 0.28$ |
| $Z$+jets             | $0.049 \pm 0.023$ | $0.050 \pm 0.023$ | $< 0.01$ |
| $W$+jets             | $< 0.01$ | $< 0.01$ | $0.024 \pm 0.026$ |
| Diboson              | $< 0.01$ | $< 0.01$ | $< 0.01$ |
| MC-only background   | 0.43 | 0.45 | 1.9 |

**Table 4.** Results of the background-only fit extrapolated to the Gtt 1-lepton SRs in the cut-and-count analysis, for the total background prediction and breakdown of the main background sources. The uncertainties shown include all systematic uncertainties. The data in the SRs are not included in the fit. The background $t\bar{t} + X$ includes $t\bar{t}W/Z$, $t\bar{t}H$, and $t\bar{t}t\bar{t}$ events. The row MC-only background provides the total background prediction when the $t\bar{t}$ normalization is obtained from a theoretical calculation [92].
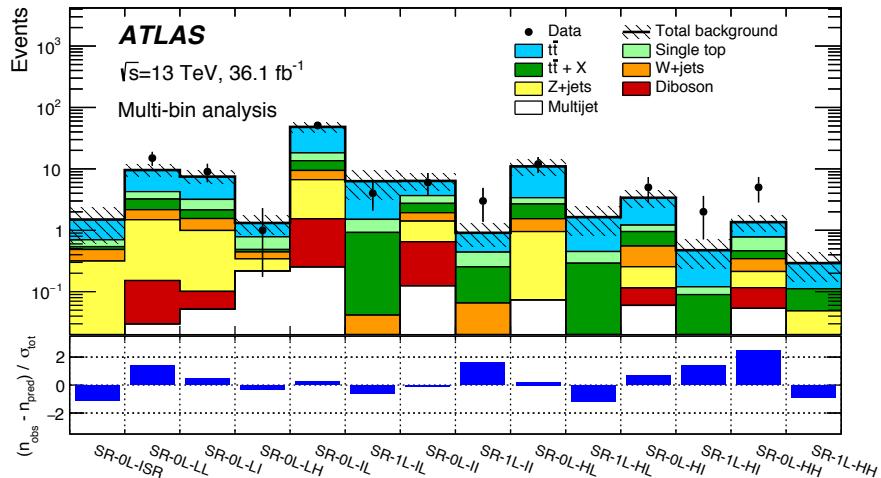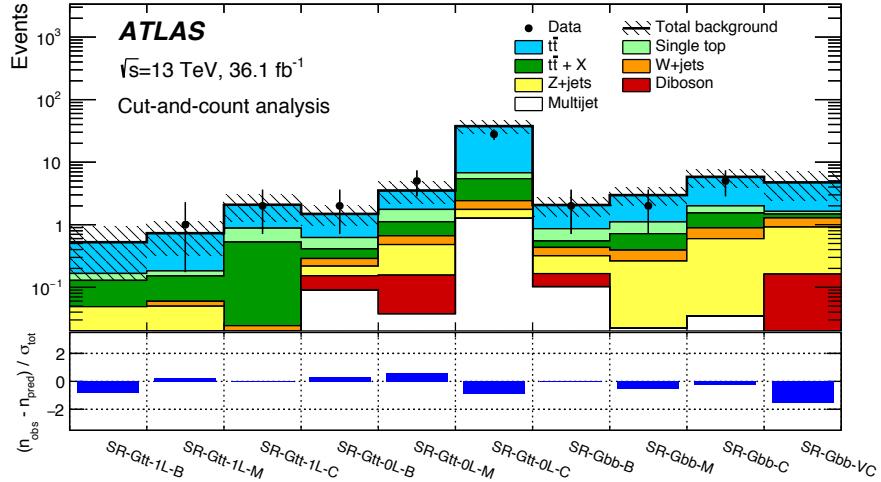
**Fig. 14.** Background-only fits extrapolated to the SRs for the cut-and-count analysis (top) and multi-bin analysis (bottom). The data in the SRs are not included in the fit. In each figure the upper panel shows the observed number of events and the predicted background yield. All uncertainties discussed in Section 6.5.3 are included. The background $t\bar{t} + X$ includes $t\bar{t}W/Z$, $t\bar{t}H$, and $t\bar{t}t\bar{t}$ events. The lower panel shows the pulls in each SR.

## 6.6. Interpretation

No discovery can be claimed and one-sided upper limits at 95% confidence level (CL) are derived from the data. Section 6.6.1 discusses model-independent exclusion limits and Section 6.6.1 discusses model-dependent exclusion limits.

### 6.6.1. Model-independent Exclusion Limits

For each SR, model-independent limits on the number of beyond-the-SM events are derived. Pseudoexperiments in the $CL_s$ prescription [**93**] are employed, neglecting possible signal contamination in the CR. Only the single-bin regions in the cut-and-count are used. Table 5 shows the results. It includes the visible beyond the Standard Model cross-section ($\sigma_{vis}^{95}$) obtained by dividing the observed upper limits on the number of beyond the Standard Model events with the integrated luminosity, as well as the $p_0$-values, which represent the probability that the SM background alone would fluctuate to the observed number of events or higher.

| Signal channel | $p_0$ (Z) | $\sigma_{vis}^{95}$ [fb] | $S_{obs}^{95}$ | $S_{exp}^{95}$ |
|---|---|---|---|---|
| SR-Gtt-1L-B | 0.50 (0.00) | 0.08 | 3.0 | $3.0^{+1.0}_{-0.0}$ |
| SR-Gtt-1L-M | 0.34 (0.42) | 0.11 | 3.9 | $3.6^{+1.1}_{-0.4}$ |
| SR-Gtt-1L-C | 0.50 (0.00) | 0.13 | 4.8 | $4.7^{+1.8}_{-0.9}$ |

**Table 5.** The $p_0$-values and $Z$ (the number of equivalent Gaussian standard deviations), the 95% CL upper limits on the visible cross-section ($\sigma_{vis}^{95}$), and the observed and expected 95% CL upper limits on the number of BSM events ($S_{obs}^{95}$ and $S_{exp}^{95}$). The maximum allowed $p_0$-value is truncated at 0.5.

### 6.6.2. Model-dependent Exclusion Limits

Multi-bin analysis regions from the leptonic and hadronic channels are statistically combined, using the $CL_s$ prescription in the asymptotic approximation [**90**], to set model-dependent upper limits. The expected and observed limits are found to be compatible with the $CL_s$ calculated from pseudoexperiments.

Figure 15 shows the 95% CL observed and expected exclusion limits in the neutralino and the gluino mass plane. The $\pm 1\sigma_{theory}^{SUSY}$ limit lines are obtained by changing the SUSY cross-section by one standard deviation up and down (Section 6.2). The yellow band around the expected limit shows the $\pm 1\sigma$ uncertainty, including all statistical and systematatic uncertainties, except the theoretical uncertainties in the SUSY cross-section. The current search shows an improvement, compared to the previous result performed at $\sqrt{s} = 13$ TeV and 3.2 fb$^{-1}$ integrated luminosity [**94**], of 450 GeV in gluino mass sensitivity, assuming massless neutralino. Gluinos having masses below 1.97 TeV are excluded at 95% CL for neutralino masses lower than 300 GeV. The red line shows the observed limit; at high gluino mass it is weaker than the expected limits, due to a mild excess observed in the region SR-1L-HI (and a mild excess in a region in the hadronic channel) of the multi-bin analysis.
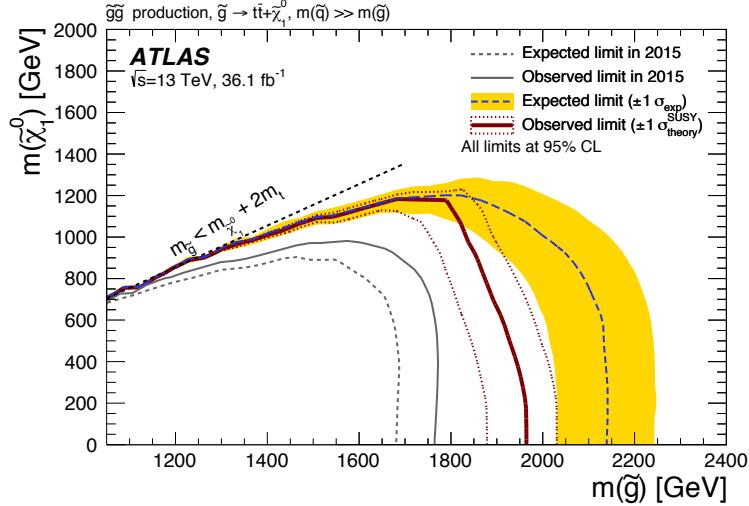
**Fig. 15.** Exclusion limits in the multi-bin analysis. The dashed line shows the 95% CL expected limit, and the solid bold line the 95% CL observed limit. The shaded bands around the expected limits show the impact of experimental and background uncertainties. The dotted lines show the impact on the observed limit of the variation of the nominal signal cross-section by $\pm 1\sigma$ of its theoretical uncertainty. Also shown are the 95% CL expected and observed limits from the ATLAS search based on 2015 data [**94**].

## 6.7. Conclusions

The analysis in this chapter presents a search for pair-produced gluinos, which is highly motivated at ATLAS as gluinos are expected to have a mass around the TeV scale by naturalness, as well as a high production cross section at the LHC. The data used were collected at the LHC in the 2015-2016 data taking period, at $\sqrt{s} = 13$ TeV and correspond to an integrated luminosity of 36.1 fb$^{-1}$. The signal model is Gtt, of which the leptonic final state involves at least one lepton, large $E_T^{\mathrm{miss}}$, and multiple jets among which at least three must be $b$-jets. Several signal regions are defined to accommodate several ranges of mass differences between the gluino and the neutralino. Two analysis strategies are followed, the cut-and-count strategy in which possibly overlapping signal regions are optimized for discovery, and the multi-bin strategy in which non-overlapping signal regions are optimized for model-dependent exclusions. The dominant source of background is $t\bar{t}$+jets, whose normalization factors are obtained in dedicated control regions. No excess relative to the Standard Model background can be claimed. Model-independent limits are set on the visible cross-section for new physics processes. The multi-bin regions in the leptonic channel are combined with those in the hadronic channel to set model-dependent limits on gluino and neutralino masses. For neutralino masses below approximately 300 GeV, gluino masses of less than 1.97 TeV are excluded at the 95% CL, which is an improvement compared to the exclusion limits obtained with the 2015 dataset alone.

# Chapter 7

## IN-JET ELECTRON IDENTIFICATION EFFICIENCIES

In early 2015 the LHC restarted after two years of shutdown, beginning what is referred to as Run 2. The new centre-of-mass energy was 13 TeV, in place of the previous 8 TeV. The higher energy opens up unexplored parameter space and allows further probe of supersymmetry (SUSY) and other beyond-the-Standard-Model processes [**60, 95, 96, 97**]. At ATLAS, many SUSY searches involve supersymmetric particles that decay into the Standard Model top quarks and we expect, with higher centre-of-mass energy, sensitivity to more massive supersymmetric particles, which would in turn decay to high $p_T$ top quarks. Since the top quarks also decay — essentially all the time — into a $W$ boson and a $b$ quark, we in turn expect boosted decay topology, in other words the daughter particles of the top quarks, which include the daughter particles of the $W$ boson and the $b$ quark, tend to stay close to each other (Figure 1).

This chapter describes the work to measure the identification efficiencies for electrons that are found inside $\Delta R = 0.4$ of high $p_T$ jets , which will also be called in-jet electrons, using $t\bar{t}$ events. Prior to the work in this chapter, there was no attempt to measure the identification efficiencies for in-jet electrons in a $t\bar{t}$ topology. The chapter will be organized as follows. In section 7.1 we motivate the need for the measurement of the identification efficiencies for in-jet electrons. Section 7.2 describes the method used to perform the measurements and presents the measured efficiencies. Section 7.3 presents some conclusions.

The data used for this chapter were collected in the period 2015-2016 at 13 TeV center-of-mass and corresponded to an integrated luminosity of 36.1 fb$^{-1}$.

## 7.1. Motivation

Prior to Run 2, ATLAS centre-of-mass energy 7-8 GeV allows limited sensitivity to high mass resonances. Because many beyond-Standard-Model particles are predicted to decay into

the Standard Model top quarks, the limited sensitivity reduces the chance in which we could expect boosted top quark decays. Such decays, however, are expected to become significant as the centre-of-mass of the LHC reached 13 TeV starting from Run 2. In a boosted top quark decay scenario, the produced particles, which in this case are the daughters of the $W$ and the $b$ quark that come from the top quark, are found close to each other [98, 99, 100]. Figure 2 shows the angular distance $\Delta R$ (Formula 3.2.1) between the $W$'s and the $b$-quarks as a function of the top $p_T$, in the context of a hypothetical particle $Z'$ with mass $m_{Z'} = 1.6$ TeV [100] that decays into a $t\bar{t}$ pair. Also shown in the same figure is the separation between the light quarks of the subsequent hadronic decay of the $W$ boson. As can be seen, the angular distance decreases as the top quark $p_T$ increases, and at high top quark $p_T$ a non-negligible fraction of the opening angles becomes very small.
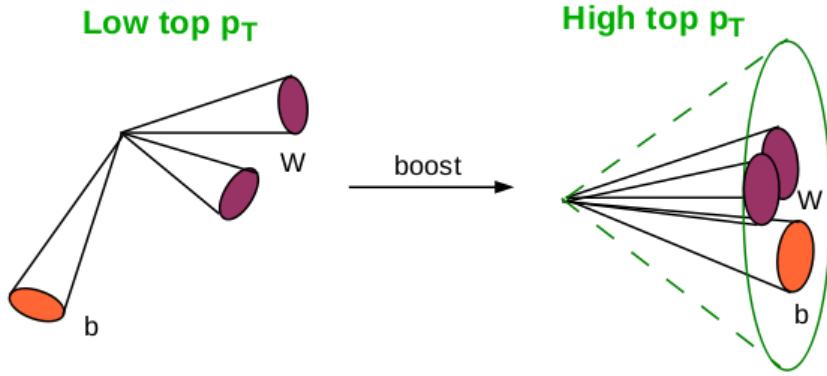


**Fig. 1.** An illustration of low $p_T$ top quark decay (left) and boosted top decay (right) of a high $p_T$ top quark. In the case of high $p_T$ top quark decay the daughter particles of the top quark, which include the daughter particles of the $W$ and the $b$ quark, are expected to be found close to each other [101].

Leptonic boosted top quark decay is also an important channel in searches for beyond-Standard-Model particles that decay into the Standard-Model top quarks. Table 1 shows a measurement of the fraction of in-jet electrons[1] over signal electrons as a function of the top quark $p_T$, at truth-level. The measurement used Powheg+Pythia $t\bar{t}$ events simulated at 13 TeV centre-of-mass energy (Chapter 6, Section 6.2), where dilepton events consisting of a muon and an electron were selected. The selections made use of the $p_T$-dependent overlap removal

$$\Delta R < \min\left(0.4,\ 0.04 + 10\ \text{GeV}/p_T\right), \tag{7.1.1}$$

where the overlap removal is required to keep the overlapping $b$-jets (Chapter 6, Section 6.3). As is shown, more and more electrons are found inside jets as the top quark $p_T$ increases.

---

[1]The jets in which the electrons are found refer to signal jets reconstructed using the anti-$k_t$ jet algorithm [71, 72, 73] with a radius parameter $\Delta R = 0.4$.

The number of in-jet electrons becomes quite significant from 500 GeV, being approximately 25% there and reaching nearly 40% at 650 GeV. If the top quark $p_T$ is allowed to go up to 1 TeV, the figure is 64%. This result supports the fact that different ATLAS analyses searching for heavy beyond-Standard-Model particles decaying into lighter sparticles, such as the gluinos and stops that decay into neutralinos, in which the final state involve the Standard Model top quarks, will be able to increase signal acceptances considerably if in-jet electrons were selected [60, 95].

This chapter develops a method and performs the initial measurements for the identification efficiencies of electrons found inside $\Delta R = 0.4$ of jets. The measurements for electrons outside jets are done by the ATLAS Egamma group [43, 102].
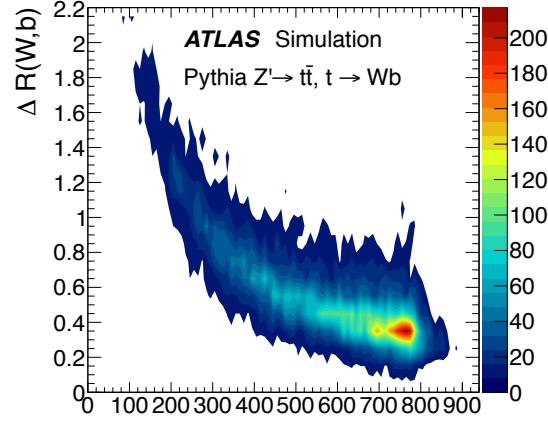
**(a)** $t \rightarrow Wb$
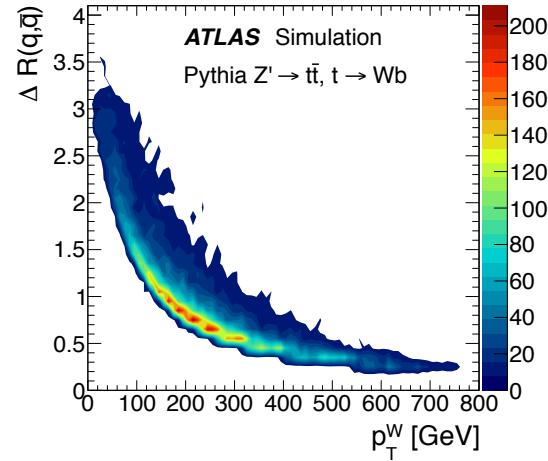


**(b)** $W \rightarrow q\bar{q}$

**Fig. 2.** (2a) The angular distance $\Delta R$ between the $W$'s and the $b$ quarks as a function of the top quark $p_T$ simulated PYTHIA [**103**], in the context of a hypothetical particle $Z'$ ($m_{Z'} = 1.6$ TeV) that decays into a $t\bar{t}$ pair. At high top quark $p_T$ a non-negligible fraction of the distances is seen to be very small. (2b) The angular distance between two light quarks from $t \rightarrow Wb$ decay as a function of the $p_T$ of the $W$ boson [**100**].

## 7.2. Method

The method that is used to measure the identification efficiencies for in-jet electrons is discussed in detail in Section 7.2.1, 7.2.2, and 7.2.3. Background estimations is described in Section 7.2.4.

| Top quark $p_T$ (GeV) | Fraction |
| --- | --- |
| $\leq 300$ | 8.4% |
| $\leq 425$ | 17.2% |
| $\leq 500$ | 24.0% |
| $\leq 650$ | 39.0% |
| $\leq 750$ | 49.0% |
| $\leq 800$ | 53.0% |
| $\leq 900$ | 59.0% |
| $\leq 1000$ | 64.0% |

**Table 1.** The fraction of in-jet electrons over the number of signal electrons, both at truth-level, as a function of the top quark $p_T$. The fraction increases and becomes very significant at high top quark $p_T$.

### 7.2.1. Boosted Dilepton $e\mu$ Events

In order to measure the identification efficiencies for in-jet electrons, a sample of reconstructed electrons (Chapter 6, Section 6.3) inside high-$p_T$ jets was obtained by selecting boosted $t\bar{t}$ dilepton ($e\mu$) events. This is expected to result not only in a pure $t\bar{t}$ sample, but also in a topology close to that of many SUSY and other beyond-Standard-Model searches that include boosted top quarks in the final state. In contrast, the standard method for measuring electron identification efficiencies, the tag-and-probe method supported by the Egamma group at ATLAS [102], makes use of $Z \to e^+e^-$ events. Even though a clean sample of electrons may be obtained in a relatively straightforward way by selecting events around the $Z$ mass peak, we expect, if electrons inside high $p_T$ jets are required, the sample to be non-representative of events with a boosted topology and limited in statistics.

Thus, a sample of electrons was obtained by selecting a hard muon and a reconstructed electron candidate with only a $p_T$ requirement applied, which will also be referred to below simply as reconstructed electrons. The efficiency at a particular identification operating point (Section 4.2.2) is defined by the ratio

$$\text{ID efficiency} = \frac{\text{The number of identified electrons}}{\text{The number of reconstructed electrons}}.$$

Both the numerator and the denominator are contaminated with background electrons which require a careful estimate (Section 7.2.4), particularly because background electrons are expected to reside primarily inside jets.

## 7.2.2. Data and Monte Carlo Samples

The data used for this chapter were collected in the period 2015-2016 and corresponds to an integrated luminosity of 36.1 fb$^{-1}$. The following simulation samples (Chapter 6, Section 6.2), at 13 TeV centre-of-mass energy, are used:

- $t\bar{t}$ events from the Powheg+Pythia generator. As a hard muon will be required in the sample in which the identification efficiencies are measured (Section 7.2.3), these events naturally partition into either a dileptonic set ($e\mu$) when truth-level electrons are present inside high-$p_T$ jets, or a semileptonic set otherwise. The latter, with jets from the fully hadronic decay of one of the top quarks constituting a source of background electrons, is expected to be the dominant background.
- $W$+jets, which will be used as a background. As the $W$ boson may produce a hard muon, the presence of jets makes these events a source of background events to signal dilepton $e\mu$ $t\bar{t}$ events.
- Single top events, which include the $Wt$ production as well as the $s$-channel and $t$-channel productions. The $Wt$ production is treated as a source of signal electrons, since it contains a pair of $W$ bosons that can decay to a prompt $e\mu$ pair, whereas the remaining two productions each contain only one $W$ boson and as a result cannot produce a prompt $e\mu$ pair.

## 7.2.3. Signal Region

The kinematic region in which the measurement of the identification efficiencies is performed is called the signal region. It is defined after the following preliminary selections, which are called the pre-selection cuts and aimed at isolating dilepton $e\mu$ $t\bar{t}$ events, are applied.

Pre-selection.
- One primary vertex
- Muon trigger. Two triggers were used for the periods 2015 and 2016. For the period 2015, isolated muons are required to pass triggers with an online threshold of $p_T > 26$ GeV, while for non-isolated muons the online threshold is $p_T > 40$ GeV. For the period 2016, isolated muons are required to pass triggers with an online threshold of $p_T > 26$ GeV, while for non-isolated muons the online threshold is $p_T > 45$ GeV.
- $p_T$-dependent overlap removal, where the overlapping $b$-jets are kept (Formula 7.1.1), allowing the possibility of electrons found inside $b$-tagged jets due to boosted $t\bar{t}$ decays.
- Events with bad or cosmic muons are removed. Highly energetic jets could reach the muon spectrometer and create hits in the latter, or jet tracks in the inner detector

could be erroneously matched to muon spectrometer segments, both of which cases are sources of bad muons. Events with these muon candidates, along with those having muons from cosmic rays, are rejected.

- Exactly one identified muon and $\geq 1$ reconstructed electrons inside jets are required for each event, where

  - The muon is required to have $p_T > 30$ GeV, $d_0/\sigma(d_0) < 3.0$, and $z_0 < 0.5$ in terms of the transverse impact parameter and the longitudinal impact parameter. It must also have ptvarcone30$/p_T < 0.06$, where ptvarcone30 is defined as the scalar sum of the momenta of the tracks with $p_T > 1$ GeV in the cone with $\Delta R < \min(10 \text{ GeV}/p_T, 0.3)$, and must be a muon that has been triggered.
  - The electrons must have $p_T \geq 30$ GeV, which is a common cut in most analyses where in-jet electrons are used, and must overlap within $\Delta R < 0.4$ with some jets. There could be more than one electron present in the event, however the leading $p_T$ electron will be used,

- $\geq 1$ $b$-tagged jet, instead of exactly 2 $b$-tagged jets as is usually expected in $t\bar{t}$ events, since we are selecting events with electrons inside jets and the $b$-tagging efficiency may suffer because the tracks of the electron, which is expected to originate from the interaction point, may confuse the $b$-tagging algorithm.

These cuts result in a set of 3183 events with one hard muon and at least one electron candidate found inside some jet. In the following, we discuss several variables that have been found to be discriminating, along with their distribution plots. Simulation shows an expected 814 dilepton events and 179 single top $Wt$ production events. On the other hand, the prominent source of background comes from semileptonic events, predicted to be 2011, whereas $W$+jets and single top $s$-channel and $t$-channel constitute two small sources of background, predicted to be 316 and 19 respectively.

- The mass of the large radius jet that overlaps with the probe electron, denoted $m_{\text{rjet}}^{\text{el}}$ and is shown in Figure 3. The large radius jet is reclustered from the small radius jets present in the events (Chapter 6, Section 6.3), and accordingly in semileptonic events it is expected to be more massive, as it picks up the masses of the jets from the hadronic decay of one of the top quarks. In dileptonic events, on the other hand, there are fewer jets due to leptonic decays of both of the top quarks, and in addition the neutrino that accompanies the electron may reduce the visible mass of the reconstructed large radius jet. As is shown in the figure, the higher mass region is dominated by background events.
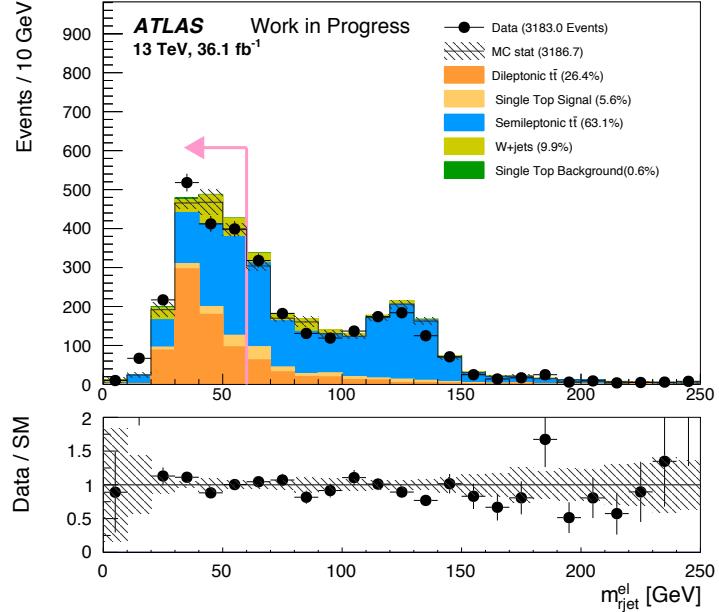
**Fig. 3.** The distribution of $m_{\text{rjet}}^{\text{el}}$ after the preselection requirements. The ratio of data to background prediction is also shown below the figure. The signal includes dileptonic $t\bar{t}$ (orange) and single top $Wt$ production (yellow), and the background includes semileptonic $t\bar{t}$ (blue), $W$+jets (teal), and single top $s$-channel and $t$-channel productions (green).

- The number of jets, which is denoted $N_{\text{jet}}$ and is shown in Figure 4. Three jets are expected from a fully hadronic decaying top quark, as compared to only one jet from a semileptonic decay. As a result, semileptonic events, in which one top quark decays hadronically and one decays semileptonically, are expected to have a greater number of jets than dileptonic events, where both top quarks decay semileptonically. Figure 4 shows that, on average, the number of jets is higher in semileptonic ttbar than dileptonic ttbar events.
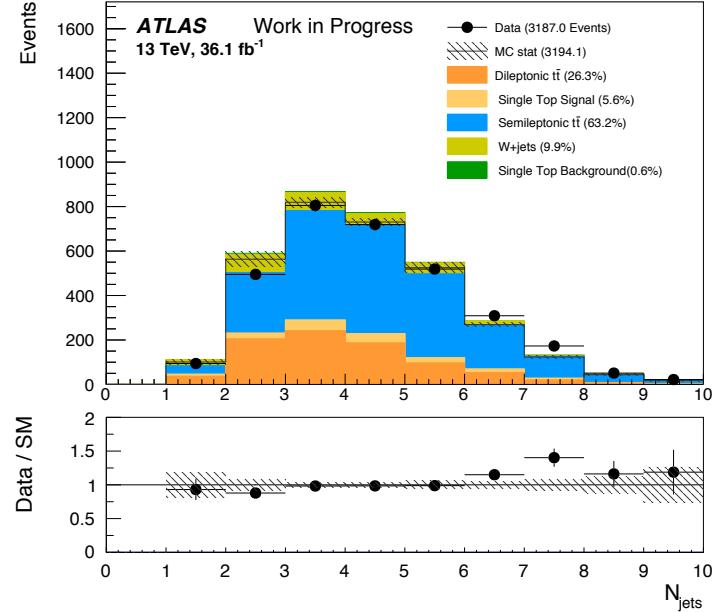
**Fig. 4.** The distribution of $N_{jet}$ after the preselection requirements. The ratio of data to background prediction is also shown below the figure. The signal includes dileptonic $t\bar{t}$ (orange) and single top $Wt$ production (yellow), and the background includes semileptonic $t\bar{t}$ (blue), $W$+jets (teal), and single top $s$-channel and $t$-channel productions (green).

- The sum of the transverse momenta of all jets, denoted $H_T$ and is shown in Figure 5. As above, a larger number of jets is expected in semileptonic events due to the fully hadronic decay of one of the top quarks, and in dileptonic events fewer jets are expected because of leptonic decays of both of the top quarks. Consequently a sum over all transverse momenta of the jets is expected to lead to a discriminating distribution. As can be seen in Figure 5, $H_T$ is a good variable to discriminate semileptonic from dileptonic ttbar events.
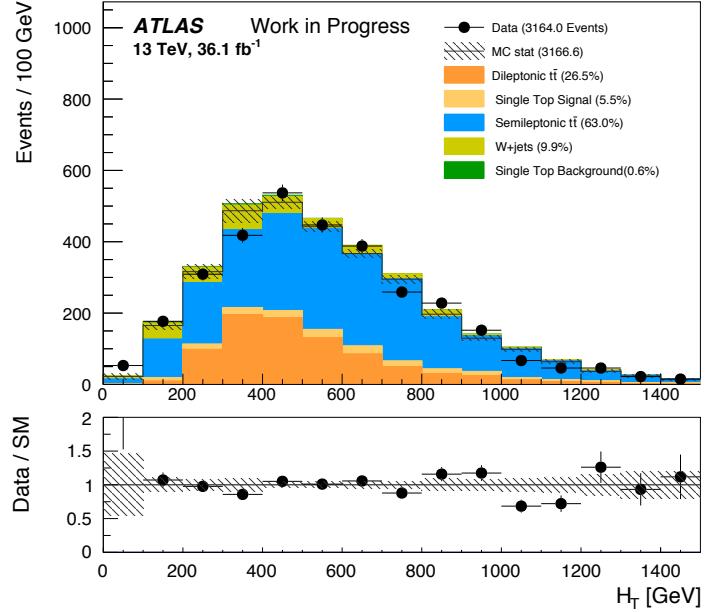
**Fig. 5.** The distribution of $H_T$ after the preselection requirements. The ratio of data to background prediction is also shown below the figure. The signal includes dileptonic $t\bar{t}$ (orange) and single top $Wt$ production (yellow), and the background includes semileptonic $t\bar{t}$ (blue), $W$+jets (teal), and single top $s$-channel and $t$-channel productions (green).

- The transverse momenta of the jet overlapping with the probe electron, which is denoted $p_T{}^{\text{jet}}$ and is shown in Figure 6. This variable allows the removal of low $p_T$ jets overlapping with background electrons.
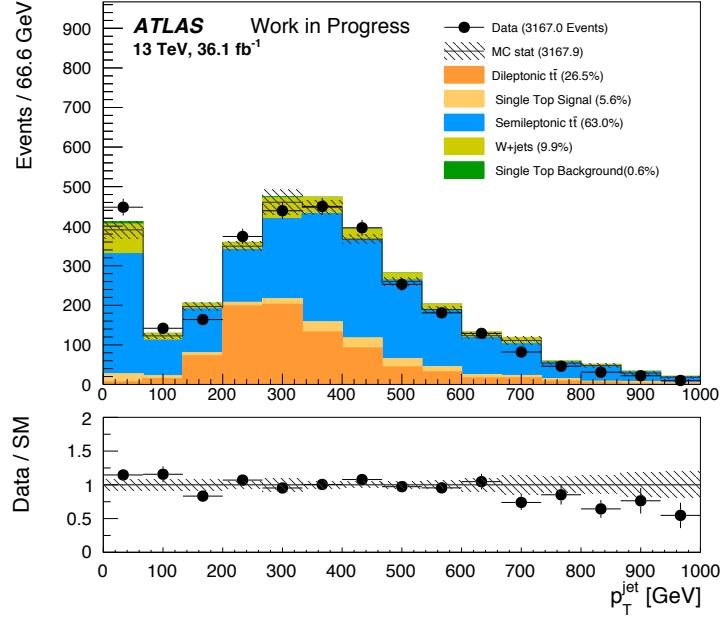
**Fig. 6.** The distribution of $p_T^{\text{jet}}$ after the preselection requirements. The ratio of data to background prediction is also shown below the figure. The signal includes dileptonic $t\bar{t}$ (orange) and single top $Wt$ production (yellow), and the background includes semileptonic $t\bar{t}$ (blue), $W$+jets (teal), and single top $s$-channel and $t$-channel productions (green).

- The fraction of the transverse momentum of the probe electron over that of the overlapping jet, denoted $p_T^{\text{fraction}}$ and is shown in Figure 7. We expect real electrons from the $W$'s produced from the top quarks to have higher $p_T$ than background electrons relative to their overlapping jets. In the figure, the low $p_T$ region can be seen to be dominated by semileptonic events.

115
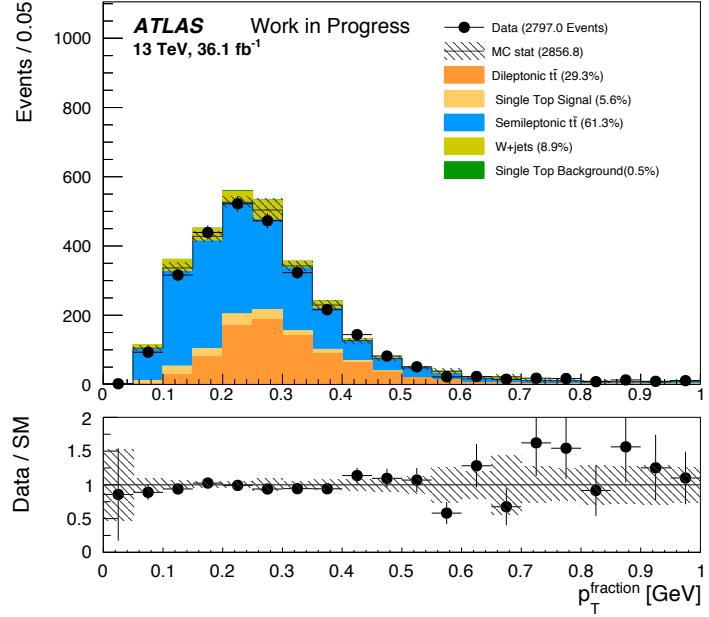
**Fig. 7.** The distribution of $p_T^{\text{fraction}}$ after the preselection requirements. The ratio of data to background prediction is also shown below the figure. The signal includes dileptonic $t\bar{t}$ (orange) and single top $Wt$ production (yellow), and the background includes semileptonic $t\bar{t}$ (blue), $W$+jets (teal), and single top $s$-channel and $t$-channel productions (green).

Further cuts to arrive at the signal region. Of all the discriminating variables shown above, $m_{\text{rjet}}^{\text{el}}$ seems to be the most discriminating variable. In addition, its distribution shows two distinct regions, one abundant in signal electrons and one largely dominated by background electrons. As will be discussed later in the chapter, the region $< 60$ GeV will define the signal region where the identification efficiencies are measured, and the region $\geq 60$ GeV will define the control region for background estimation. With this in mind, we decided to apply cuts on the other discriminating variables to further remove the undesired background, while leaving $m_{\text{rjet}}^{\text{el}}$ untouched.

The cuts are as follows:

- Missing transverse momentum $E_T^{\text{miss}} > 25$ GeV, to ensure that the QCD multi-jet background is negligible.
- The number of jets $< 5$ and sum of $p_T$ of jets $< 700$ GeV, to remove semileptonic events (Figure 4 and 5).
- $p_T$ of jet overlapping with the probe electron is between 150 GeV and 500 GeV, to remove semileptonic events (Figure 6) and at the same time make sure that boosted $t\bar{t}$ dilepton events are selected.
- $p_T(\text{probe})/p_T(\text{closest jet}) > 0.16$ (Figure 7).

The resulting distribution $m_{\text{rjet}}^{\text{el}}$ is shown in Figure 8. There are 1102 events, of which 734 are in the signal region $< 60$ GeV and 368 in the background-dominated region $\geq 60$ GeV. In the signal region, simulation shows an expected 485 dilepton events and 30 single top $Wt$ production events, whereas for the background semileptonic events, $W$+jets, and single top $s$-channel and $t$-channel are predicted to be 230, 4, and 92 respectively.
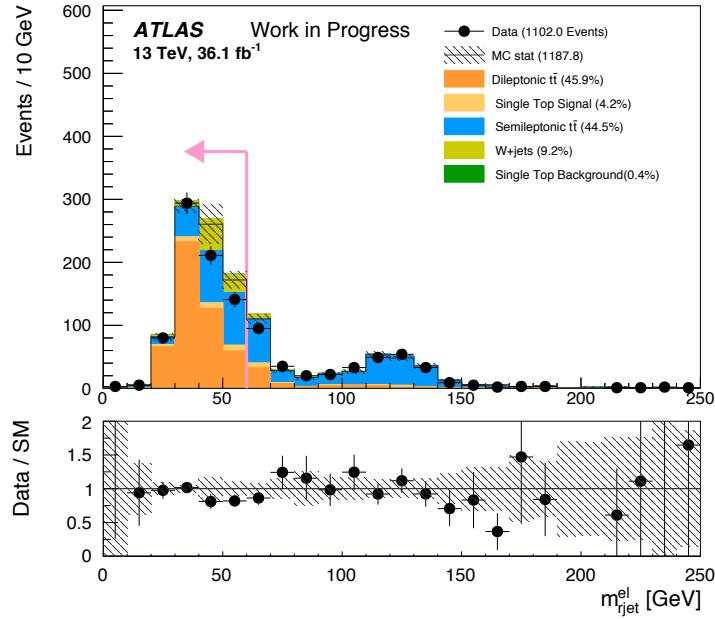


**Fig. 8.** The distribution of $m_{\text{rjet}}^{\text{el}}$ after further selections. The ratio of data to background prediction is also shown below the figure. The signal includes dileptonic $t\bar{t}$ (orange) and single top $Wt$ production (yellow), and the background includes semileptonic $t\bar{t}$ (blue), $W$+jets (teal), and single top $s$-channel and $t$-channel productions (green).

## 7.2.4. Background Estimation

The identification efficiency for electrons inside jets depends on the particular operating point (Loose, Medium, or Tight) at which the measurement is carried out. Such an efficiency, which will be denoted $\epsilon$, is the ratio of a numerator and a denominator (Section 7.2), both of which are expected to be contaminated with background electrons that need to be estimated. If $P$ denotes the number of electron candidates passing a particular ID operating point, $B_P$ the number of background electrons passing the operating point, $N$ the total number of reconstructed electron candidates in the sample, and $B_N$ the number of background electrons present in the sample, the efficiency $\epsilon$ may be written as

$$\epsilon = \frac{P - B_P}{N - B_N}. \tag{7.2.1}$$

Because ATLAS analyses using in-jet electrons all use the Medium or Tight operating points, these are the only two points which will be measured in this chapter. Accordingly, a Medium or Tight ID selection will be applied on the denominator sample, giving in each case the required numerator. Background estimations will consist of estimating the term $B_P$ separately for the Medium and Tight points in the numerator, and estimating the common term $B_N$ in the denominator.

Estimating $B_P$. Since we expect background electrons to rarely pass the Medium or Tight ID selection, we expect in turn the term $B_P$ to be very small in either case. Thus $B_P$ is taken directly from simulation, and the measurements are not expected to be affected significantly.

Figure 9 shows the $m_{\mathrm{rjet}}^{\mathrm{el}}$ distributions for electrons that pass the Medium and Tight selections. The distributions are obtained by applying a Medium or Tight ID selection in addition to the selections that define the signal region (Section 7.2.3). The number of background electrons predicted by the simulation can be seen to be indeed small in each case, accounting for only 0.3% of the total number in the Medium case and 0.1% in the Tight case.
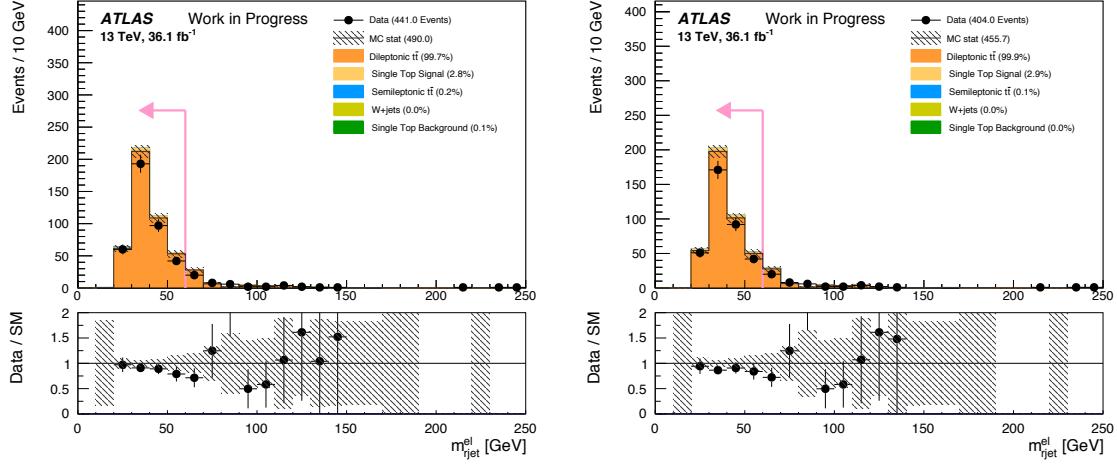


**Fig. 9.** The distribution of $m_{\mathrm{rjet}}^{\mathrm{el}}$ for electrons passing the Medium (left) and Tight (right) operating points. Background electrons figure 0.3% and 0.1% respectively.

Estimating $B_N$. The term $B_N$ represents background contamination from fake electrons found in $N$ (Formula 7.2.1). Since $N$ contains only reconstructed in-jet electrons with no ID applied, estimating $B_N$ is expected to be the most challenging part of the measurements.

The method employed for estimating $B_N$ in the following makes use the set of electrons that fail the Loose ID selection, which will be called antiloose electrons hereafter. This sample is expected to be very pure in fake electrons. These electrons are made up of two

parts, one in the signal region ($\leq 60$ GeV) and one in the background-dominated region ($\geq 60$ GeV, Figure 8). The part in the background-dominated region will be used to obtain a normalization factor, which will then be applied to the part in the signal region to estimate the number of background electrons. In what follows, the shape of the distribution of the set of antiloose electrons will also be referred to as the fake electron template. Its part in the signal region will be denoted by $T$, and that in the background-dominated region will be denoted by $T_>$.

In order to check if the set of antiloose electrons would be a suitable distribution, we use simulation and plot it against the set of background electrons in $N$, namely $B_N$. Both sets are normalized to unity in Figure 10, and $B_N$ is obtained using truth information. The figure shows that the antiloose electron sample is representative of the electron background we aim to estimate. On the other hand, Figure 11 shows the composition of antiloose electrons in the $m_{\mathrm{rjet}}^{\mathrm{el}}$ distribution. Simulation predicts about 10% of signal electron contamination, but otherwise the distribution is made up mostly of fake electrons, dominated by semileptonic $t\bar{t}$.
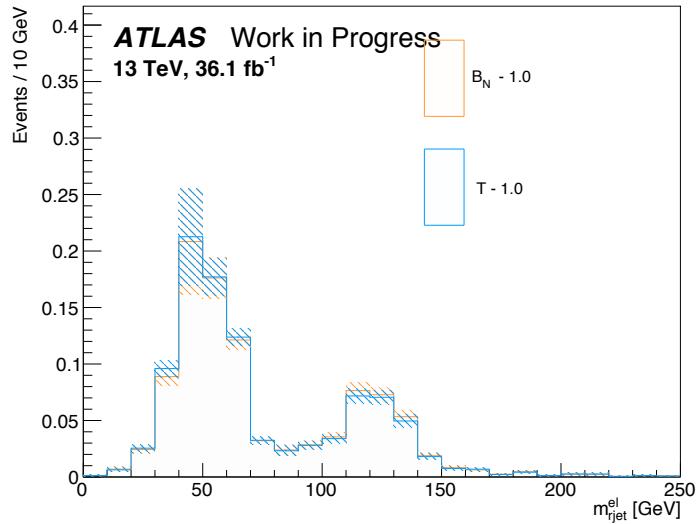


**Fig. 10.** The simulated distribution $m_{\mathrm{rjet}}^{\mathrm{el}}$ of $B_N$ against that of $T$, normalized to unity. $T$ describes very well $B_N$ and therefore it is reasonable to estimate $B_N$ using $T$.
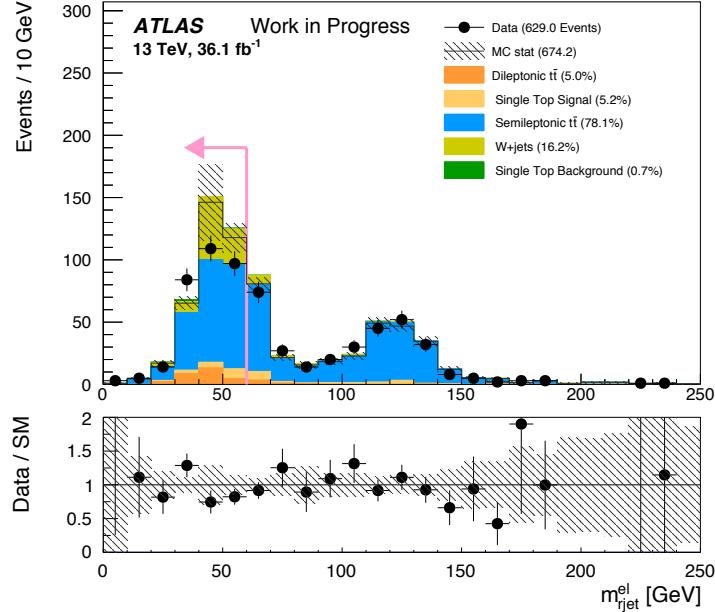
**Fig. 11.** The distribution $m_{\mathrm{rjet}}^{\mathrm{el}}$ for electrons that fail the Loose ID point, also called antiloose electrons.

Background estimation using antiloose electrons proceeds in detail as follows:

(1) First, $T$ and $T_>$ are obtained by selecting antiloose electrons. Thus the method is data-driven, $T$ and $T_>$ from simulations are not used.

(2) In addition to $N$, the set of reconstructed electron candidates in the signal region, there is also the set of reconstructed electron candidates in the background-dominated region, which will be denoted $N_>$.

Signal contamination is substracted from $T_>$, the resulting set of which is denoted $\overline{T}_>$, and signal contamination is subtracted from $N_>$, where the resulting set is denoted by $\overline{N}_>$. Then $\overline{T}_>$ is normalized to $\overline{N}_>$, to obtain a normalization factor that will then be applied to the signal region.

(3) Signal contamination is subtracted from $T$, the resulting set of which is denoted $\overline{T}$, and the normalization factor is applied to $\overline{T}$, to obtain the number of background electrons in the signal region.

In other words, the background to be estimated in the signal region, $B_N$, is measured according to

$$B_N = \overline{T} \times \frac{\overline{N}_>}{T_>}. \tag{7.2.2}$$

The following section discusses signal contamination subtractions in $T$, $T_>$, and $N_>$, and the measurements of the identification efficiencies.

### 7.2.5. The Measurements of the Identification Efficiency

The identification efficiency $\epsilon$ shown in Formula 7.2.1, where $B_P$ is taken from simulation and $B_N$ is evaluated according to Formula 7.2.2, is

$$\epsilon = \frac{P - B_P}{N - \overline{T} \times \frac{\overline{N}_>}{\overline{T}_>}}. \tag{7.2.3}$$

$\overline{T}$ is the set of antiloose electrons in the signal region $m^{\mathrm{el}}_{\mathrm{rjet}} < 60$ GeV, $T$, minus signal contamination, and $\overline{T}_>$ is the corresponding quantity in the background-dominated region $m^{\mathrm{el}}_{\mathrm{rjet}} \geq 60$ GeV. As there is an expected only 10% of signal contamination in the set of antiloose electrons (Figure 10), $\overline{T}$ and $\overline{T}_>$ will be obtained by subtracting signal contamination as predicted by simulations from $T$ and $T_>$ respectively.

On the other hand, signal contamination in $N_>$ (Figure 8), from which $\overline{N}_>$ is obtained, is larger. In fact, as has been mentioned at the end of Section 7.2.3, there are 368 events in the background-dominated region, of which simulation predicts signal contamination, made up of dilepton events and single top $Wt$ production events, to be $61 + 20 = 81$ events. In order to reduce the contribution from the estimation of this signal contamination to the uncertainty in the efficiency we will use a data-driven approach. According to Figure 9, the number of background electrons after a Medium or Tight ID selection is expected to be negligible. We expect as a result $P$, and the corresponding quantity $P_>$ in the background-dominated region, to be relatively free of background electrons. Thus $P_>$ could be used to represent signal contamination in $N_>$, provided the corresponding identification efficiency is properly taken into account. In other words,

$$\overline{N}_> = N_> - P_>/\epsilon,$$

where the efficiency in 7.2.3, which is being measured, is used again. The efficiency will be evaluated iteratively, until the change from one iteration to the next is less than 0.5%. The value of 0.5% will be taken as the uncertainty due to signal contamination subtraction in $N_>$.

The efficiencies, as well as the total statistical and systematic uncertainties (Section 7.2.6), are $\mathbf{0.870 \pm 0.017 \pm 0.031}$ for Medium and $\mathbf{0.784 \pm 0.019 \pm 0.020}$ for Tight. The efficiency is higher for Medium than for Tight, consistent with expectation. The statistical uncertainties are slightly larger for Tight, also consistent with expectation, as the statistics for Tight is slightly less than that for Medium. The relevant quantities in Formula 7.2.3 that are used to compute the efficiencies in data are listed in Table 2.

|  | MEDIUM | TIGHT |
|---|---|---|
| $P$ | 392 | 356 |
| $B_P$ | 1.47 | 0.40 |
| $N$ | 734 | 734 |
| $\overline{N_>}$ | 368 | 368 |
| $P_>$ | 49 | 48 |
| $\overline{T}$ | 267.35 ||
| $\overline{T_>}$ | 292.52 ||

**Table 2.** The relevant quantities for computing the efficiencies according to Formula 7.2.3.

The efficiencies and statistical uncertainties in simulation for the Medium and Tight operating points are also computed and are **0.871 ± 0.010** and **0.807 ± 0.011** respectively. Thus the Medium operating point in data and in simulation agree, and so do the Tight operating point in data and in simulation, within the uncertainty.

The next section discusses in detail the treatment of statistical and systematic uncertainties.

## 7.2.6. Uncertainties

The measurement of the identification efficiency is accompanied by statistical and systematic uncertainties. The identification efficiencies, the statistical uncertainties, and the systematic uncertainties have been quoted in Section 7.2.5, they are **0.870 ± 0.017 ± 0.031** and **0.784 ± 0.019 ± 0.020** for the Medium and the Tight operating points respectively. Thus the statistical uncertainty is approximately 2% for the Medium point and 2.4% for the Tight point, and the systematic uncertainty is higher, approximately 3.6% and 2.6% respectively. This section discusses in detail the treatment of the statistical and systematic uncertainties, which are listed in Table 3 at the end of this section.

Statistical Uncertainties. According to Formula 7.2.3, the efficiency is measured according to the formula

$$\epsilon = \frac{P - B_P}{N - \overline{T} \times \frac{\overline{N_>}}{\overline{T_>}}},$$

where

- $P$ is the number of electrons that pass Medium or Tight.
- $B_P$ is background contamination due to fake electrons in $P$.
- $N$ is the set of reconstructed electron candidates, and $\overline{N_>}$ the corresponding quantity in the background-dominated region minus signal contamination.

- $\overline{T}$ is the set of antiloose electrons minus signal contamination, and $\overline{T}_>$ the corresponding quantity in the background-dominated region.

Since $N$ contains $P$, and $\overline{N}_>$ contains $\overline{T}_>$, the quantities in the formula are not all independent. We may remove the correlation between $N$ and $P$ by writing $N = P + F$, where $F$ is the set of electrons that fail a particular ID point. Then

$$\epsilon = \frac{P - B_P}{P + F - \overline{T} \times \frac{\overline{N}_>}{\overline{T}_>}}.$$

The correlation between $\overline{N}_>$ and $\overline{T}_>$ remains, and moreover $F$ and $\overline{T}$ are also correlated, because in the Medium case or in the Tight case, $F$ represents electrons failing Medium or Tight respectively, and since $\overline{T}$ represents electrons failing Loose (minus signal contamination), in each case $\overline{T}$ is a subset of $F$ and there is accordingly a correlation.

In order to remove all the correlations and write the efficiency completely in terms of statistically independent quantities, we will first multiply both the numerator and the denominator by $\overline{T}_>$, to write

$$\epsilon = \frac{(P - B_P)\overline{T}_>}{P\overline{T}_> + F\overline{T}_> - \overline{T} \times \overline{N}_>}.$$

Then we will add and subtract $\overline{T} \times \overline{T}_>$ in the denominator, to have

$$\epsilon = \frac{(P - B_P)\overline{T}_>}{P\overline{T}_> + F\overline{T}_> - \overline{T} \times \overline{T}_> + \overline{T} \times \overline{T}_> - \overline{T} \times \overline{N}_>}$$

$$= \frac{(P - B_P)\overline{T}_>}{P\overline{T}_> + (F - \overline{T})\overline{T}_> - (\overline{N}_> - \overline{T}_>)\overline{T}}.$$

The difference $F - \overline{T}$ represents the set of electrons that fail Medium or Tight but pass the Loose identification, and the difference $\overline{N}_> - \overline{T}_>$ represents the set of electrons that pass the Loose identification. If we treat each of the differences as a single term, and set $S = F - \overline{T}$ and $\overline{R}_> = \overline{N}_> - \overline{T}_>$ respectively, the efficiency becomes

$$\epsilon = \frac{(P - B_P)\overline{T}_>}{P\overline{T}_> + S\overline{T}_> - \overline{R}_> \times \overline{T}}, \tag{7.2.4}$$

which is now a function of six independent quantities, $\epsilon = \epsilon(P, B_P, \overline{T}_>, S, \overline{R}_>, T)$. The statistical uncertainty of the efficiency then follows the standard error propagation formula,

$$\Delta\epsilon^2 = \left(\frac{\partial\epsilon}{\partial P}\right)^2 \Delta P^2 + \cdots + \left(\frac{\partial\epsilon}{\partial T}\right)^2 \Delta T^2. \tag{7.2.5}$$

Let $A$ denote the numerator in Formula 7.2.4 and $B$ the denominator. The terms in the formula above are then

$$\frac{\partial\epsilon}{\partial P} = \frac{B\overline{T}_> - A\overline{T}_>}{B^2}, \quad \frac{\partial\epsilon}{\partial B_P} = \frac{-B\overline{T}_>}{B^2}, \quad \frac{\partial\epsilon}{\partial \overline{T}_>} = \frac{B(P - B_P) - A(P + S)}{B^2},$$

$$\frac{\partial \epsilon}{\partial S} = \frac{-A\overline{T}_>}{B^2}, \quad \frac{\partial \epsilon}{\partial \overline{R}_>} = \frac{AT}{B^2}, \quad \frac{\partial \epsilon}{\partial \overline{\overline{T}}} = \frac{A\overline{R}_>}{B^2}.$$

Since $P$ and $S$ are the only terms in the signal region not used for background estimation, the statistical uncertainty of the efficiency is taken from the contributions of these two terms. For both operating points, the contribution from $S$ is the major one; the contribution from $P$ is small ($< 0.5\%$ from the total 2% for the Medium point and 2.4% for the Tight point).

The contributions to the uncertainty from other terms, which are used for background estimation, are taken as contributions to the total systematic uncertainty.

Systematic Uncertainties. Contributions from different sources to the total systematic uncertainty (3.6% for the Medium point and 2.5% for the Tight point), which are discussed below, are added in quadrature.

- The variation of the signal region. In addition to defining the signal region at $\leq 60$ GeV, we may define it at $\leq 50$ or $\leq 80$ GeV, the asymmetry because of the fact that signal distributions on both sides of the point 60 GeV are not equal in equal intervals. The contribution to the total systematic uncertainty is **0.022** (approximately 2.5%) for the Medium point and **0.010** (approximately 1.3%) for the Tight point.
- The variation of the term $B_P$, which is taken from simulation and represents background contamination in $P$. A 50% variation is used for a conservative estimate of the contribution of this term, which has been seen to be negligible for both Medium and Tight points ($< 0.2\%$ in both cases).
- The simultaneous variations, either up or down, of the signal contaminations in $T$ and $T_>$, the subtractions of which from both terms give $\overline{T}$ and $\overline{T}_>$. A 25% variation is used for a conservative estimate of these contributions, which are **0.017** (approximately 2%) for the Medium point and **0.015** (approximately 1.9%) for the Tight point.
- The change of the template $T$, from the distribution of antiloose electrons to the distribution of antiloose electrons in events with exactly two $b$-jets. The contributions to the total systematic uncertainty are **0.008** (approximately 0.9%) for the Medium point and **0.007** (approximately 0.9%) for the Tight point.
- The statistical uncertainties from the counting of $\overline{T}_>$, $\overline{R}_>$, and $\overline{T}$ in Formula 7.2.4. They are 0.002 (approximately 0.2%), 0.008 (approximately 0.9%), and 0.002 (approximately 0.2%) respectively for the Medium point and 0.001 (approximately 0.1%), 0.006 (approximately 0.8%), and 0.001 (approximately 0.1%) respectively for the Tight point.

| Operating Point | MEDIUM | TIGHT |
|---|:---:|:---:|
| **Systematic Uncertainties** | | |
| Variations of the signal region to 50 and 80 GeV | 0.022 | 0.010 |
| Variations of $B_P$, the (simulation) background contamination in $P$ | 0.002 | 0.000 |
| Simultaneous variations of signal contaminations in $T$ and $T_>$ | 0.017 | 0.015 |
| Change of template $T$ | 0.008 | 0.007 |
| Statistical uncertainties in the signal and control regions | 0.008 | 0.006 |
| **Statistical Uncertainties** | | |
| Contributions from $S$ and $P$ | 0.010 | 0.011 |

**Table 3.** The statistical and systematic uncertainties on the efficiency of electron identification for the Medium and Tight operating points. The statistical uncertainties from the counting of $\overline{T}_>$, $\overline{R}_>$, and $\overline{T}$ are listed as statistical uncertainties in the signal and control regions, and are combined in quadrature into a single term.

## 7.2.7. Efficiencies as Functions of the Properties of the Electron and of the Overlapping Jet

In addition to the integrated efficiencies, the efficiencies as functions of the properties of the electron and of the overlapping jet are also measured. The measurements include the following variables (Figure 12 and 13).

- $p_T$ of the probe electron, in five bins: 30-60 GeV, 60-80 GeV, 80-110 GeV, 110-140 GeV, and $> 140$ GeV.
- $|\eta|$ of the probe electron, in five bins: 0.0-0.3, 0.3-0.6, 0.6-0.9, 0.9-1.3, and $> 1.3$.
- $\Delta R$ between the probe electron and the overlapping jet, in five bins: 0.0-0.15, 0.15-0.19, 0.19-0.23, 0.23-0.27, and 0.27-0.4.
- $p_T$ of the overlapping jet, in five bins: 150-220 GeV, 220-280 GeV, 280-340 GeV, 340-400 GeV, and 400-500 GeV.
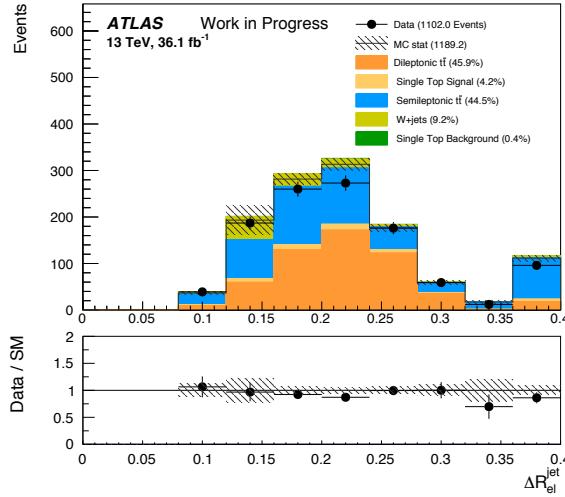
**(a)** $\Delta R$ between the probe electron and the overlapping jet
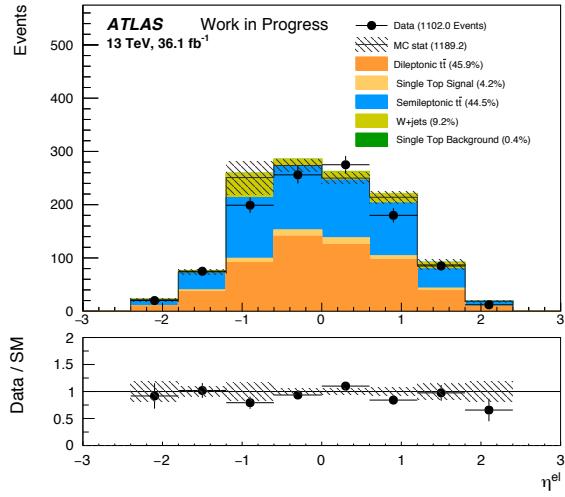


**(b)** $\eta$ of the probe electron.

**Fig. 12.** The distributions of $\Delta R$ between the probe electron and the overlapping jet and $\eta$ of the probe electron.

The efficiencies, for the Medium and Tight operating points, as a function of the $p_T$ and $|\eta|$ of the probes, are shown in Figure 14. Also shown are the efficiencies for standard $Z \to e^+e^-$ electrons obtained by the ATLAS collaboration [**43, 102**], which, as can be seen, agree with those for in-jet electrons within the error bars. As a function of the $p_T$ of the probe, the efficiencies increase as $p_T$ increases. On the other hand, no obvious dependency is seen in the case of $|\eta|$.
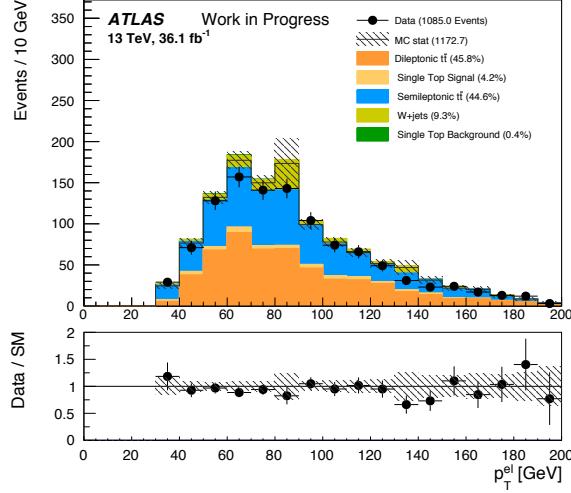
**(a)** $p_T$ of the probe
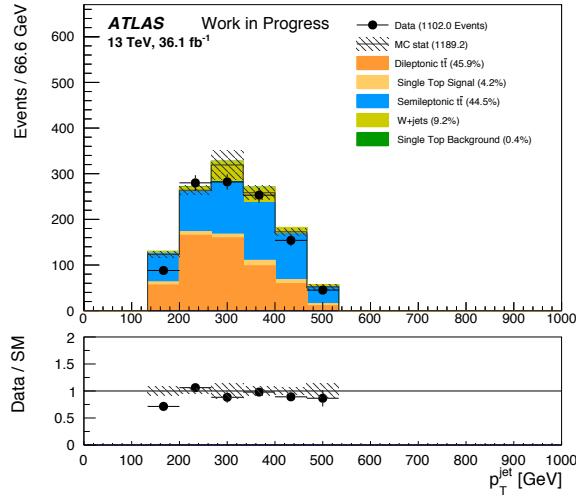


**(b)** $p_T$ of the overlapping jet

**Fig. 13.** The distributions of $p_T$ of the probe and $p_T$ of the overlapping jet.

The efficiencies as a function of the $\Delta R$ between the probe and the overlapping jet, and as a function of the $p_T$ shown in Figure 15. The rates appear to stay constant within the uncertainties.
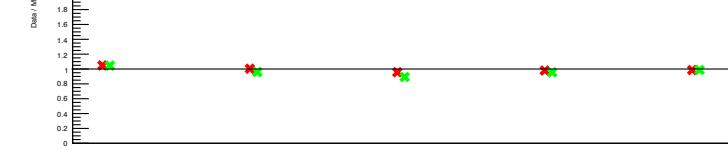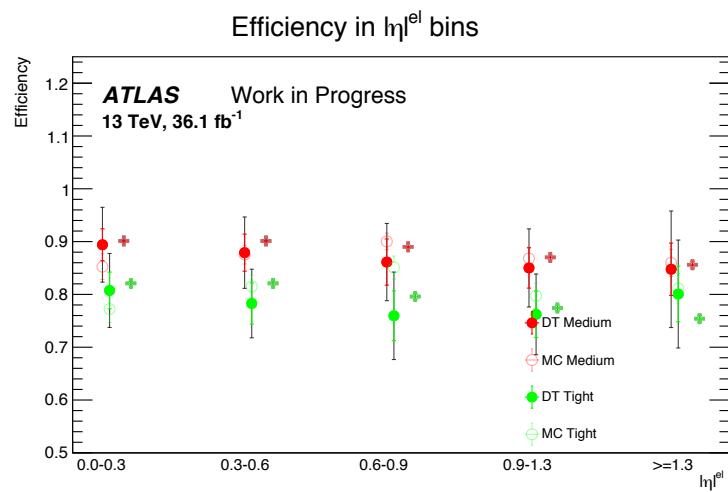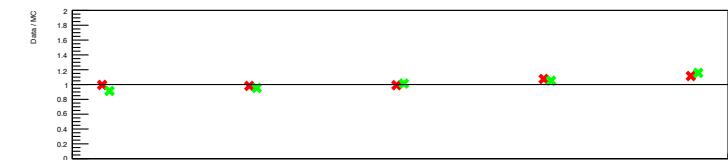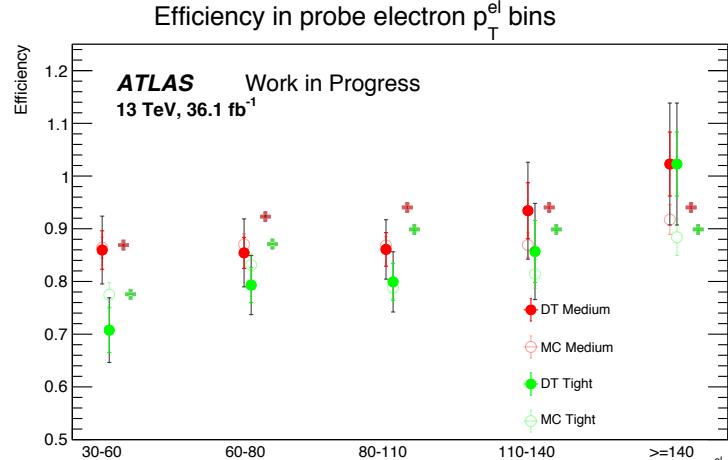
**Fig. 14.** The efficiencies in $p_T$ of the probe electron as well as in $|\eta|$ of the probe. Also shown are the efficiencies for standard electrons and the associated uncertainties (which are very small and therefore are barely visible).
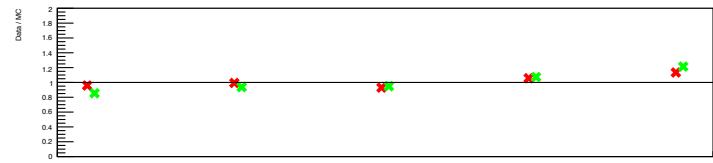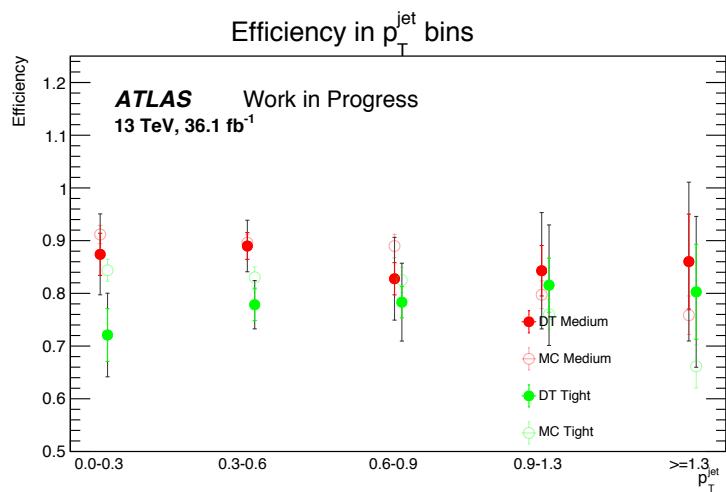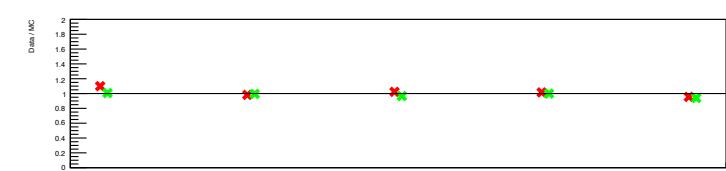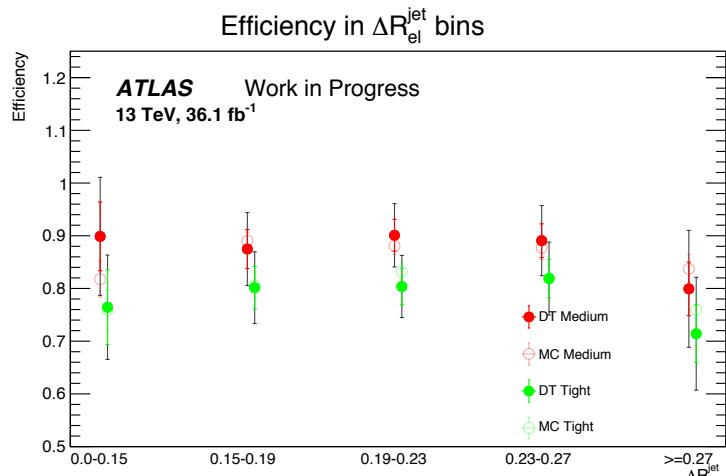
**Fig. 15.** The efficiencies in $\Delta R$ between the probe electron and the overlapping jet, as well as in $p_T$ of the overlapping jet.

## 7.3. Conclusions

This chapter describes the work to measure the identification efficiencies for in-jet electrons. It was the first attempt to perform such a measurement since Run 2 began, and the first ever using dilepton $t\bar{t}$ events. The measurement use the data collected in the period 2015-2016, at 13 TeV centre-of-mass and totaled 36.1 fb$^{-1}$ in integrated luminosity. A sample of electrons for the measurements is obtained by selecting boosted $t\bar{t}$ dilepton ($e\mu$) events. Background estimations use both simulations and data, and the efficiencies are evaluated iteratively. The efficiencies are measured for the Medium and Tight operating points, on both data and simulation. The efficiencies as functions of the properties of the electrons and of the overlapping jets are also measured, showing that the identification efficiencies for standard isolated electrons provided by the Egamma group appear to apply also for in-jet electrons. In all of the results, the efficiencies predicted by simulation agree with those obtained from the measurements on data.

# Chapter 8

# CONCLUSIONS

This thesis presented my work done as part of the ATLAS collaboration. The common theme is electrons, specifically the improvement of the reconstruction and identification of signal electrons in SUSY searches. The main work was discussed in three chapters:

- Chapter 5 describes the estimation of the charge mis-identification rates for electrons by a likelihood function, the Poisson likelihood in particular. These rates are important for new physics searches in which the final state consists of a pair of same-sign leptons, where the leptons refer to electrons and muons. The method uses $Z \rightarrow e^+e^-$ events, which furnish a source of clean and high-statistics set of electrons on which charge measurements could be performed. A Poisson likelihood function is constructed, taking into account the dependency of charge mis-identification rates on kinematic properties such as on $p_T$ and on $\eta$ of the electrons. The results show that in most bins, simulation over-estimates the rates as compared to the data by 5-20%. The method has been applied to correct the simulation prediction for the electron charge mis-identification rates by the ATLAS collaboration.

- Chapter 6 describes a SUSY search for gluino pair-production, which is highly motivated as gluinos are expected by naturalness to have a mass around the TeV scale, and moreover their production cross section is high at the LHC. The data are collected in the 2015-2016 data taking period, at center-of-mass $\sqrt{s} = 13$ TeV and corresponds to an integrated luminosity of 36.1 fb$^{-1}$. The final state consists of large missing transverse momentum and multiple jets, among which at least three must be $b$-jets. The chapter focuses on the leptonic final state, which requires in addition at least one lepton (either an electron or a muon). Following the approach used in the $t\bar{t}$ resonance search, a boosted overlap removal procedure between jets and muons is introduced into the analysis, which is adopted for jets and electrons in a subsequent version of the analysis. An optimization for the selection of the discriminating variables for the leptonic channel is also described. No excess relative to the Standard

Model background is claimed. Model-independent limits are set on the visible cross-section for new physics processes, and model-dependent limits are set for gluino and neutralino masses. Gluino masses of less than 1.97 TeV for neutralino masses below approximately 300 GeV are excluded at the 95% CL, showing an improvement over the same analysis using the 2015 dataset alone.

- Chapter 7 describes the measurements of the identification efficiencies for electrons found within $\Delta R = 0.4$ of high-$p_T$ jets. The measurements are motivated by a considerable increase in signal acceptance seen in some SUSY searches (the SUSY search described in Chapter 6 is a particular example) when electrons overlapping with jets are selected, as well as by the fact that prior to the measurements only electrons non-overlapping with jets had been calibrated. The data used corresponds to an integrated luminosity of 36.1 fb$^{-1}$, collected at center-of-mass $\sqrt{s} = 13$ TeV. The measurements use a dilepton $(e\mu)$ $t\bar{t}$ sample enriched in boosted top quarks. The results present the integrated efficiencies and the efficiencies as a function of the $p_T$ of the electrons, $|\eta|$ of the electrons, $\Delta R$ between the electrons and the closest jets, and of the $p_T$ of the overlapping jets.

As the search for SUSY continues, the treatment of electrons will continue to be refined and improved. The reconstruction, identification, and selection of electrons are already benefiting from machine learning methods, and this trend is expected to accelerate with time. On the other hand, even though no sign of SUSY has been found, we are hopeful that as more data are collected, as well as from an increase in luminosity and centre-of-mass energy (the LHC will resume its operation in 2021 at $\sqrt{s} = 14$ TeV and 2.5 times the nominal luminosity) and better analysis techniques, the search sensitivity will improve, giving us deeper insight into supersymmetry (and if we are lucky, a discovery).

# References

[1] S. Laporta and E. Remiddi, *The analytical value of the electron $(g - 2)$ at order $\alpha^3$ in QED*, Physics Letters B **379** (1996) 283 - 291.

[2] R. Barbieri and G. F. Giudice, *Upper Bounds on Supersymmetric Particle Masses*, Nucl. Phys. B **306** (1988) 63-76.

[3] S. L. Glashow, *Partial Symmetries of Weak Interactions*, Nucl. Phys. **22** (1961) 579-588.

[4] S. Weinberg, *A Model of Leptons*, Phys. Rev. Lett. **19** (1967) 1264-1266.

[5] A. Salam, *Elementary Particle Physics: Relativistic Groups and Analyticity*, Almquvist and Wiksell (1968) 367.

[6] M. Srednicki, *Quantum field theory*, Cambridge University Press 2007.

[7] P. W. Higgs, *Broken symmetries, massless particles and gauge fields*, Phys. Lett. **12** (1964) 132-133.

[8] F. Englert and R. Brout, *Broken Symmetry and the Mass of Gauge Vector Mesons*, Phys. Rev. Lett. **13** (1964) 321-323.

[9] G. S. Guralnik, C. R. Hagen, and T. W. B.Kibble, *Global Conservation Laws and Massless Particles*, Phys. Rev. Lett. **13** (1964) 585-587.

[10] ATLAS Collaboration, *Observation of a new particle in the search for the Standard Model Higgs boson with the ATLAS detector at the LHC*, Phys. Lett. B **716** (2012) 1-29.

[11] CMS Collaboration *Observation of a New Boson at a Mass of 125 GeV with the CMS Experiment at the LHC*, Phys. Lett. B **716** (2012) 30-61.

[12] Robert J. A. Lambourne, *Relativity, Gravitation and Cosmology*, Cambridge University Press June 2010.

[13] G. Burdman, *New solutions to the hierarchy problem*, Brazilian Journal of Physics **37** (2007) 506 - 513.

[14] G. 't Hooft, C. Itzykson, A. Jaffe, H. Lehmann, P. K. Mitter, I. M. Singer, and R. Stora, *Recent Developments in Gauge Theories. Proceedings, Nato Advanced Study Institute, Cargese, France, August 26 - September 8, 1979*, NATO Sci. Ser. B **59** (1980) pp.1-438.

[15] K. G. Begeman, A. H. Broeils, and R. H. Sanders, *Extended rotation curves of spiral galaxies: Dark haloes and modified dynamics*, Mon. Not. Roy. Astron. Soc. **249** (1991) 523.

[16] J. Dunkley et al., *Five-Year Wilkinson Microwave Anisotropy Probe (WMAP) Observations: Bayesian Estimation of CMB Polarization Maps*, Astrophys. J. **701** (2009) 1804.

[17] G. Bertone, D. Hooper, and J. Silk, *Particle dark matter: Evidence, candidates and constraints*, Phys. Rept. **405** (2005) 279-390.

[18] J. L. Feng, *Dark Matter Candidates from Particle Physics and Methods of Detection*, Ann. Rev. Astron. Astrophys. **48** (2010) 495-545.

[19] J. Frieman, M. Turner, and D. Huterer, *Dark Energy and the Accelerating Universe*, Ann. Rev. Astron. Astrophys. **46** (2008) 385-432.

[20] A. Van, et al. *Distribution of dark matter in the spiral galaxy NGC 3198*, Astrophys. J. **295** (1985).

[21] Y. A. Golfand and E. P. Likhtman, *Extension of the Algebra of Poincare Group Generators and Violation of p Invariance*, JETP Lett. **13** (1971) 323-326.

[22] D. V. Volkov and V. P. Akulov, *Is the Neutrino a Goldstone Particle?*, Phys. Lett. B **46** (1973) 109-110.

[23] J. Wess and B. Zumino, *Supergauge Transformations in Four-Dimensions*, Nucl. Phys. B **70** (1974) 39-50.

[24] J. Wess and B. Zumino, *Supergauge Invariant Extension of Quantum Electrodynamics*, Nucl. Phys. B **78** (1974) 1.

[25] S. Ferrara and B. Zumino, *Supergauge Invariant Yang-Mills Theories*, Nucl. Phys. B **79** (1974) 413.

[26] A. Salam and J. A. Strathdee, *Supersymmetry and Nonabelian Gauges*, Phys. Lett. B **51** (1974) 353-355.

[27] J. R. Ellis et al., *Supersymmetric Relics from the Big Bang*, Nucl. Phys. B **238** (1984) 453-476.

[28] S. Dimopoulos and H. Georgi, *Softly Broken Supersymmetry and SU(5)*, Nucl. Phys. B **193** (1981) 150-162.

[29] N. Sakai, *Naturalness in Supersymmetric Guts*, Z. Phys. C **11** (1981) 153.

[30] S. Dimopoulos, S. Raby, and F. Wilczek, *Supersymmetry and the Scale of Unification*, Phys. Rev. D **24** (1981) 1681-1683.

[31] L. E. Ibanez and G. G. Ross, *Low-Energy Predictions in Supersymmetric Grand Unified Theories*, Phys. Lett. B **105** (1981) 439-442.

[32] S. P. Martin, *A Supersymmetry primer*, (1997) 1-98. `https://arxiv.org/abs/hep-ph/9709356`.

[33] MSSM Working Group Collaboration, *The Minimal Supersymmetric Standard Model: Group Summary Report. The Minimal supersymmetric standard model: Group summary report*, hep-ph/9901246, 1998. `http://cds.cern.ch/record/376049`.

[34] P. Pralavorio, *Particle Physics and Cosmology: Proceedings, 100th Les Houches Summer School*, Post-Planck Cosmology: Les Houches, France, July 8 - August 2, 2013 (2015) 353-405.

[35] M. E. Peskin, *Supersymmetry in Elementary Particle Physics*, Theoretical Advanced Study Institute in Elementary Particle Physics: Exploring New Frontiers Using Colliders and Neutrinos, SLAC-PUB-13079 **1** (2008) 609-04. `https://arxiv.org/abs/0801.1928`.

[36] CERN web site, *About CERN*, `https://home.cern/about`. Accessed: 2020-02-11.

[37] R. Voss and A. Breskin, *The CERN Large Hadron Collider, accelerator and experiments*, (2009) `https://jinst.sissa.it/LHC/`.

[38] F. Marcastel, *CERN's Accelerator Complex. La chaîne des accélérateurs du CERN*, (2013).

[39] ATLAS Collaboration, *The ATLAS Experiment at the CERN Large Hadron Collider*, JINST **3** (2008) S08003.

[40] M. Schott and M. Dunford, *Review of single vector boson production in pp collisions at $\sqrt{s} = 7$ TeV*, Eur. Phys. J. C **74** (2014) 60 p.

[41] ATLAS Collaboration, *ATLAS Insertable B-Layer Technical Design Report*, ATLAS-TDR-19, (2010). `https://cds.cern.ch/record/1291633`.

[42] S. Artz et al, *Upgrade of the ATLAS Central Trigger for LHC Run-2*, JINST **10** (2015) C02030.

[43] ATLAS Collaboration, *Electron reconstruction and identification in the ATLAS experiment using the 2015 and 2016 LHC proton-proton collision data at $\sqrt{s} = 13$ TeV*, Eur. Phys. J. C **79** (2019) 639.

[44] ATLAS Collaboration, *Electron and photon reconstruction and performance in ATLAS using a dynamical, topological cell clustering-based approach*, ATL-PHYS-PUB-2017-022, CERN, Geneva, Dec, 2017. `https://cds.cern.ch/record/2298955`.

[45] W. Lampl et al., *Calorimeter clustering algorithms: Description and performance*, ATL-LARG-PUB-2008-002, 2008. `https://cds.cern.ch/record/1099735`.

[46] ATLAS Collaboration, *Performance of the ATLAS Track Reconstruction Algorithms in Dense Environments in LHC Run 2*, Eur. Phys. J. C **77** (2017) 673.

[47] T. Cornelissen et al., *The global $\chi^2$ track fitter in ATLAS*, J. Phys. Conf. Ser. **119** (2008) 032013. http://cds.cern.ch/record/1176901.

[48] ATLAS Collaboration, *Improved electron reconstruction in ATLAS using the Gaussian Sum Filter-based model for bremsstrahlung*, ATLAS-CONF-2012-047, CERN, Geneva, May, 2012. https://cds.cern.ch/record/1449796.

[49] ATLAS Collaboration, *Electron and photon energy calibration with the ATLAS detector using LHC Run 1 data*, Eur. Phys. J. C **74** (2014) 3071.

[50] ATLAS Collaboration, *Electron and photon energy calibration with the ATLAS detector using 2015-2016 LHC proton-proton collision data*, JINST **14** (2019) P03017.

[51] A. Hocker et al., *TMVA - Toolkit for Multivariate Data Analysis with ROOT: Users guide. TMVA - Toolkit for Multivariate Data Analysis*, physics/0703039, CERN, Geneva, Mar, 2007. https://cds.cern.ch/record/1019880.

[52] The ATLAS collaboration, *Search for doubly-charged Higgs boson production in multi-lepton final states with the ATLAS detector using proton-proton collisions at $\sqrt{s} = 13$ TeV*, Eur. Phys. J. C **78** (2017).

[53] ATLAS Collaboration, *$W^{\pm}W^{\pm}jj$ in pp Collisions at $\sqrt{s} = 8$ TeV with the ATLAS Detector*, Phys. Rev. Lett. **113** (2014) 141803.

[54] ATLAS Collaboration, *Evidence for the associated production of the Higgs boson and a top quark pair with the ATLAS detector*, Phys. Rev. D **97** (2018) 072003.

[55] ATLAS Collaboration, *Search for supersymmetry at $\sqrt{s}$=8 TeV in final states with jets and two same-sign leptons or three leptons with the ATLAS detector.*, JHEP **06** (2014) 035.

[56] B. Nachman, *For a light stop, less is more when gluinos mediate*, Mod. Phys. Lett. A **31** (2016) 1650052.

[57] M. Papucci, J. T. Ruderman, A. and Weiler, *Natural SUSY Endures*, JHEP **09** (2012) 035.

[58] J. Alwall P. Schuster, and N. Toro, *Simplified Models for a First Characterization of New Physics at the LHC*, Phys. Rev. D **79** (2009) 075020.

[59] D. Alves et al., *Simplified Models for LHC New Physics Searches*, J. Phys. G **39** (2012) 105005.

[60] ATLAS Collaboration, *Search for supersymmetry in final states with missing transverse momentum and multiple b-jets in proton-proton collisions at $\sqrt{s} = 13$ TeV* , JHEP **06** (2018) 107.

[61] ATLAS Collaboration, *Luminosity determination in pp collisions at $\sqrt{s} = 8$ TeV* , Eur. Phys. J. C **76** (2016) 653.

[62] S. Agostinelli et al., *GEANT4: A Simulation toolkit*, Nucl. Instrum. Meth. A **506** (2003) 250-303.

[63] J. Alwall et al. , *The automated computation of tree-level and next-to-leading order differential cross sections, and their matching to parton shower simulations*, JHEP **07** (2014) 079.

[64] R. D. Ball et al., *Parton distributions with LHC data*, Nucl. Phys. B **867** (2013) 244-289.

[65] T. Sjostrand, S. Mrenna, and P. Z. Skands, *A Brief Introduction to PYTHIA 8.1*, Comput. Phys. Commun. **178** (2008) 852-867.

[66] S. Alioli et al., *A general framework for implementing NLO calculations in shower Monte Carlo programs: the POWHEG BOX*, JHEP **06** (2010) 043.

[67] H-L. Lai, *New parton distributions for collider physics*, Phys. Rev. D **82** (2010) 074024.

[68] M. Bahr et al., *Herwig++ Physics and Manual*, Eur. Phys. J. C **58** (2008) 639-707.

[69] T. Gleisberg et al., *Event generation with SHERPA 1.1*, JHEP **02** (2009) 007.

[70] ATLAS collaboration, *Vertex Reconstruction Performance of the ATLAS Detector at $\sqrt{s} = 13$ TeV*, ATL-PHYS-PUB-2015-026, CERN, Geneva, Jul, 2015. https://cds.cern.ch/record/2037717.

[71] ATLAS Collaboration, *Topological cell clustering in the ATLAS calorimeters and its performance in LHC Run 1*, Eur. Phys. J. C **77** (2017) 490.

[72] M. Cacciari, G. P. Salam, and G. Soyez, *The anti-$k_t$ jet clustering algorithm*, JHEP **04** (2008) 063.

[73] M. Cacciari, G. P. Salam, and G. Soyez,, *FastJet User Manual*, Eur. Phys. J. C **72** (2012) 1896.

[74] The ATLAS collaboration, *Selection of jets produced in* 13 *TeV proton-proton collisions with the ATLAS detector*, ATLAS-CONF-2015-029, 2015. `https://cds.cern.ch/record/2037702?ln=en`.

[75] *B-tagging diagram*, `https://commons.wikimedia.org/wiki/File:B-tagging_diagram.png`. Accessed: 2020-02-11.

[76] ATLAS Collaboration, *Performance of b-Jet Identification in the ATLAS Experiment*, JINST **11** (2016) P04008.

[77] ATLAS Collaboration, *Optimisation of the ATLAS b-tagging performance for the 2016 LHC Run*, ATL-PHYS-PUB-2016-012, CERN, Geneva, Jun, 2016. `https://cds.cern.ch/record/2160731`.

[78] B. Nachman et al., *Jets from Jets: Re-clustering as a tool for large radius jet reconstruction and grooming at the LHC*, JHEP **02** (2015) 075.

[79] The ATLAS collaboration, *Electron efficiency measurements with the ATLAS detector using the 2015 LHC proton-proton collision data*, ATLAS-CONF-2016-024, 2016. `https://cds.cern.ch/record/2157687`.

[80] ATLAS Collaboration, *Muon reconstruction performance of the ATLAS detector in proton-proton collision data at $\sqrt{s}$ =13 TeV*, Eur. Phys. J. C **76** (2016) 292.

[81] ATLAS Collaboration, *Performance of missing transverse momentum reconstruction for the ATLAS detector in the first proton-proton collisions at at $\sqrt{s}$ = 13 TeV*, ATL-PHYS-PUB-2015-027, CERN, Geneva, Jul, 2015. `https://cds.cern.ch/record/2037904`.

[82] ATLAS Collaboration, *Expected performance of missing transverse momentum reconstruction for the ATLAS detector at $\sqrt{s}$ = 13 TeV*, ATL-PHYS-PUB-2015-023, CERN, Geneva, Jul, 2015. `https://cds.cern.ch/record/2037700`.

[83] The ATLAS collaboration, *A search for $t\bar{t}$ resonances in the lepton plus jets final state with ATLAS using 14 $fb^{-1}$ of pp collisions at $\sqrt{s}$ = 8 TeV*, ATLAS-CONF-2013-052, 2013. `http://cds.cern.ch/record/1547568`.

[84] L. Moneta et al., *The RooStats Project*, PoS ACAT2010 (2010) 057 `https://arxiv.org/abs/1009.1003`.

[85] E. Gross, *LHC statistics for pedestrians*, PHYSTAT-LHC Workshop on Statistical Issues for LHC Physics (2007) 205–212

[86] ATLAS Collaboration, *Search for supersymmetry in final states with two same-sign or three leptons and jets using 36 $fb^{-1}$ of $\sqrt{s}$ = 13 TeV pp collision data with the ATLAS detector*, JHEP, **09** (2017) 084.

[87] ATLAS Collaboration, *Search for squarks and gluinos with the ATLAS detector in final states with jets and missing transverse momentum using 4.7 $fb^{-1}$ of $\sqrt{s}$ = 7 TeV proton-proton collision data*, Phys. Rev. D **87** (2013) 012008.

[88] ATLAS Collaboration, *Jet Calibration and Systematic Uncertainties for Jets Reconstructed in the ATLAS Detector at $\sqrt{s}$ = 13 TeV*, CERN, Geneva, Jul, 2015. `https://cds.cern.ch/record/2037613`.

[89] ATLAS Collaboration, *Measurements of fiducial cross-sections for $t\bar{t}$ production with one or two additional b-jets in pp collisions at $\sqrt{s}$ =8 TeV using the ATLAS detector*, Eur. Phys. J. C **76** (2016) 11.

[90] G. Cowan, *Asymptotic formulae for likelihood-based tests of new physics*, Eur. Phys. J. C **71** (2011) 1554.

[91] M. Baak et al., *HistFitter software framework for statistical data analysis*, Eur. Phys. J. C **75** (2015) 153.

[92] M. Czakon and A. Mitov, *Top++: A Program for the Calculation of the Top-Pair Cross-Section at Hadron Colliders*, Comput. Phys. Commun. **185** (2014) 2930.

[93] A. L. Read, *Presentation of search results: The CL(s) technique*, J. Phys. G **28** (2002) 2693-2704.

[94] ATLAS Collaboration, *Search for pair production of gluinos decaying via stop and sbottom in events with b-jets and large missing transverse momentum in pp collisions at $\sqrt{s} = 13$ TeV with the ATLAS detector*, Phys. Rev. D. **94** (2016) 032003.

[95] ATLAS Collaboration, *Search for supersymmetry in events with b-tagged jets and missing transverse momentum in pp collisions at $\sqrt{s} = 13$ TeV with the ATLAS detector*, JHEP, **11** (2017) 195.

[96] ATLAS Collaboration, *Search for heavy particles decaying into top-quark pairs using lepton-plus-jets events in proton-proton collisions at $\sqrt{s} = 13$ TeV with the ATLAS detector*, Eur. Phys. J. C **78** (2018) 565.

[97] ATLAS Collaboration, *Search for pair production of heavy vector-like quarks decaying into high-$p_T$ W bosons and top quarks in the lepton-plus-jets final state in pp collisions at $\sqrt{s} = 13$ TeV with the ATLAS detector*, JHEP **08** (2018) 048.

[98] ATLAS Collaboration, *Search for a scalar partner of the top quark in the jets plus missing transverse momentum final state at $\sqrt{s}=13$ TeV with the ATLAS detector*, JHEP **12** (2017) 085.

[99] ATLAS Collaboration, *Search for squarks and gluinos in final states with jets and missing transverse momentum using 36 fb$^{-1}$ of $\sqrt{s} = 13$ TeV pp collision data with the ATLAS detector*, Phys. Rev. D **97** (2018) 112001.

[100] ATLAS Collaboration, *Performance of jet substructure techniques for large-R jets in proton-proton collisions at $\sqrt{s} = 7$ TeV using the ATLAS detector*, JHEP **09** (2013) 076.

[101] E. Thompson, *BOOST!*, `https://www.quantumdiaries.org/2012/08/05/boost/`. Accessed: 2020-02-11.

[102] ATLAS Collaboration, *Electron efficiency measurements with the ATLAS detector using 2012 LHC proton-proton collision data*, Eur. Phys. J. C **77** (2017) 195.

[103] T. Sjostrand, S. Mrenna, and P. Z. Skands, *PYTHIA 6.4 Physics and Manual*, JHEP **05** (2006) 026.